

# Ultimate Limit State Analysis of a Segmented Tunnel Lining

- Results of full-scale tests compared to finite element analysis -



 **TU Delft**



Arjan Lutikholt  
Delft, July 4, 2007



Ultimate Limit State Analysis of a Segmented Tunnel Lining  
- Results of full-scale tests compared to finite element analysis -

Arjan Lutikholt  
Section Structural Engineering - Concrete Structures  
Faculty of Civil Engineering and Geosciences  
Delft University of Technology

Keywords:

*Segmented tunnel lining, experiments, numerical simulations,  
DIANA, full-scale test, ULS, failure load, beam model,  
plane stress model, ring interaction*

July 4, 2007



# Preface

This research was carried out as a Master Thesis at the Section of Concrete Structures at Delft University of Technology in cooperation with TNO Built Environment and Geosciences. With this assignment I got a chance to work on a very interesting and unique project. It gave me the opportunity to combine two subjects that I enjoyed most during my study, structural engineering and concrete structures.

I would like to thank the members of my examination committee for sharing their knowledge and for their help and support during the realization of this thesis. I address special thanks to Joop den Uijl who was my supervisor and gave me the chance to work on such a fantastic research project. He gave me advice and support throughout the process of writing this master thesis. I also want to thank Adri Vervuurt who gave me the opportunity to carry out this master thesis at TNO and for discussing various problems and difficulties with me. Furthermore I would like to thank all the employees from TNO for creating a pleasant atmosphere to work in, especially Henco Burggraaf and Ton van Overbeek who made me familiar with DIANA. Ane de Boer from the RWS Bouwdienst I would like to thank for given his review and recommendations on improving the FE calculations. I also appreciate the interesting discussions with the members of the CUR/COB commission TC151 of which this research is part.

Delft, July 4, 2007  
Arjan Lutikholt

Examination Committee:

Prof.dr.ir. J.C. Walraven, TU Delft - Section Structural Engineering - Concrete Structures  
Ir. J.A. den Uijl, TU Delft - Section Structural Engineering - Concrete Structures  
Dr.ir. A.H.J.M. Vervuurt, TNO Built Environment and Geosciences  
Dr.ir. C.B.M. Blom, TU Delft - Section Structural Engineering - Concrete Structures  
Ir. A. de Boer, Rijkswaterstaat Bouwdienst  
Dr.ir. P.C.J. Hoogenboom, TU Delft - Section Structural Engineering - Structural Mechanics  
Ir. L.J.M. Houben, TU Delft

Delft University of Technology  
Faculty of Civil Engineering and Geosciences  
Section Structural Engineering - Concrete Structures



# Summary

Due to the fact that the Netherlands is increasingly crowded and due to the continuing growing demand for mobility, a great interest is taken in underground construction. Because of low hindrances during construction and lack of space in populated areas, shield driven tunnels are becoming more popular whereas its application in soft soils is relatively new. In the early constructed tunnels measurements showed that stresses in the construction phase were considerably higher than expected. Because of these measurements and unexpected damage in constructed tunnels a full-scale test set-up was build at Delft University of Technology for obtaining knowledge on the lining behaviour. The initial test program aimed at providing data for the validation of FE models in the Serviceability Limit State and for investigating the effect of some specific construction steps on the lining behaviour.

The most recent tests performed aimed at providing data regarding the tunnel behaviour under ovalisation loads in the Ultimate Limit State. For determining the effectiveness of the ring joints and the interaction between neighbouring rings two tests have been performed. In the first experiment carried out a high axial force was applied contrarily to the second experiment in which a low axial force was applied. The goal of this master thesis is to gain understanding in the behaviour of the lining in the ULS load conditions. To achieve this, this thesis starts with various theoretical concepts, validated with experimental results, for describing segment joint rotations and describing shear and slip of the ring joints. Also different failure mechanisms are analysed regarding failure of the soil behind the lining as well as failure of the lining itself.

For obtaining a clear view of the lining deformations during the two experiments and for understanding its behaviour especially at failure, the deformed shape of the lining is calculated for every load step based on the measured joint rotations and the measured segment curvatures. Subsequently the deformations are split into the contributions of the joint rotations and the segment curvatures. The calculated deformations show a very good agreement with the deformations obtained with externally measured displacements in the linear branch of loading. Discrepancies in the non-linear branch give an indication for the level of concrete cracking in a certain ring.

It turned out that in the first experiment, in which a high axial force was applied, deformations in the top and bottom ring were mainly due to joint rotations and segment curvatures. The joint rotations in the middle ring were significantly lower whereas a large share of deformations were caused by concrete cracking. Because of the high frictional capacity of the ring joints, the segments in the middle ring were loaded additionally due to the bending moments transferred from the neighbouring rings. The segments in the middle ring were

therefore loaded until their bending moment capacity was reached at  $36 \text{ kN/Jack}$ . Failure was initiated by cracking of the critical concrete segments in the middle ring and followed by an ongoing rotation of segment joints in adjoining rings.

In the second experiment a weak axial interaction was present leading to a sudden increase in the ovalisation measured at  $22 \text{ kN/Jack}$ . Failure of the lining was obtained by failure of the segment joints that was observed in all three rings almost simultaneously. Before the critical segments were loaded to their bending moment capacity the shear strength of the plywood sheets was reached leading to slip of the ring joints, and subsequently, failure of the lining.

From numerical analyses of a single tunnel segment it became clear that due to a low reinforcement ratio the bending capacity of segments is affected strongly by the concrete tension softening properties. Due to mesh dependency in bending and uncertain tension softening parameters, four different sets of material properties for modelling concrete fracture are adopted, validated and later on implemented in the complete lining model.

For modelling the lining behaviour in the ULS a 1D FE model is developed. The model contains three rings each composed of 7 segments and 1 key segment. The segments are modelled with beam elements and interface elements representing the plywood sheets at the ring joints. Both components are assigned with non-linear material properties. The segment joints are modelled using a single beam element with rotational properties according to Janssen. To validate numerical calculations a more sophisticated 2D plane stress model is developed in which the joints and stresses are analysed in more detail. Comparing the deformations in the segments and the rotations in the joints show that between both models a very good agreement is found. The initiation and propagation of cracks seems to be more realistically modelled by the 2D model. Because of the low computation time and the ability to analyse the structural behaviour more easily, the 1D beam model is adopted for further simulating and studying the lining behaviour.

Due to the detailed analyses of the lining and decomposition of the deformations it was possible to closely compare the numerical results with experimentally obtained data. Rotations in the joints as well as strains measured on the concrete surfaces are found to match almost exactly with FE results simulating the first experiment. By simulating the rotational behaviour of the segment joints it is found that the used Janssen concept may be used, with reduced initial stiffness according to earlier performed experiments. It is shown that there is a substantial contribution of the tension softening branch to the load bearing capacity of the lining.

The second experiment is characterized by a low axial force and by cracked segments at the start of loading. To simulate this experiment the first experiment is simulated to obtain a damaged lining after which the slip level of the interface elements is adjusted. By performing several calculations it turned out that a slip level of  $50 \text{ kN}$  to  $70 \text{ kN}$  results in an acceptable estimate of the load bearing capacity. The strains in the concrete segments and the rotations in the joints again show a good agreement compared to the experimentally obtained data.

# Samenvatting

Door bevolkingsgroei en toenemende vraag naar mobiliteit in Nederland groeit de interesse naar ondergrondse constructies. De beperkte hinder tijdens constructie en gebrek aan ruimte in dicht bebouwde gebieden leidt tot het steeds aantrekkelijker worden van geboorde tunnels. Metingen in de eerste tunnels die op deze manier in Nederland zijn gebouwd lieten zien dat spanningen tijdens de constructie aanzienlijk hoger waren dan oorspronkelijk gedacht. Vanwege deze metingen en onverwachte schades in gebouwde tunnels is een proefopstelling geplaatst bij de Technische Universiteit Delft waarin tunnelringen op ware grootte beproefd konden worden. Het initiale test programma was gericht op het vergaren van data voor het valideren van EE modellen onder gebruiksbelastingen en om het effect van enkele specifieke constructiestappen op het globale gedrag te onderzoeken.

Recent uitgevoerde experimenten waren gericht op het verkrijgen van inzicht in het constructieve gedrag van de lining onder ovaliserende belastingen in de uiterste grenstoestand. Voor het bepalen van de effectiviteit van de ringvoegen en de interactie tussen naastliggende ringen zijn twee verschillende proeven uitgevoerd. In de eerste proef is een hoge axiale kracht aangebracht in tegenstelling tot de tweede proef waarin een lage axiale kracht is aangebracht. Het doel van dit rapport is het opdoen van kennis in het constructieve gedrag van de lining in de uiterste grenstoestand. Om dit te bereiken wordt in dit rapport begonnen met een beschrijving van het theoretische en experimentele gedrag van zowel langs- als ringvoegen. Verschillende bezwijkmechanismen met betrekking tot het falen van de lining als ook het falen van de achterliggende grond worden beschreven.

Voor het verkrijgen van een helder beeld van de vervormingen en voor het verduidelijken van het gedrag van de lining gedurende de twee experimenten, vooral tijdens bezwijken, is de vervormde toestand van de lining voor elke belastingsstap berekend. Deze berekeningen zijn gebaseerd op de gemeten rotaties in de voegen en de gemeten krommingen in de segmenten. De ovaliserende vervormingen zijn vervolgens opgedeeld in een aandeel voegrotaties en een aandeel segmentkrommingen. De berekende vervormingen blijken goed overeen te komen met extern gemeten ovalisaties in de lineaire tak van belastingen. Afwijkingen in de niet-lineaire tak geven een indicatie voor het niveau van scheurvormingen van de segmenten in een ring.

Tijdens het belasten van de eerst uitgevoerde proef, waarin een hoge axiale kracht aanwezig was, bleek dat de vervormingen in de bovenste en onderste ring voornamelijk bestonden uit rotaties in de voegen en krommingen in de segmenten. Voegrotaties in de middelste ring waren significant lager en een aanzienlijk deel van de vervormingen werd veroorzaakt door scheurvormingen in de segmenten. Door de hoge wrijvingscapaciteit van de ringvoegen was het voor de segmenten in de middelste ring mogelijk om additionele buigende momenten,

afkomstig uit naastliggende ringen, op te nemen. Deze segmenten konden daardoor belast worden totdat de buigcapaciteit bereikt werd bij  $36 \text{ kN/Jack}$ . Bezwijken is daarbij geniteerd door scheurvorming in de kritieke segmenten in de middelste ring en een doorgaande rotatie van de voegen in naastliggende ringen.

In de tweede proef was een lage axiale interactie aanwezig waardoor een plotselinge toename in verplaatsingen bij een belasting van  $22 \text{ kN/Jack}$  werd waargenomen. De triplex plaatjes tussen de ringen waren niet in staat om de additionele buigende momenten in de langsvoeegen over te brengen naar naastliggende segmenten. Alvorens de kritieke segmenten tot hun buigcapaciteit belast konden worden werd de schuifkracht in de ringvoegen bereikt en bezweek de lining.

Uit numerieke analyses van een enkel tunnel segment werd het duidelijk dat vanwege een laag wapeningspercentage de buigcapaciteit van de betonnen segmenten sterk afhankelijk is van de eigenschappen van het beton onder trek. Als gevolg van de mesh afhankelijkheid en als gevolg van de onbekende softening eigenschappen, zijn vier verschillende combinaties van materiaal eigenschappen voor het modelleren van beton gebruikt en later gecomplementeerd in het complete tunnel model.

Om het gedrag van de lining beter te begrijpen is een 1D EE model ontwikkeld. Dit model bestaat uit drie ringen elk opgebouwd uit 7 segmenten en 1 sluitsteen. De segmenten zijn gemodelleerd met balk elementen en met interface elementen die de triplex plaatjes representeren, waarbij aan beide onderdelen niet-lineaire eigenschappen zijn toegekend. De segmentvoegen zijn gemodelleerd door gebruik te maken van een enkel balk element welke de rotatie eigenschappen volgens Janssen bezit. Om de numerieke berekeningen te valideren is een meer geavanceerd 2D model ontwikkeld waarin de voegen en de spanningen gedetailleerd geanalyseerd kunnen worden. De vervormingen in de segmenten en de rotaties in de voegen blijken goed met elkaar overeen te komen. De ontwikkeling van scheurvorming lijkt beter beschreven te worden door het 2D model. Vanwege de korte berekeningstijd en de interpreteerbaarheid van de resultaten is het 1D model gebruikt bij de verder uitgevoerde simulaties.

Door de gedetailleerde analyse van de lining en het scheiden van vervormingen in een aandeel voegrotaties en een aandeel segmentkrommingen is het mogelijk om de numerieke resultaten nauwkeurig te vergelijken met de experimenteel verkregen data. Rotaties in de voegen als ook de rekken gemeten op de betonnen segmenten blijken goed overeen te komen met resultaten van het EE model bij het simuleren van de eerste proef. Het is bewezen dat de Janssen relatie, met gereduceerde initiale stijfheid zoals gebleken uit eerder uitgevoerde proeven, gebruikt kan worden. Ook is aangetoond dat de eigenschappen van beton onder trek een aanzienlijke bijdrage leveren met betrekking tot de draagkracht van de totale lining.

De tweede proef wordt gekenmerkt door een relatief lage axiale belasting en het al gescheurd zijn van enkele segmenten. Om deze proef met een EE model te simuleren moet eerst de beschadigde lining worden verkregen door de eerste proef te simuleren waarna de schuifsterkte van het triplex wordt aangepast. Door vervolgens enkele berekeningen uit te voeren waarin de schuifsterkte van het triplex wordt gevarieerd is de schuifsterkte geschat op  $50 \text{ kN}$  tot  $70 \text{ kN}$ . Wederom komen de rekken in de betonnen segmenten net als de rotaties in de voegen goed overeen met experimenteel gevonden waarden.





# Contents

<b>I</b>	<b>Literature Survey</b>	<b>xv</b>
<b>1</b>	<b>Introduction</b>	<b>1</b>
1.1	Background . . . . .	1
1.2	Problem statement and objective . . . . .	2
1.3	Outline . . . . .	2
<b>2</b>	<b>General introduction to shield driven tunnels</b>	<b>5</b>
2.1	Tunnel lining . . . . .	5
2.1.1	Concrete segments . . . . .	5
2.1.2	Segment joints . . . . .	7
2.1.3	Ring joints . . . . .	7
2.2	Forces in a segmented tunnel . . . . .	9
2.2.1	Ring action . . . . .	10
2.2.2	Beam action . . . . .	10
2.2.3	Structural design models . . . . .	11
2.3	Theoretical behaviour of segment joints . . . . .	12
2.3.1	Moment-rotation relation according to Janssen . . . . .	13
2.3.2	Moment-rotation relation according to Gladwell . . . . .	14
2.4	Theoretical behaviour of ring joints . . . . .	17
2.5	Experimental research . . . . .	18
2.5.1	Segment joints . . . . .	18
2.5.2	Ring joints . . . . .	20
<b>3</b>	<b>Ultimate Limit State analysis</b>	<b>25</b>
3.1	Failure mechanisms of lining due to ovalisation . . . . .	25
3.2	Snap through of a joint . . . . .	26
3.3	Non-linearities . . . . .	27
<b>II</b>	<b>Analysis of Test Data</b>	<b>29</b>
<b>4</b>	<b>Description of tests and test set-up</b>	<b>31</b>
4.1	Load on the lining . . . . .	32
4.2	Conducted measurements . . . . .	33
4.3	Earlier performed tests . . . . .	35

<b>5</b>	<b>Experimental results</b>	<b>37</b>
5.1	Ovalisation deformation of lining . . . . .	37
5.2	Global observed lining behaviour . . . . .	42
5.2.1	Experiment C01 . . . . .	44
5.2.2	Experiment C02 . . . . .	47
5.2.3	Comparing experiment C01 and C02 . . . . .	48
<b>6</b>	<b>Critical Cross-Sections</b>	<b>51</b>
6.1	Compression strains in experiment C01 . . . . .	51
6.2	Compression strains in experiment C02 . . . . .	54
<b>III</b>	<b>Numerical Analysis</b>	<b>55</b>
<b>7</b>	<b>Numerical analysis</b>	<b>57</b>
7.1	Finite element modelling . . . . .	57
7.1.1	Different element types for the modelling of a tunnel lining . . . . .	57
7.1.2	Results of earlier constructed FE models of tunnel linings . . . . .	61
7.2	Single tunnel segment . . . . .	62
7.2.1	Bending moment-curvature relation of a tunnel segment . . . . .	62
7.2.2	Softening behaviour of concrete . . . . .	65
7.3	Simplified tunnel model . . . . .	71
<b>8</b>	<b>Description of FE Models</b>	<b>75</b>
8.1	1D FE model . . . . .	75
8.1.1	Geometry of FE Model . . . . .	75
8.1.2	Material properties of FE Model . . . . .	78
8.2	2D FE Model . . . . .	80
8.2.1	Geometry of FE Model . . . . .	80
8.2.2	Material properties of FE Model . . . . .	83
<b>9</b>	<b>Results of FE calculations</b>	<b>85</b>
9.1	Comparison between the 1D and 2D FE models . . . . .	85
9.2	Results of 1D FE analysis compared to experimental results of C01 . . . . .	89
9.2.1	External deformations . . . . .	89
9.2.2	Compression strains . . . . .	90
9.2.3	Segment joint rotations . . . . .	92
9.2.4	Additional capacity of segment joints . . . . .	93
9.2.5	Cracking pattern . . . . .	95
<b>10</b>	<b>Structural behaviour of the lining</b>	<b>97</b>
10.1	Experiment C01 . . . . .	97
10.1.1	Redistribution of bending moments . . . . .	97
10.1.2	Increase of normal force . . . . .	100
10.1.3	Load bearing capacity of the lining . . . . .	102
10.1.4	Ring interaction . . . . .	103
10.2	Experiment C02 . . . . .	105
10.2.1	Redistribution of bending moments . . . . .	107

10.2.2 Ring interaction . . . . .	108
<b>11 Conclusions and recommendations</b>	<b>111</b>
11.1 Conclusions . . . . .	111
11.2 Recommendations . . . . .	112
<b>Bibliography</b>	<b>115</b>
<b>IV Appendices</b>	<b>119</b>
<b>A Numbering and positioning of measurement devices</b>	<b>121</b>
<b>B Calculation deformations of lining</b>	<b>125</b>
<b>C Deformations of lining in experiment C01</b>	<b>129</b>
<b>D Deformations of lining in experiment C02</b>	<b>133</b>
<b>E Ovalisational deformation of lining</b>	<b>137</b>
<b>F FE results compared to experimentally obtained data</b>	<b>143</b>
<b>G Validating numerical analysis of a single tunnel segment</b>	<b>153</b>
<b>H Comparison of bending moments between experiment C01 and C02</b>	<b>157</b>
<b>I Data on CD</b>	<b>161</b>



# List of Symbols

$E$	Young's modulus	$[N/mm^2]$
$E_{steel}$	Young's modulus of reinforcement steel	$[N/mm^2]$
$F_n$	Normal force in a segment	$[N]$
$F_{Shear}$	Shear strength of plywood sheet	$[N]$
$G_f$	Fracture energy	$[Nm/m^2]$
$N_{ovalisation}$	Normal force due to non-uniform radial load	$[N]$
$S_{r,max}$	Maximum crack spacing	$[mm]$
$W$	Crack width of concrete	$[mm]$
$b$	Width of a segment	$[mm]$
$c$	Concrete cover to the reinforcement	$[mm]$
$d$	Distance between LVDT's located on a joint	$[mm]$
$d_{max}$	Maximum aggregate size	$[mm]$
$f_t$	Tensile strength concrete	$[N/mm^2]$
$h$	Height of the reduced joint thickness	$[mm]$
$h_{cr}$	Crack bandwidth	$[mm]$
$k_1$	Coefficient which takes account of the bond properties of the bonded reinforcement	$[-]$
$k_2$	Coefficient which takes account for the distribution of strain	$[-]$
$m$	Enlargement factor joint rotations	$[-]$
$t$	Segment thickness	$[mm]$
$\beta$	Shear retention factor	$[-]$
$\epsilon_u^{cr}$	Ultimate crack strain	$[-]$
$\phi$	Bar diameter	$[mm]$
$\mu$	Friction coefficient	$[-]$
$\nu$	Lateral contraction coefficient	$[-]$
$\sigma_y$	Yield stress of reinforcement steel	$[N/mm^2]$



Part I  
Literature Survey



# Chapter 1

## Introduction

### 1.1 Background

In 1994, the Dutch government established the Centre for Underground Buildings (COB) to explore the possibilities for underground constructions in the Netherlands. One of the structures with a high potential in crowded areas are segmented tunnels, but are difficult to accomplish in soft soils. To gain knowledge on the behaviour of segmented tunnels, different shield driven tunnels, which were experimental, were financed. The first tunnel constructed this way was the Second Heinenoordtunnel in 1997. During the construction of this project a lot of measurements were performed to provide information on how the tunnel was behaving in Dutch soil. Analysis of the strain distribution during construction showed that stresses were higher than expected. In the second tunnel constructed, the Botlek Railway Tunnel, damages appeared which could not be explained very well.

For gaining better insight in the structural behaviour, the project organisation High Speed Line and the management group Betuweroute decided to conduct a series of full-scale tests. In 1999, a test set-up, consisting out of three rings of the Botlek Railway Tunnel, was built in the Stevin laboratory at the Delft University of Technology. In this facility, research was performed on the behaviour of the lining under construction and service loads. Obtained data was analysed and compared to Finite Element Models which led to the improvement of the prediction of lining behaviour. This knowledge resulted in better segment design and was valuable for the design and construction of other tunnelling projects to come.

After a few years the facility was handed over to TNO Built Environment and Geosciences and the TU Delft to extend the research. Tests followed in which basic load cases and the effects of inaccurate placed segments were studied. Measurements were evaluated and detailed analyses were made, numerical models were validated and more knowledge on concrete linings was obtained.

At the same time plans for more shield driven tunnels were undertaken and construction of those projects started. During the construction of projects like the Sophia Railway Tunnel, Western Scheldt Tunnel, Green Heart Tunnel and the tunnel underneath the Pannerdensch canal a lot of new experiences regarding the execution were gained from which many things were learned.

During earlier tests it became clear that the joints have a large influence on the global behaviour of the lining. Because these tests were performed in the Serviceability Limit State no insight in the Ultimate Limit State was obtained. To get insight in the behaviour of the lining during extreme loading, the experiments were extended with a series of tests in the Ultimate Limit State. Two tests were performed in which the lining was loaded by different axial loadings, both with a uniform radial load followed by a non-uniform radial load.

## 1.2 Problem statement and objective

Most experiments in the full-scale test facility at the TU Delft were performed in the Serviceability Limit State. In order to assess the safety level of a concrete lining, and the ultimate load capacity, tests have been performed in the Ultimate Limit State. An important aspect in the behaviour of the lining is the interaction between the concrete segments. The question is how neighbouring rings and segments interact. Depending on the degree of cooperation, every separate ring carries the radial load on its own or exchanges forces to adjoining rings. In the first case, segment joints will be governing. In the second case, the segments itself will be governing for the ring behaviour. The goal of this master thesis is to gain understanding in the behaviour of the concrete lining in the Ultimate Limit State. What is the influence of the joints and how can this be modelled? What are the failure mechanisms and when do they occur? To gain this knowledge, test results are analysed and a FE model is developed. To achieve this, theoretical models for the segment joints and properties of packing materials are studied. With the aid of the developed FE model and the available test results, the influence of the joints and the interaction between rings on the ultimate load capacity is further analysed.

## 1.3 Outline

This thesis is divided into three sections. The first section elaborates on the literature available regarding tunnel design. The second section is an analysis of obtained test data. Finally, in the third section, a FE model is described and results are analysed.

To get a good impression of the studied subjects a literature study is performed. Chapter 2 starts with the treatment of the global forces on a segmented lining followed by a short description of the composition of a lining. The behaviour of the segment- and the ring joints is treated as well as the properties of the different packing materials. The various existing theoretical models for the behaviour of the joints are described. Also the behaviour of the joints and the packing materials during experiments is summarized. In chapter 3 some considerations are given regarding failure mechanisms of the lining and failure mechanisms of the surrounding soil.

The second section presents an analysis of the obtained test data. Chapter 4 starts with the description of the test set-up and the performed measurements followed by a review regarding earlier performed experiments. In chapter 5 the global observed lining behaviour is elucidated and in chapter 6 the test data is analysed in more detail. This data is collected mainly during two experiments focusing on the behaviour of the lining in the ULS. The behaviour and failure

of the concrete lining is analysed in detail at which most attention is paid to the behaviour of the joints and their effect on the migration of forces to adjoining rings.

The third section elaborates on the FE calculations. After a general introduction to FE analyses, the most important aspects regarding tunnel modelling are discussed, like mesh dependency and the behaviour of a single tunnel segment in chapter 7. The geometrical as well as the physical properties of a 1D beam model and a 2D plane stress model are described in chapter 8, followed by a comparison of the results of both models in chapter 9. The FE models are compared to experimentally obtained results after which the structural behaviour of the tunnel is analysed in more detail in chapter 10.

Throughout the report, references to segments and joints are made. It is very difficult to get a clear picture in mind of the different parts of the model due to the three dimensional configuration of the lining. Therefore, it is not always instantly clear what is meant by certain references. To be able to better understand this report, it is useful to make a scale model of the lining before reading it. In appendix A an A4-paper is included from which a scale model can be folded.

In appendix I the content of the enclosed CD is described. On this CD the Excel sheets used to calculate the deformed shape of the lining, the experimentally collected data and the DIANA data and command files are found.



## Chapter 2

# General introduction to shield driven tunnels

### 2.1 Tunnel lining

In a tunnel a lining is needed to withstand soil- and water pressures. Previously, most tunnels in the Netherlands were constructed using the cut and cover or sink method. Due to hindrance during construction of an immersed tunnel and lack of space in populated areas, the shield driven method became more popular. These shield driven tunnels are segmented because of the soil conditions and are constructed mainly from reinforced concrete segments. The excavation of the ground and the placement of the segments is carried out by a Tunnel Boring Machine [Bickel et al. 1996]. Between the segments in a ring the segment joints are situated and between two rings ring joints are situated. In the succeeding paragraphs the main parts of the lining and their functions are treated.

#### 2.1.1 Concrete segments

The elements are prefabricated within rather tight tolerances. The dimensions of a segment are chosen to be as large as possible, resulting in a minimum number of segments per ring, with the aim of optimising the speed at which the tunnel boring machine advances. Also the available space for transport and placement of the segments, as well as the maximum possible extension of the jacks, determine the dimensions of the segments.

The thickness of the concrete segments is determined by the global structural behaviour of the lining and the magnitude and configuration of the applied jack forces coming from the TBM. The concrete segments are positioned in stretched bond. In this configuration there is no ongoing joint in axial direction. If a strong interaction between rings is present, bending moments in segment joints are transferred to segments in adjacent rings. This way the rotation of segment joints is limited. Definitions mostly used in tunnel engineering are represented graphically in figure 2.1.

In case of the Botlek Railway Tunnel 8 segments per ring are used, subdivided in 5 normal segments, 2 counter segments and 1 key segment. The key segment is placed last and preferably near the top of a ring. The key element is wedge shaped (tapered) and smaller which

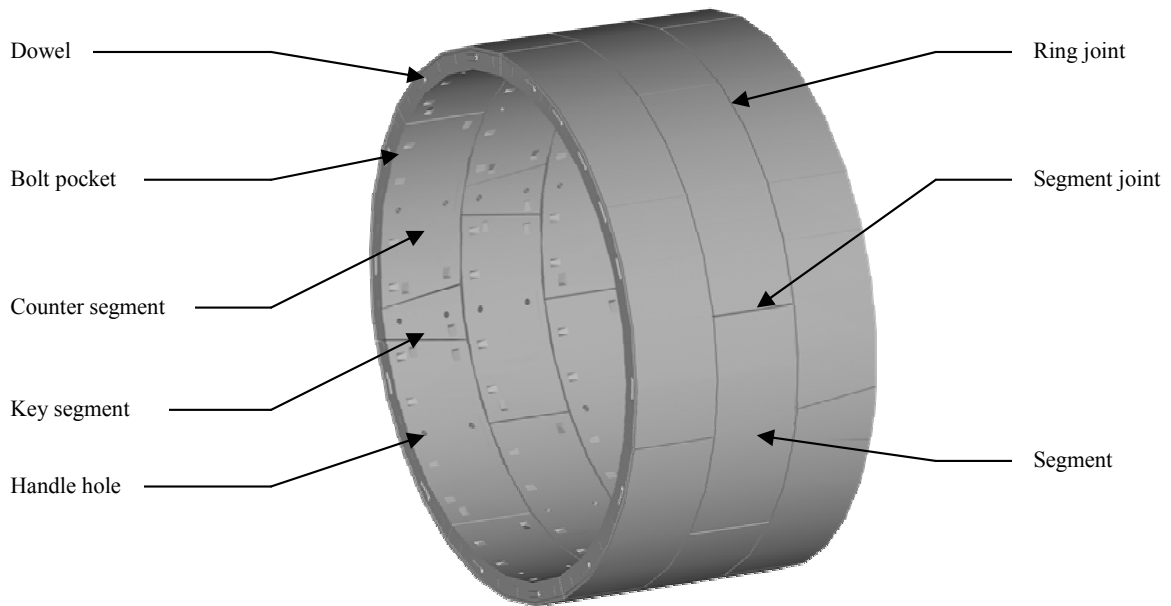


**Figure 2.1:** Lining defenitions

makes its placement easier. The front face of a complete ring is not parallel to its back face to be able to construct a curved alignment. This is shown exaggerated in figure 2.2.

The concrete segments are prefabricated and lightly reinforced to withstand bending moments and splitting forces. These forces not only occur in the SLS but also during transport and placement. Additional reinforcement is put on places where jack forces are introduced, handle and bolt holes are located and around dowels.

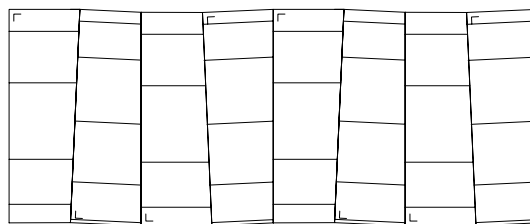


**Figure 2.2:** Alignment of the lining

During construction the axial force is not present all the time. Alternately some jacks have to be withdrawn to create space for the placement of a new segment. This will result in a local temporarily loss of axial pressure leading to poor connections between some segments. To ensure the segment positions, bolts are applied in the joints. After having assembled a few rings, the withdrawal of jacks at the boring front will have no effect on axial forces in the behind laying rings. At that moment the bolts become unnecessary and are removed for making sure that they do not affect the structural behaviour.

### 2.1.2 Segment joints

The contact line between succeeding segments in a single ring is indicated as a segment joint. In practice, two different types of segment joints are used. The plane joint and the convex joint which are illustrated in figure 2.3. The main difference between the convex and plane joint is the ability to transfer bending moments. When in case of a plane joint a rotation occurs, a moment, induced by normal forces, will try to close the gap. This means that a plane joint is able to transfer bending moments. The disadvantage is that when large rotations occur, the exterior parts of two segments make contact. This point contact will lead to damage and water tightness is not longer guaranteed. When large rotations are expected a convex joint can be considered which possesses a curved contact area. Caused by its geometry no moments will be transferred and the joint will act like a hinge.

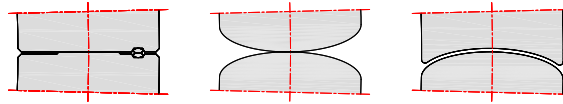


**Figure 2.3:** Plane joint (left) and two convex joints (middle and right)

In Baumann (1992) the behaviour of a plane and convex joint is described roughly. The field of application for both joints is formulated depending on allowable joint rotations and normal forces present in the lining. Having large joint rotations and large normal forces a convex joint is preferable, because the risk of spalling of the concrete is limited. Due to a wider compression zone of the concrete when a plane joint is applied, this joint will be more preferable having small joint rotations and small normal forces. Existing tunnels in the Netherlands are carried out with plane joints and having a limited width of the contact area.

In case of a plane joint, contact between two segments in a ring is mostly established by concrete-to-concrete surface contact without packing material. This contact area will have a reduced thickness in comparison with the segmental thickness. Through this contact area the normal force will be introduced concentrated into the next segment.

Water tightness is provided by rubber gaskets. These gaskets are situated at the exterior part of the joint. When a large rotation occurs the gaskets will be pressed or unpressed, depending on its direction of rotation. When the gasket is unpressed, water is able to leak through the joint. When this water contains surrounding soil this can lead to a decrease of support by the ground and may cause failure.

### 2.1.3 Ring joints

In between two adjacent rings a ring joint is situated. Contact between two rings is established, in two to five contact areas per segment, by concrete-to-concrete contact or via packing materials. To prevent large deformations, segments are also equipped with dowels and sockets. Different configurations for dowels and sockets are available. Small, non constructive, dowels and sockets can be applied to make placement of the segments easier. They are not reinforced and do not prevent large deformations. Under normal load conditions there will be no contact between the dowels and sockets. Between the concrete surfaces kaubit is used

to avoid damage of the concrete which might attack its durability.

When the normal contact areas are not able to resist the shear forces, large deformations will take place. To prevent failure of the lining, structural dowels and sockets are applied. To be able to carry the loads the dowels are reinforced and their dimensions are larger. In radial and tangential direction generally a margin between the dowel and socket is present. In tangential direction this margin is relatively large which will result in no interaction between rings in this direction. In radial direction the margin is smaller but only when deformations become to large shear forces will be carried by the dowels and sockets. Again, in most cases, kaubit is used as a packing material to avoid damage when the two surfaces make contact.

The main contact between two rings is established by concrete-to-concrete contact or by packing materials. These contact areas are located at several areas along the edge of a segment. Concrete-to-concrete contact can introduce local peak stresses due to an unsmooth surface. To prevent this from happening a packing material is mostly applied. In practice, plywood or kaubit is placed between the two concrete surfaces as can be seen in figure 2.4. This packing material will introduce the axial, tangential and radial force into the next ring. These contact areas are placed in line with the hydraulic jacks coming from the TBM in order to get a good transition of axial jack forces to adjacent rings.



**Figure 2.4:** Tunnel segments with kaubit used as a packing material (left) and plywood used as a packing material (right)

**Plywood as a packing material** When different deformations between the segments in two adjoining rings occur a shear force will develop in the plywood. Via friction between the concrete and the plywood, cooperation between two rings will be established. The shear strength of this connection is dependent on the axial force present in the lining and the friction coefficient between concrete and plywood. Unknown are the long term effects regarding durability. More properties of plywood as a packing material in ring joints are described in Gijbers and Hordijk (1997).

**Kaubit as a packing material** A bituminous material can also be placed in between two concrete segments. This material, with a very low stiffness, will deform extremely when compressed. The material will be squeezed until a rest thickness of approximately 0,2 mm remains. When increasing the normal forces, the kaubit will be squeezed more resulting in a

larger contact area. Because the concrete surface is not perfectly smooth, and almost no rest thickness of the kaubit is left, concrete-to-concrete contact can occur resulting in a dramatic change of the friction coefficient which may affect ring interaction extremely.

## 2.2 Forces in a segmented tunnel

Forces in a tunnel are caused by loadings on the tunnel during construction and usage. During construction a lot of parameters affect the load conditions. The TBM will disturb ground and water pressures and will put a large axial force on the tunnel lining by its jacks to push itself forward. Behind the cutting wheel, grout is injected to close the gap between concrete lining and surrounding soil. The tunnel will float in this grout when it is liquid and it will support the lining when it is hardened. All these factors determine the resulting force on the lining in the construction stage and eventually it might also have its influence on forces during usage. A compact description of primary forces on the lining is given below. An extended coverage of forces on a lining is found in Frissen et al. (1997).

Acting forces on a tunnel lining can be subdivided in axial, radial and tangential direction. The axial force is caused by the applied jack forces during construction. To move the TBM forward, these forces have to be large enough to overcome the pressure at the boring front and friction between the TBM and soil. Subsequently the hydraulic jacks introduce this force onto the segments in the latest ring build. Depending on the configuration used, 2 to 4 jacks per segment are applied. The concentrated axial forces are spread in the segments and via ring joints these forces are once again introduced into adjoining rings. Stresses due to the jack forces decrease in time, because of time dependent effects like creep and relaxation of the concrete and packing materials. How this axial force develops in time is not exactly known but is estimated to be eventually 80 percent of the initial applied force [Koek 2004].

When constructing a tunnel below the water table, a water pressure is present and only acts in radial direction on the lining. A low water table results in a low uniform radial load resulting in a relatively high ovalisation load on the lining and is therefore governing in design. Also the possibility of floating has to be omitted. When not enough overburden is present it can be a problem to fulfil equilibrium.

Soil around the tunnel can load or unload (support) the lining. Depending on the deformations of the lining, active or passive ground forces act on the lining. Undisturbed soil conditions are generally used to determine soil pressures. Differences in vertical and horizontal core pressures will result in a non-uniform load around the circumference. There are different ways to model the interaction between lining and surrounding grout. Discrete springs can be placed around the lining or a soil continuum can be modelled. The resulting soil forces on the lining can be subdivided into a radial and a tangential component.

The concrete segments are assembled inside the TBM. These segments are placed on the inside part of the exterior steel shield of the TBM until a complete ring is formed. When the TBM moves on, the segments are pushed out of the protected shell and will gradually be exposed to the surrounding grout. Caused by differences in diameter of the steel shield and concrete lining, a gap will form on the exterior part of the concrete lining behind the

TBM. This tail void has a thickness of approximately 10 to 15 centimetres. To prevent soil settlements this gap is injected with grout which has the same or a little bit higher pressure than the surrounding soil. Because the force distribution along the circumference of the lining is very important, the injecting of grout should be performed in such a way that no negative effects on internal lining forces are introduced [Blom 2002]. In practice, this is hard to achieve and even harder to measure. Mostly it is assumed that the grout pressure is symmetrically hydrostatic around the lining. When injected properly, the grout increases the capacity of a lining. When recently injected, the water cement mixture is still liquid and causes an uplift force which can result in floating of the lining and might cause additional stresses in the lining. From observations during the construction of the Second Heinenoordtunnel it was proved that additional stresses were introduced caused by floating of the lining. The axial normal pressure in segments situated at the top were larger compared to the pressures found at the bottom [Vervuurt and Gijsbers 1999]. At greater distance from the TBM a decrease of this pressure was observed. This indicates that the lining undergoes an upward force just after injecting. Extended analysis of the effect of grouting on the lining can be found in Peters and Zafari (2000).

### 2.2.1 Ring action

In foreign countries most attention is paid to the behaviour of a single ring during design. Because of the stretched bond layout of segments, non-uniform displacements between two rings occur, resulting in an interaction. In that case, two adjoining rings are modelled and analysed. Because the load everywhere along the track is the same, the tunnel can be designed based on this analysis.

### 2.2.2 Beam action

Varying and soft soil conditions in the Netherlands may lead to non-uniform settlements. When tunnelling through this soil the lining is loaded differently in axial direction. Effects of these settlements on the lining can only be analysed when multiple rings are modelled. The analysis of these varying load conditions in axial direction is called the beam action of a lining. Only limited research is performed on the effects of these settlements and how this can be modelled [Blom 1995] [Van Empel 1998]. Effects like opening and shear of the ring joints, force introduction into segments and the influence of dowels and sockets have to be included. In Visschedijk (1998) three dimensional beam and shell models are implemented in which the ring joints are included. With these numerical models the effects like bending moments in axial direction and shear of adjoining rings can be analysed very well. Also the opening of ring joints can be investigated.

A simplified method for determining the forces caused by non-uniform settlements is a beam continuously supported by springs, figure 2.5. These models cannot simulate the opening of ring joints but they can predict bending moments in the lining in axial direction. To get reliable answers equivalent material properties, determined from more complex analysis, have to be assigned to the beam.

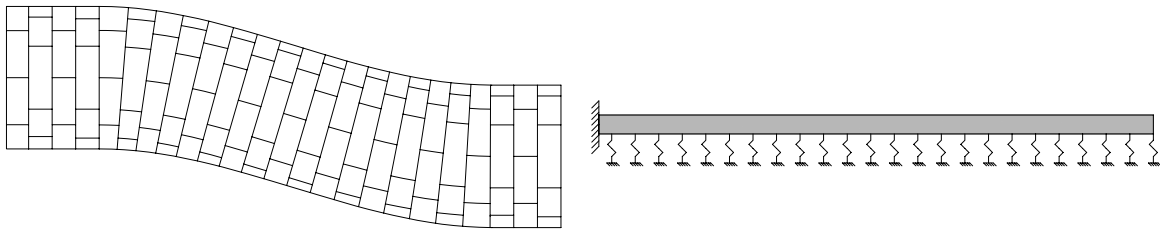


**Figure 2.5:** Deformation of lining (left) and simplified modelling of beam action (right)

### 2.2.3 Structural design models

Different methods are available for designing a tunnel. From practice, the need for analytical models is still present to get insight in the effects of different parameters. The problems with these models arise when incorporating soil-lining interaction. Various analytical models have been developed in time. Distinctions can be made between embedded and continuum models, figure 2.6.

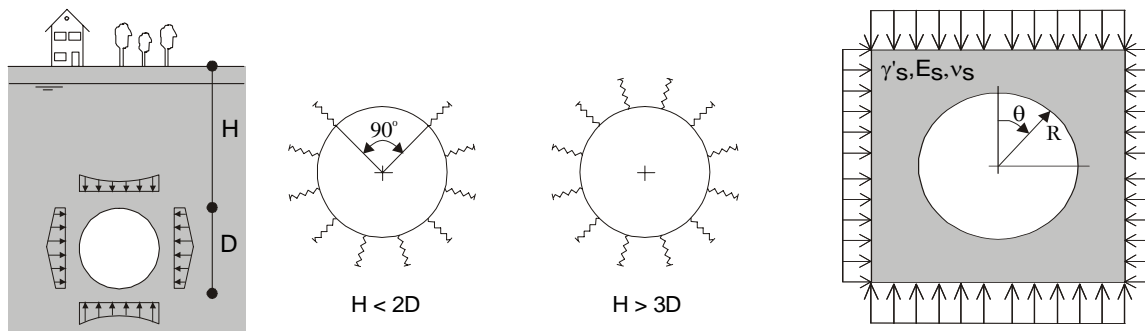


**Figure 2.6:** Embedded spring model (left) and continuum model (right)

In 1964, Schulze and Duddeck developed a spring supported ring model. In this embedded model the lining-ground stiffness relation is incorporated, as well as the influence of the radius and the depth of the tunnel. The ground support is modelled with radial and tangential discrete springs along the circumference of the lining. The ring itself is homogeneous using the linear elastic shell theory. With the aid of some simple equations the radial and tangential load on the lining is derived from the primary pressures in the undisturbed soil. Subsequently the maximum normal forces and moments, due to ovalisation, can be found in a graph developed by Schulze and Duddeck. These graphs are based on analytical as well as empirical (to incorporate for ground-lining interaction) calculations. Clay and peat are not in the field of application, so it is questionable whether this method can be applied in Dutch soil conditions [Postma 1997]. In the described model only one ring is taken into account without segment joints. To incorporate these joints an equivalent bending stiffness for the lining is applied to estimate deformations. For more accurate solutions the joints can also be modelled as hinges or rotational springs, but solutions can only be found numerically. Additional contributions to this model were done in succeeding years, like the contribution of geometrical non-linearities

[Windels 1966]. Refinements eventually resulted in the final paper of Duddeck [Duddeck and Erdmann 1982] in which a complete description of many design models is made. Blom (2002) also developed an analytical multiple segmented ring model including ring interaction and non-linear effects of segment joints.

To model the ground load on a tunnel lining more accurate, a continuum model may be used. A two dimensional rectangular elastic solid is modelled in which a cavity is included. These models give more information on forces in the surrounding soil. The stress distribution in the elastic soil around the cavity, as result of a uniform radial displacement or stress, is described by Mindlin (1940). Later on, solutions for compressible materials [Verruijt 1997] and ovalisation loads [Strack 2000] were found. Because these calculations are based on a predefined deformation of the lining, no soil-lining interaction is present. Mentioned documents do not incorporate the effects of boring and injection grout which will affect the soil and water pressures around the lining.

Most models described above only consider one ring. A German contractor (Wayss and Freitag) developed a double ring model in which adjacent segments are coupled by bars. When segment joints have different circumferential locations in adjoining rings this Wayss and Freitag model is more realistic. Disadvantage is that this has to be solved using numerical analysis, but still a lot of insight is gained caused by the simplicity of the model.

Detailed solutions can be produced when making finite element calculations. Ground and tunnel lining, segmented or continuous, can be modelled very precisely and interaction between soil and the segments can be analysed in detail. Also the non-linear behaviour of soil and lining can be taken into account. These models can be two or three dimensional and an advanced interaction between segments can be implemented. In these more sophisticated analyses it might be more difficult to provide insight and they are time consuming to develop.

## 2.3 Theoretical behaviour of segment joints

As previously emphasized, the joints in between the segments determine for the greater part the behaviour of the global lining. A good understanding of the joint behaviour leads to an improved understanding of test results and a more realistic analytical and numerical modelling. The behaviour of segment joints is significantly affected by the normal force present in the joint, caused by an uniform radial pressure on the lining. When bending moments stay low, there is a compression force on the entire cross-section of the joint. No gap will form and the bending moment only leads to minor additional rotations depending on the joint height and joint thickness. If the height of the joint is almost equal to the segmental thickness, no additional curvatures, leading to a rotation, will occur. However, when the height of the joint is very small compared to the segmental thickness and the joint thickness is relatively large, the curvatures in the joint will be high leading to large rotations in this still linear branch.

Only when the pressure on the outer side of the contact area becomes zero, a gap will form leading to major additional rotations. Theoretically, this transition is reached when the bending moment  $M = \sigma * W$ , in which  $\sigma$  is the stress caused by the normal force and  $W$  the

section modulus of the joint. After that point, a severe rotation in the joint develops. The capacity of the joint will theoretically be  $M = 1/2hF_n$  and is dependent on the height  $h$  of the joint and the normal force  $F_n$  present in the joint. The results of a FE calculation are shown in figure 2.7 in which the two different stages (linear and non-linear) can be recognised.

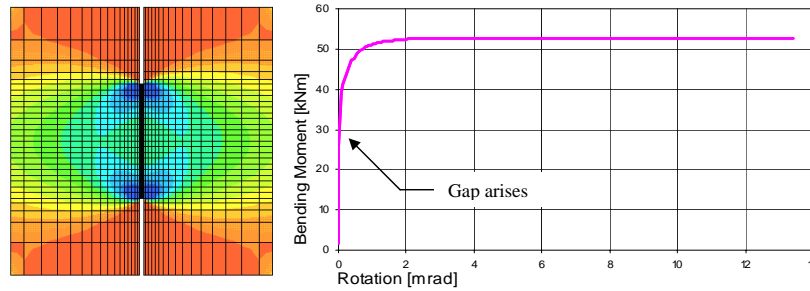


**Figure 2.7:** FE model of segment joint including stress distribution caused by a normal force (left) and rotation versus bending moment of the joint (right)

In the past, different theoretical models were developed to describe the joint behaviour with the aim of getting realistic analytical and numerical lining models. In the following paragraphs the Janssen and Gladwell relations are elucidated.

### 2.3.1 Moment-rotation relation according to Janssen

A simple theoretical model for describing the moment-rotation behaviour of segment joints was developed by Janssen (1983). In the derivation, linear elastic material properties and full concrete-to-concrete surface contact in the joint is assumed. Restraintment of the reinforcement and three dimensional effects are not accounted for.

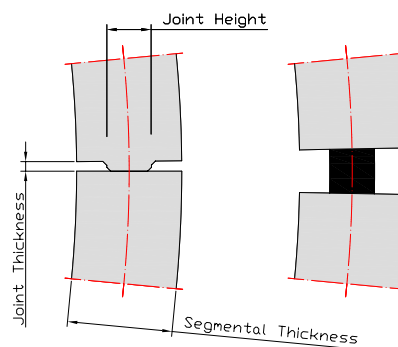


**Figure 2.8:** Modelling of a segment joint by Janssen, reality (left) and Janssen model (right)

Janssen represents the joint by an equivalent concrete beam in between two segments. This concrete element simulates rotations in the joint and additional curvatures in the two adjoining segments caused by the concentrated force introduction into the segments. To simulate the rotations the concrete beam is not able to take tension forces and has dimensions equal to the joint height, like drawn in figure 2.8. In the first branch of loading only compression stresses are present because of the normal force. In the equivalent 'beam' a curvature will develop resulting in a rotation. No tension is present and the joint stays closed. This is the linear

branch of the Janssen relation. In reality, when the joint is very thin, only a very minor additional rotation will occur. Because of the hypothesis that the joint has a length equal to the height of the joint, according to Janssen, a rotation will develop taken into account for the spread of load in the region of the joint. Regarding this, the Janssen relation will be more accurate when describing a thick joint. The linear moment-rotation relation is described by equation 2.1.

$$\text{linear} : \left\{ \phi = \frac{Mh}{EI} = 12 \frac{M}{Eh^2b} \right\} \quad M < 1/6F_n h \Rightarrow \quad \phi < \frac{2F_n}{Ehb} \quad (2.1)$$

$$\text{non-linear} : \left\{ \phi = \frac{8F_n}{9bhE \left( \frac{2M}{F_n h} - 1 \right)} \right\} \quad M \geq 1/6F_n h \Rightarrow \quad \phi \geq \frac{2F_n}{Ehb} \quad (2.2)$$

It is obvious that the stiffness of the joint is only affected by the Young's modulus of the concrete and the contact height of the joint. By increasing the bending moment, the joint will open and a non-linear relation will occur. This non-linear branch will start as soon as the normal force stays no longer within the core of the contact area. The transition between the linear and the non-linear branch occurs theoretically at  $M = 1/6F_n h$ .

After this moment a less stiff behaviour is reached. At the opening side of the joint the contact stresses are zero and a gap will form. In this non-linear branch the influence of the normal force is present. The non-linear branch of the Janssen relation is given by equation 2.2.

Rotations are prohibited by adjacent segments if a strong interaction in axial direction is present. When the moment reaches  $M = 1/2Nh$  the maximum moment capacity of the joint is reached which implies an eternal rotation. The Janssen relation is graphically represented in figure 2.9 for realistic geometrical properties of the joint.

In his derivation, Janssen considered a linear relation between strains and stresses. This constitutive relation is assumed to be bi-linear for concrete. Blom calculated the influence of this plastic behaviour of the concrete on Janssen's relation. For large rotations a reduced moment capacity compared to the original Janssen relation is found. When a large normal force is present, the maximum concrete strength is reached earlier, compared to the situation with a low normal force, resulting in an earlier decrease of rotational stiffness. In figure 2.9 it is clearly shown that this relation will not reach the theoretical maximum moment as derived previously. It has to be underlined that this reduced horizontal plateau will not always be reached and is dependent on the concrete strength, the normal force and the bending moment present in the joint.

### 2.3.2 Moment-rotation relation according to Gladwell

Janssen considered a linear stress distribution in the joint. From elasticity theory it is known that this is not correct. In reality, a non-linear stress distribution over the cross-section develops, where at the edge of the contact area the stresses reach infinity. Based on elasticity theory, Gladwell (1980) developed a relation between the moment and rotation between two flat surfaces, figure 2.10.

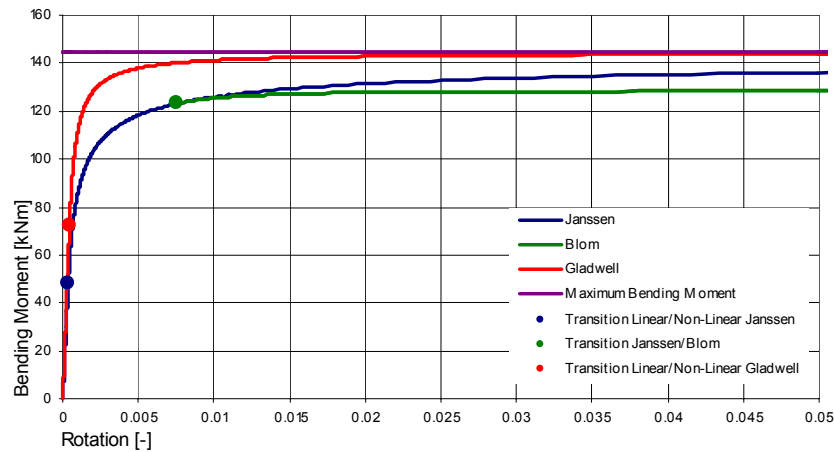


**Figure 2.9:** Moment-rotation relation according to Janssen, Blom and Gladwell (Normal force=1.700 kN, contact height joint=170 mm)

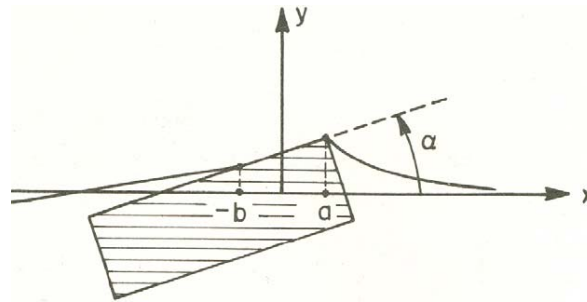


**Figure 2.10:** Flat punch pressed unsymmetrical into a half plane [Gladwell 1980]

Contact stresses concentrate on the edges of the joint. This results in a more stiff rotational behaviour compared to a linear stress distribution as can be seen in figure 2.9. Just like Janssen, a linear and a non-linear branch can be distinguished in the moment-rotation diagram. The initial Gladwell stiffness is higher and the joint stays closed longer compared to Janssen. The linear relation is given in equation 2.3 and the non-linear relation is given in equation 2.4. The Gladwell relation in the non-linear branch approaches the asymptotical bending moment more quickly than the Janssen relation as can be seen from figure 2.9. For larger rotations the two relations approach each other and will finally reach the same asymptotical bending moment.

$$linear : \left\{ M = 1/32 \frac{\pi h^2 b E}{1 - \nu^2} \right\} \quad M < 1/4 F_n h \Rightarrow \phi < \frac{8N(1 - \nu^2)}{2} \quad (2.3)$$

$$non - linear : \left\{ M = 1/2 h N - \frac{2b(1 - \nu^2)}{\pi h E} \right\} \quad M \geq 1/4 F_n h \Rightarrow \phi \geq \frac{8N(1 - \nu^2)}{2} \quad (2.4)$$

In Van Der Vliet (2006), 2D FE calculations of joints loaded by a normal force and a bending moment are presented. In the FE model the material properties are linear elastic and plane sections remain plane (Bernoulli). These analyses resulted in moment-rotation diagrams and

were compared to the Janssen and Gladwell relations. It turned out that the Gladwell relation is a very good approximation to the FE solution, but still there are some discrepancies. The Janssen relation showed a lower stiffness. The discrepancies are caused by the influence of the reduced contact thickness in relation to the segmental thickness and are mostly affected in the linear branch.

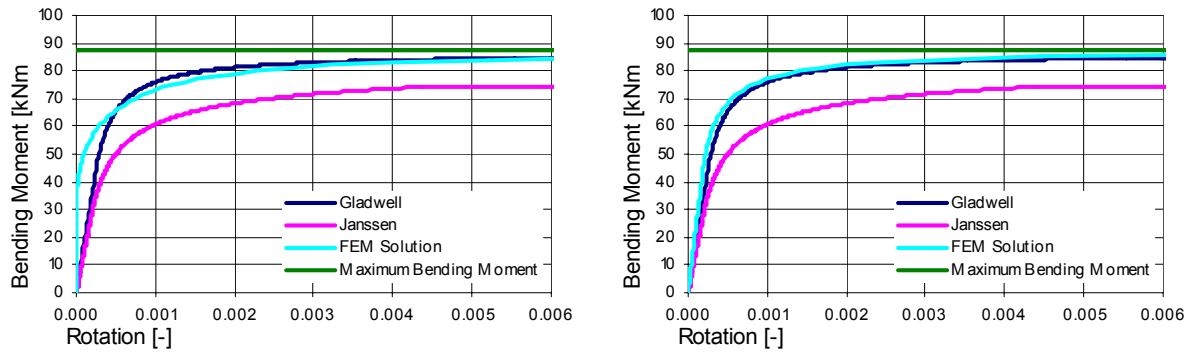


**Figure 2.11:** FEM Solutions compared to Janssen and Gladwell for  $\alpha = \frac{170}{170} = 1$  (left) and for  $\alpha = \frac{170}{400} = 0,4$  (right)

In the FE calculations the influence of the reduced contact height is included via a factor  $\alpha$ . The relation between the contact thickness and the segmental thickness is  $\alpha = \frac{\text{contact thickness}}{\text{segmental thickness}}$ . For several values of  $\alpha$ , FE analyses were carried out of which the results of two of them are shown in figure 2.11. When the segmental thickness is far greater than the contact thickness, the parameter approaches zero. In this theoretical case the Gladwell relation approximates the FE solution. When the segmental thickness is equal to the contact thickness, no rotations are found in case of low bending moments. This is obvious because practically no joint is present and no additional rotations occur when only compression stresses are present. When the joint starts to open, the relation will closely follow the Gladwell relation and will finally approach the same maximum bending moment.

The right graph in figure 2.11 is drawn for the geometrical properties of a joint present in the Botlek Railway Tunnel. For this situation the Gladwell relation shows a very good approximation of the FE solution and can be used for the modelling of a tunnel lining. It has to be emphasized that these curves are obtained only using analytical models and FE analysis and are not based on experimental results.

When rotations increase, the segments rotate more and more around the edge of the contact area. Increasing rotations even further will cause plastic behaviour and eventually this will lead to cracking of the concrete at this spot. Rotations can increase until the joint reaches a rotation of approximately  $0,045 \text{ rad}$  [Vervuurt 2006]. These analyses are carried out with geometrical properties of the Botlek Railway Tunnel. At that point the outer parts of the segments will touch resulting in strengthening. From there on the forces are mainly carried by the edges of the concrete segments. In figure 2.12 the extreme rotations of two segments and their effect on the moment-rotation relation is shown.

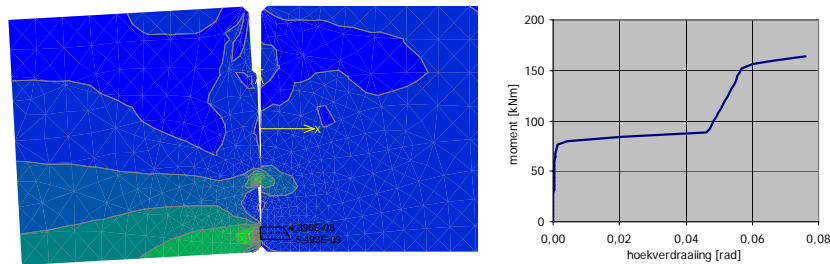


**Figure 2.12:** Extreme joint rotation resulting in touching of the outer edges of the segment (left) and bending moment-rotation relation (right)

In previously described relations, the non-linear branches are dependent on the normal force. Because of the ovalisation of the lining the normal force will have different values along the circumference of the lining. In the conducted experiments, the normal forces vary between  $964 \text{ kN}$  and  $1.072 \text{ kN}$  when an ovalisational load of  $36 \text{ kN/m}^1$  is applied per ring, possessing a width of  $1.500 \text{ mm}$ . This is the maximum applied ovalisation load which the lining is exposed to in the conducted experiments. The influence of these varying normal forces on the rotation according to Janssen and Gladwell is presented in figure 2.13. The bending moments reach a 10% discrepancy. However, when the bending moment is known and a rotation has to be found, the discrepancies are very severe depending on the stage of non-linearity. Incorporating the effect of variable normal forces along the lining has to be considered in relation to the accuracy of a Janssen or Gladwell relation.

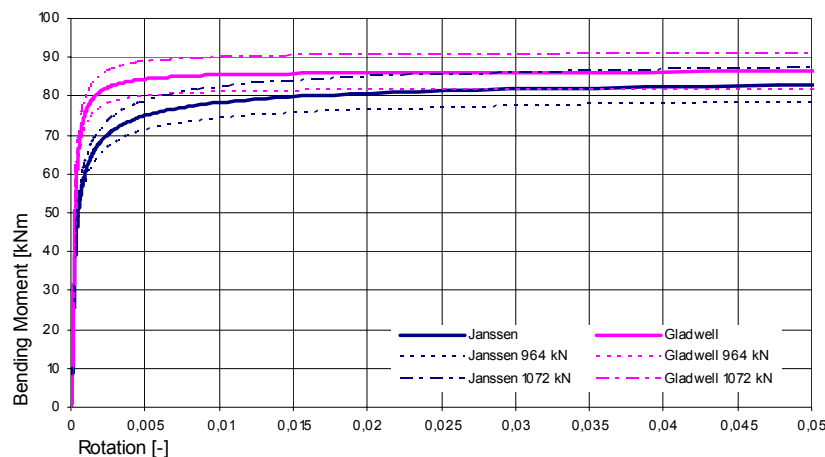


**Figure 2.13:** Janssen and Gladwell relation for different values of the normal force (joint height= $170 \text{ mm}$ )

## 2.4 Theoretical behaviour of ring joints

A ring joint is located in between segments of two adjoining rings. In this joint, rotations and translations can occur. Between the two concrete surfaces a packing material may be applied. When no packing material is applied a concrete-to-concrete contact is present. This can result in high peak stresses because of an unsmooth surface. The friction in this joint, established

by concrete-to-concrete contact, will develop a ‘shear’ force counteracting mutual radial and tangential deformations. Implicitly this also gives a resistance against rotations in this plane. The shear force depends on the smoothness of the concrete area, the normal force in the joint and the area which makes contact. When a packing material is applied, in between the two concrete surfaces, there will be two planes in which shear deformations between materials can occur. Friction between the concrete and the plywood will develop a ‘shear’ force between two rings counteraction mutual deformations. Depending on the packing material applied, a shear deformation inside the packing material can also occur.

## 2.5 Experimental research

Joints between segments are loaded by normal forces, shear forces and bending moments. The properties of the packing materials in between the segments will have a large influence on the global behaviour of a tunnel ring. Various experiments have been carried out to analyse the behaviour of these joints under different load conditions. These experiments could validate existing analytical and numerical models and are valuable for numerical modelling of a complete lining.

### 2.5.1 Segment joints

In Hordijk and Gijsbers (1996), experiments on segment joints without packing materials are described. Two tunnel segments were loaded by increasing bending moments, under various normal forces. The influence of bolts on the rotation capacity of joints is also studied. Because a bolt is positioned only on one side of the segment, experiments were performed on two rotational directions. This resulted in a total of four test specimens, one specimen for testing, one without a bolt, one with a bolt in positive bending and one with a bolt in negative bending. The used segments had a segmental thickness of  $350\text{ mm}$  and a segmental width of  $500\text{ mm}$  which is a third of the width used in the full-scale tunnel test. The contact height of the joint is  $158\text{ mm}$ , which results in a contact area of  $158 \times 500\text{ mm}^2$ . Elongations were measured in four points, two on every side of the segment, over a length of  $50\text{ mm}$ ,  $600\text{ mm}$  and  $1200\text{ mm}$ . A schematic overview of the test set-up is given in figure 2.14.

When raising the normal force to the desired level the measurements resulted in normal force-deformation diagrams. After reaching a constant deformation the rotation test could start. For the calculation of the rotations, the measurements directly over the joint,  $50\text{ mm}$  are used. The differences in measured rotations between  $50$ ,  $600$  and  $1200\text{ mm}$  were very small so the  $50\text{ mm}$  data is a good representation of real occurring rotations in the joint. The normal forces lay in a ranch varying between  $0,2\text{ kN/mm}$  and  $4,4\text{ kN/mm}$ . In the Botlek Railway Tunnel an average normal force of  $1,5\text{ kN/mm}$  is present [Vervuurt 2003] and in the full-scale test a normal force of  $0,7\text{ kN/mm}$  is present [Vervuurt and Den Uijl 2006]. These experiments are thus representative and obtained moment-rotation diagrams are treated below.

Looking at the moment-rotation diagrams a linear and a non-linear branch is recognized just like Janssen and Gladwell predicted. According to the theory the initial stiffness is independent from the normal force. In the experiments the initial stiffness seems to be dependent from the normal force. The initial rotation stiffness shows a steeper slope with increasing normal forces, figure 2.15. This can be explained by the fact that the concrete contact areas

are not smooth enough to guarantee ideal contact in the joint. With an increasing normal force the contact area increases. In the treated theoretical models a full contact is supposed. Because this is not feasible in practice, the initial stiffness will always be lower than the theoretically derived stiffness. For low normal forces the discrepancies between the experimental stiffnesses and theoretical stiffnesses are very large. In these areas the theoretically derived initial stiffness according to Janssen or Gladwell cannot be used. For a normal force in the range varying between  $2 \text{ kN/mm}$  and  $3 \text{ kN/mm}$  the Janssen relation shows a good approximation to the found initial stiffness in the test results.

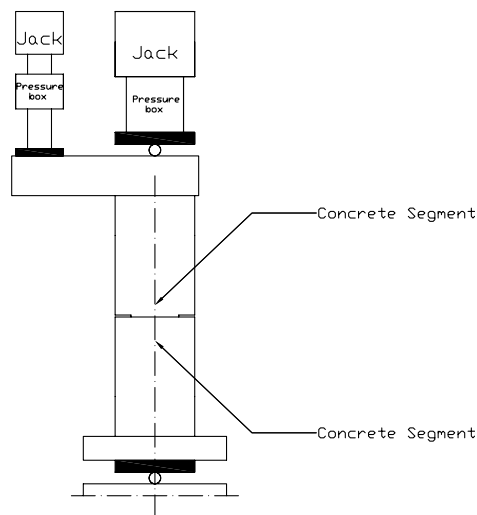


**Figure 2.14:** Schematic overview of test set-up

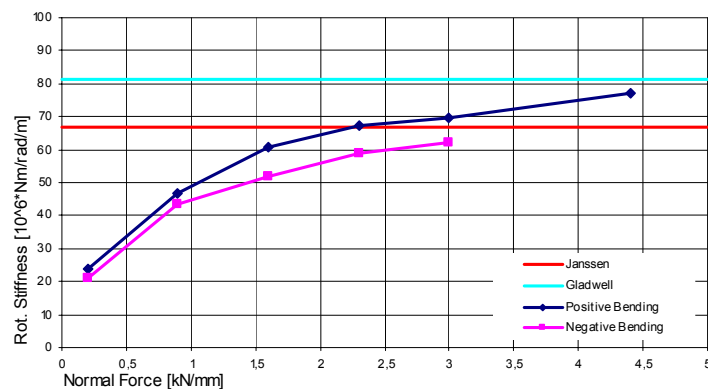


**Figure 2.15:** Initial rotational stiffness depending on the normal force [Hordijk and Gijsbers 1996]

Hordijk and Gijsbers (1996) concluded that for large rotations the results are in accordance with Janssen which means that Janssen may be used for modelling the joint behaviour. When having a closer look at the results, figure 2.16, Janssen shows a too weak behaviour, especially for rotations below  $0,002 \text{ rad}$  the moments are not described very well. Only for the highest normal force Janssen shows a good overall relation but it is questionable what the influences of discrepancies in rotational behaviour, for low normal forces, are in practice. The experi-

mental results are also compared to theoretical models derived from Gladwell in figure 2.16. Gladwell predicts larger bending moments than the test results show and the initial stiffness is for all normal forces too high. From these tests it seems that Janssen predicts rotational behaviour more accurate than Gladwell.

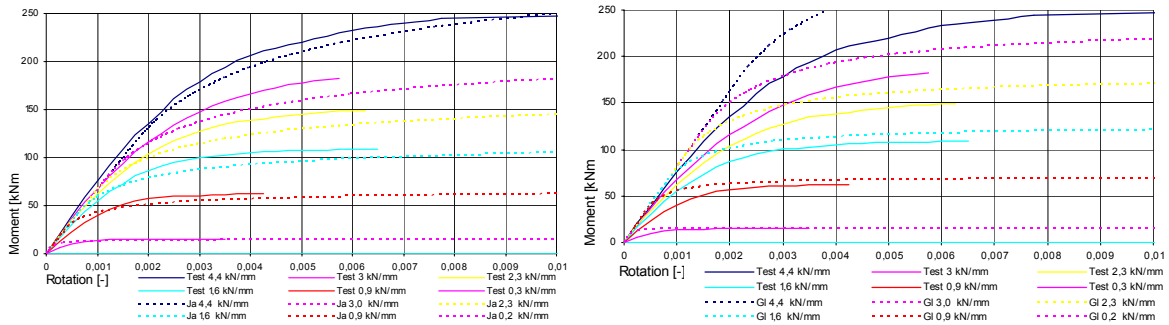


**Figure 2.16:** Test results [Hordijk and Gijbers 1996] compared to Janssen (left) and compared to Gladwell (right)

According to Hordijk and Gijbers (1996), the initial rotational stiffness was hardly affected by the presence of bolts. The ultimate bending moment of joints with a bolt is higher than joints without a bolt. This increase in maximum bending moment capacity is in the order of  $20 \text{ kNm/m}$  and decreases with an increasing normal force. From these tests it can be concluded that the influence of bolts is of minor importance on the rotations.

## 2.5.2 Ring joints

The ring joints exist of contact surfaces between the elements and of dowels and sockets, from which the latter one is not making contact. The shear behaviour of the contact surfaces is of major importance for the migration of bending moments to adjacent rings. When the bending moment capacity of a segment joint is reached, additional moments can be transferred to adjacent segments resulting in a higher load bearing capacity of the overall lining.

Experimental research on the shear stiffness between rings is described in Gijbers and Hordijk (1997). Both kaubit as well as plywood as a packing material is tested. Also the failure of the dowels is tested. The shear behaviour of the contact areas was only investigated in the radial direction.

The specimen on which the shear behaviour of the shear connection is tested consists out of 3 unreinforced concrete blocks with two joints on both sides of the middle block (obtained ‘shear’ forces therefore have to be divided by two). In this joint kaubit or plywood with a thickness of  $2 \text{ mm}$  and dimensions  $150 \times 150 \text{ mm}^2$ , is used as a packing material in between the concrete surfaces. The middle block is pushed out under a normal force and deformations are measured. The experiment was performed deformation controlled. Results of performed tests are described in the next paragraphs and a schematic overview of the test set-up is given in figure 2.17.

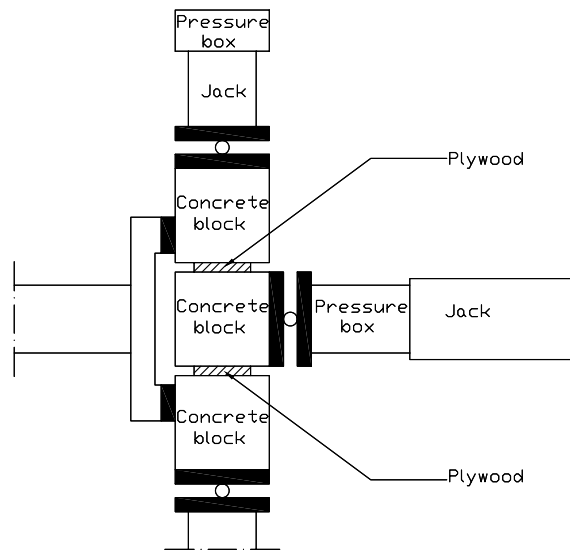


**Figure 2.17:** Schematic overview of test set-up

### Kaubit as a packing material

A normal force was applied and increased to a maximum of  $135\text{ kN}$ ,  $270\text{ kN}$  or  $405\text{ kN}$  in 30 minutes. This value was kept constant in the coming two hours and displacements were measured every 10 minutes. Subsequently the shear tests were performed. In the first 30 minutes the thickness of the kaubit decreased and was squeezed out of the joint. This continued during the next two hours until no ongoing deformation was measured and a remaining thickness of  $0,2 - 0,3\text{ mm}$  was left. After these 2,5 hours the shear test started. The applied normal force was of little influence on the maximum shear force which could be transferred. The speed in which the displacement is applied is of influence on the maximum shear force which can be transferred. These experiments resulted in different friction coefficients for different deformation velocities. The lower the deformation velocity is, the lower the friction coefficient. For very low velocities the friction coefficient is negligible. In figure 2.18 the results of a deformation controlled experiment with a deformation velocity of  $0,1\text{ mm/minute}$  and a normal force of  $270\text{ kN}$  is presented. From the graph it can be concluded that kaubit practically cannot transfer shear forces.

Caused by the decreasing thickness of the kaubit sheets, the underlying concrete surfaces are making contact. This means that in a joint these areas co-operate in transferring forces. How much the concrete will co-operate is dependent on how the contact between the concrete surfaces is established, how smooth the concrete surface is and on the magnitude of the applied normal force. For those areas in which the concrete makes contact, a friction coefficient of  $0,4$  to  $0,5$  can be applied and a much higher shear force can be transferred to the neighbouring segment.

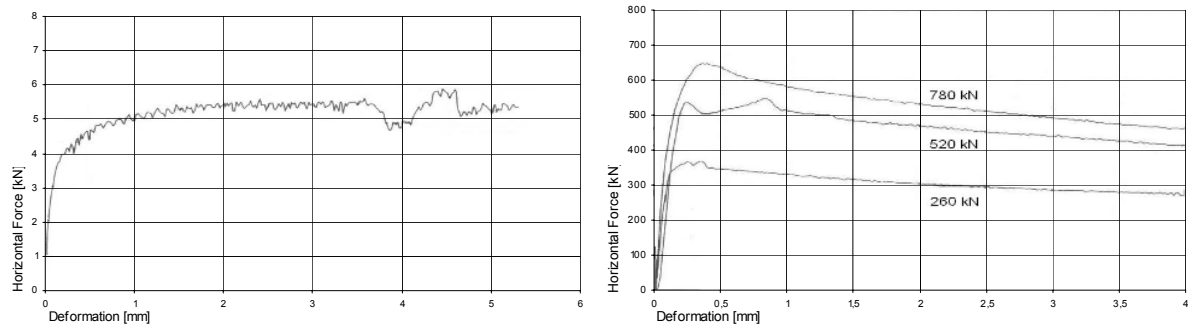


**Figure 2.18:** Force-deformation diagram for kaubit (left) and for plywood (right, with different values of the normal force) [Gijsbers and Hordijk 1997]

### Plywood as a packing material

A total of 3 specimens were tested in which plywood was used between the concrete cubes. A normal force was gradually increased to a maximum of 260 *kN*, 520 *kN* or 780 *kN* and kept constant during another thirty minutes. Every 10 minutes deformations were measured and after one hour a total axial deformation of 0,8 to 1,0 *mm* was measured in test 1, 2 and 3. After one hour the shear test started. The tests resulted in friction coefficients. These friction coefficients were dependent on the normal forces and the applied displacements. These tests are short term and no information is available on the behaviour of plywood in long term situations. Half of the thickness of the packing material will remain which implies that the concrete edges of the segments will not make contact as it did when using kaubit. Result is that normal- and shear forces are still introduced into the next segments concentrated. The concrete surfaces of the segments are not making contact so no peak stresses or damages occur.

Normal Force [kN]	Horizontal Shear Force		Friction Coefficient	
	Maximum	At 4 mm	Maximum	At 4 mm
260	362	275	0,70	0,53
520	531	418	0,51	0,40
780	644	462	0,41	0,30

**Table 2.1:** Results of ring joints loaded by shear forces [Gijsbers and Hordijk 1997]

The tests were deformation controlled using a constant deformation velocity of 0,1 *mm/minute*. The results of these tests are shown in figure 2.18. The three specimens were each loaded with different normal forces. The top values of the shear force were all reached before a deformation of 0,5 *mm* was applied. When gradually increasing the deformation beyond this top value, the shear force will decrease and eventually reach 75% of its top value. At that point a deformation of 4 *mm* is reached. Gijsbers and Hordijk (1997) concluded that shear in the joint takes place in one of the two contact surfaces. No notable shear deformation took place in the plywood itself. Friction coefficients were calculated at the top value of the shear force and at a deformation of 4 *mm*. The friction coefficient turns out to be dependent on the normal force and the applied deformation and lies in the ranch of 0,30 and 0,53 for a deformation of 4 *mm*. These values can be found in table 2.1. Friction coefficients found

during the experiment are comparable with friction coefficients found for smooth concrete surfaces shearing against each other without packing materials.

A deformation of approximately  $0,3 \text{ mm}$  results in the largest shear force. When gradually increasing the deformation, the shear force will decrease and eventually reach 75% of its top value. At that point a deformation of  $4 \text{ mm}$  is reached. This behaviour can be described by a bi-linear relation shown in figure 2.19. The initial stiffness is mostly given a value of  $10^6 \text{ N/mm}$  and the strength is determined with equation 2.5.  $F - shear$  is the horizontal branch in the bi-linear relation and is dependent on the normal force,  $F_n$ , present in the joint.

$$F_{Shear} = 4F_n^{1/3} \quad (2.5)$$

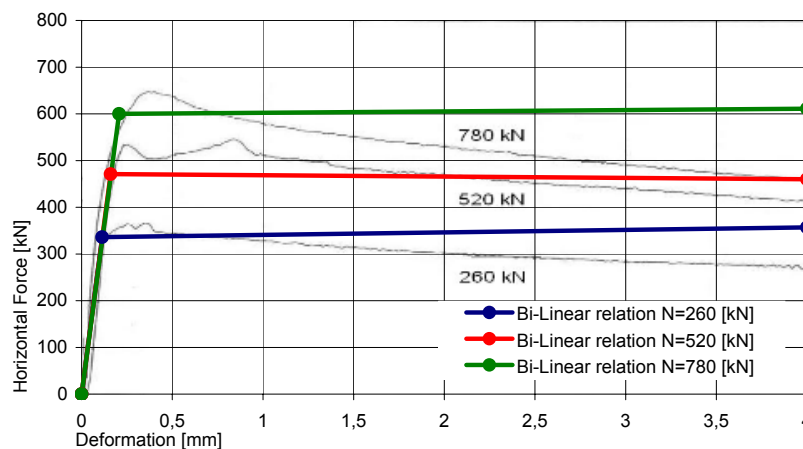


**Figure 2.19:** Experimentally obtained shear forces compared to bi-linear relations in which shear strength is determined by formula 2.5

### Dowels in ring joints

Dowels and sockets were also tested. These elements are not installed for transferring forces under normal load conditions. Only when deformations become large, and the plywood is not able to carry the shear force anymore, the dowels and sockets make contact and become active in transferring forces. One dowel laying in a socket is loaded by a deformation until failure occurred. After a deformation of  $5 \text{ mm}$  forces began to grow which is the moment that the dowel touches the outside of the recess in which the dowel is resting. At that moment the stiffness increases enormously until failure occurred. When the segments are not placed exactly in one line, the mutual deformations between the dowel and the socket before making contact may obviously deviate. The dowel had a circular shape with a diameter of  $70 \text{ mm}$ . This relatively small dowel measured a failure capacity of  $140 \text{ kN}$  at a deformation of  $2 \text{ mm}$ . The strength of the joint is determined by the strength of the recess in which the dowel is placed. No damage was found on the dowel after dismantling of the test specimen. The value at which failure occurs is heavily influenced by the tensile strength of the applied concrete [Gijsbers and Hordijk 1997].



## Chapter 3

# Ultimate Limit State analysis

Structural analyses and experiments performed in the past were mostly focused on the Serviceability Limit State. In this paragraph theoretical ideas about the behaviour and failure mechanisms of a lining in the Ultimate Limit State are described.

A tunnel can fail because of different mechanisms. In this section failure and failure mechanisms due to uniform radial and ovalisation radial loading, caused by soil, water or grout pressures, are discussed. In general the soil behind the lining or the lining itself can fail. Bakker (2000) describes the failure of a tunnel with regard to the soil behind the lining, whereas Blom (2002) discusses failure and corresponding failure mechanisms of the lining itself.

### 3.1 Failure mechanisms of lining due to ovalisation

When a horizontal ovalisation of the tunnel lining occurs, the soil at the left and right side of the tunnel is compressed. Due to this compression a lateral stress increase will be observed, which tends to diminish the difference between the vertical and horizontal soil stresses. A flexible lining in stiff soil will deform by the soil stresses in such a way that the lining stresses are mainly due to hoop compression. Bending moments in the lining would vanish and the only mode of failure left would be compressive failure of the lining [Bakker 2000]. Problem is that additional bending moments can be introduced due to large deformation effects. The increase of these second order bending moments due to geometric effects might exceed the decrease due to diminishing stress differences in the surrounding soil. Bakker (2000) investigated the second order bending moments and concluded that for small deformations of the lining bending moments would decrease and for larger deformations bending moments would increase. For Dutch soil conditions, and realistic lining parameters, Bakker (2000) concluded that bending moments decrease. This means that in case of horizontal ovalisation the ground has a positive influence on the ultimate load bearing capacity of the lining.

Blom (2002) also described the behaviour of a lining in the ground subject to ovalisation loads. When increasing the load, bending moments in the lining increase until somewhere in the lining the bending moment capacity of a segment or a cross-section is reached. The active load can still increase without an excessive increase in deformations of the lining. More plastic hinges will develop and deformations grow. Blom (2002), just like Bakker (2000), emphasizes

that the increasing loads are fully compensated by the soil and that the ring stays stable. The ULS will thus not be determined by the bending capacity but by the normal capacity of a segment.

### 3.2 Snap through of a joint

In the lining both normal forces and bending moments are present, which is comparable to an eccentrically loaded column. This means that local instability like buckling can occur. When the deformations become relatively large and the ring itself is not able to resist the normal force anymore, segments can snap through which means failure of the lining. Blom describes this snap through mechanism for a single ring partially supported by soil, figure 3.1. A geometrical and physical non-linear calculation is set up in which a segmented ring is loaded by an uniform radial load and an increasing ovalisation radial load. The lining is partially supported by springs at the sides of the ring. Increasing the ovalisation radial load results in increasing bending moments until a plastic hinge develops in the bottom of the lining. The ring stays stable when further increasing the load until two more plastic hinges develop at the same time at the top of the ring. In between those two plastic hinges there is a segment joint which will snap through. Blom calculated that the increase of the load from the first plastic hinge to the snap through is a factor three. This mechanism is calculated to happen when the top of the ring undergoes a displacement of 650 *mm*.

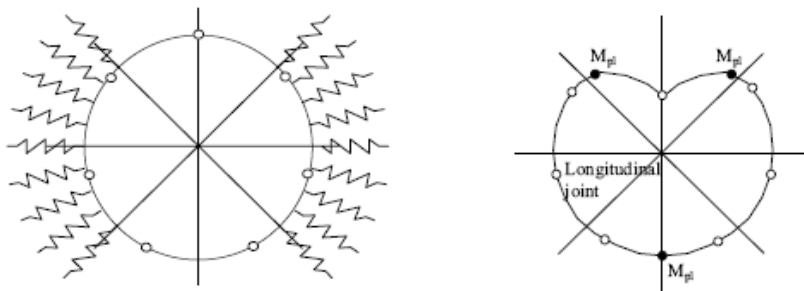


**Figure 3.1:** Model of lining loaded by ovalisation load (left) and failure mechanism (right)

In the full-scale tunnel set-up at Delft University of Technology the forces on the lining caused by the soil are simulated using hydraulic jacks. These jacks apply an uniform radial force and an ovalisation radial force on the tunnel lining. The ovalisation radial force increases load at the top and bottom of the lining and decreases load at both sides of the lining. As described above, the soil positively reacts on this force and supports the lining. In the test facility the influence of the ground is not present which leads to no resistance against the ovalisation radial load. This is Bloms case described above, in which the spring stiffness is set to zero. When no ground is present a different failure mechanism develops. Because segment joints have a low resistance against bending, plastic hinges can be expected here.

When the moment capacity of a segment or segment joint is reached an increase in rotations is observed in the single ring model, which results in large deformations. In reality, as well as in the full-scale test, the radial movement of the lining of a single ring interacts with adjoining

rings. Large deformations are limited by the migration of forces to adjoining rings.

When large deformations occur the water tightness of the lining is not ensured. Because of shear of adjoining rings the gaskets begin to open and water can flow to the inside of the tunnel. This water contains soil leading to a reduced support of the lining at that spot and may cause failure. These deformations are prescribed in the SLS but because of serious safety concerns it can be an ULS condition.

In building practice and in linear analysis the existence of one plastic hinge is considered to be the maximum capacity of the tunnel lining. When doing non-linear analysis the loading can still increase without collapse. Increasing the load even further results in more plastic hinges until instability of the lining occurs. Blom proved that a high plastic reserve is present in a lining.

### 3.3 Non-linearities

In Vollema (1996), the influences of geometrical non-linearities are analysed. This research concluded that the influence of geometrical non-linearities do not have to be taken into account. However, the load in this research was based on the SLS in which deformations are relatively small. When performing ULS analyses the influence of geometrical non-linearities have to be investigated. Because of high normal forces present in the concrete, a small deformation can cause significant bending moments. In Blom (2002), a comparison for a single ring between linear and non-linear behaviour, physical and geometrical, for joints and segments is performed. When the ring is fully embedded in the soil, modelled by springs, there will be no failure. Only the rate of increase in deformations in the various analysis is different, figure 3.2(right). Increasing ovalisation loads is compensated by soil reactions just like described in the previous paragraph. Failure is not initialized by reaching the ultimate bending capacity but by reaching the normal capacity.

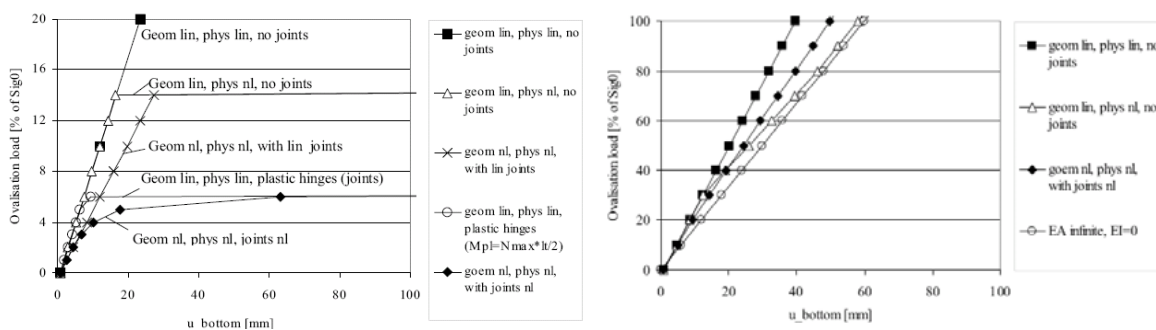


**Figure 3.2:** Ovalisation load plotted as a function of the radial deformation for lining without soil (left) and lining with soil (right), deformation curves plotted for different conditions of the segments and joints (Linear or Non-Linear)

In the ULS, failure is defined as the situation where deformations increase to infinity so a large influence of non-linear behaviour is expected. A tunnel deforming is resisted by surrounding soil. In the full-scale test facility no soil, which can have a positive influence on deformations,

is present. This means a large influence of non-linearities. Blom made a comparison between different material analyses for a lining without the support of soil, figure 3.2 (left). Neglecting the non-linear behaviour of the segment joints overestimates the capacity of the ring with more than a factor two. If a geometrical and physical linear calculation is made, but the plastic moment of the segment joints is involved, the maximum loading found is equal to the full non-linear analysis. Including only non-linear joint stiffnesses gives a good approximation of the ultimate load capacity. The discrepancies between predicted and ‘real’ occurring deformations increase when the load approximates the ultimate load bearing capacity of the lining.

**Part II**

**Analysis of Test Data**



## Chapter 4

# Description of tests and test set-up

The full-scale test set-up consists of segments from the Botlek Railway Tunnel and was situated at the Stevin II Laboratory of the Delft University of Technology. A detailed description of the set-up is found in Blom and Oosterhout (2000). The set-up contains three rings, with a width of  $1.500\text{ mm}$ , which are situated in a vertical position, omitting the effect of gravity. Each ring is built up out of 7 segments and a keystone with a system radius of  $4.525\text{ mm}$  and a segmental thickness of  $400\text{ mm}$ . Joints between the segments are placed in a stretched bond alignment resulting in segment joints on the same circumferential location in the top and bottom ring. The three key-stones are situated differently in each ring. In the ring joints plywood sheets are used as a packing material. In the segment joints no packing material is used resulting in a concrete-to-concrete surface contact.

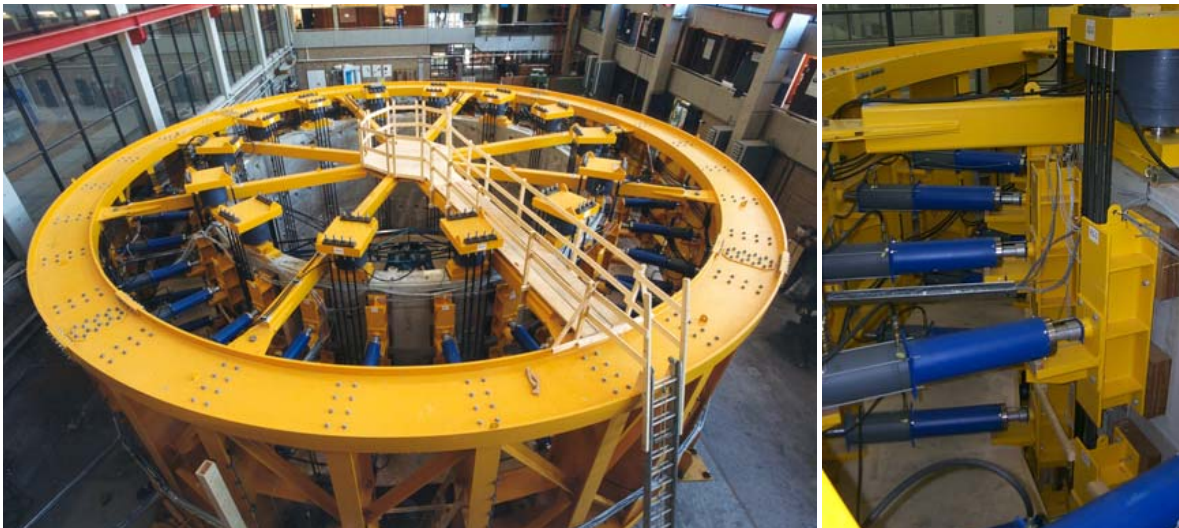


**Figure 4.1:** Top view of test set-up in the Stevin Laboratory of the Delft University of Technology (left) and close-up of radial and axial jacks (right)

The test specimen is loaded in a radial and axial direction. Per ring, 28 radial jacks are present. Each jack applies the force via a steel profile and two Azob blocks onto the concrete, as seen in figure 4.1. The reaction forces from the  $3 \times 28$  radial jacks are carried by a steel

frame outside the concrete lining. Axial pressure is provided by 14 jacks situated on top of the segments in the upper ring. Via Dywidag bars the reaction forces from the axial jacks are coupled to steel plates on which the segments in the bottom ring rest. These 14 steel plates allow for radial and tangential movements. Four of those plates only allow for radial translation and counteract tangential translations by hydraulic jacks. This way a rigid body rotation is prevented. A schematic overview of the lining including the surrounding structure, numbering of the jacks and external measurement equipment is given in figure 4.3.

## 4.1 Load on the lining

The ultimate ovalisation load capacity of the lining is determined for two different values of the axial force. A high axial force results probably in a strong interaction between the three rings leading to concrete failure. A low axial force results in a weak interaction between the three rings, probably resulting in failure due to slip of the ring joints and an ongoing rotation of the segment joints.

The specimen is loaded by axial and radial forces, of which the radial forces are subdivided in a uniform and an ovalisation part. In figure 4.2 the different load steps on the lining are represented graphically for both experiments. The experiment is force controlled. In practice the axial forces are determined by the driving force of the TBM. The uniform part of the radial force is mainly determined by the depth at which the tunnel is located, whereas the ovalisation part of the radial load is determined by the kind of soil in which the tunnel is situated. The effects of ovalisation loads are studied for two different values of the axial force.

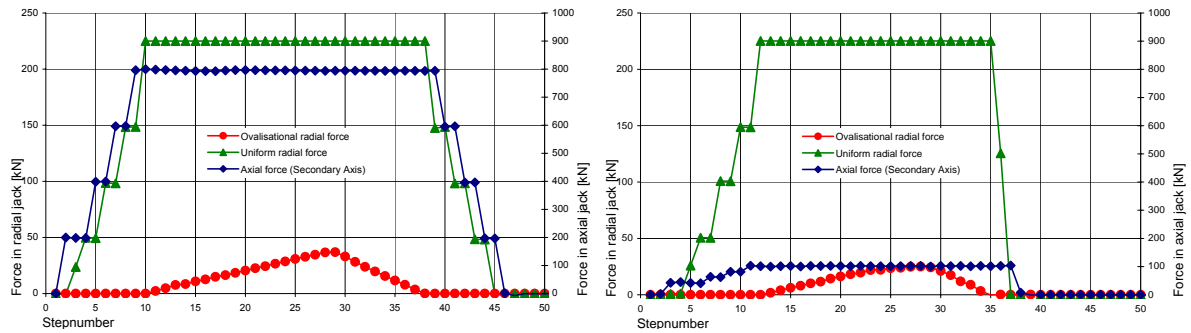


**Figure 4.2:** Overview of load on lining during experiment C01 (left) and experiment C02 (right) as a function of the step number, calculated from oil pressures in jacks

In the tests, first a uniform radial and axial load is applied in steps. After approximate 10 steps a uniform radial load of 225 kN per jack is present. This results in a normal force of 1002 kN/ring in tangential direction. A force of 225 kN/Jack corresponds to half of the average uniform radial force which is acting on the Botlek Railway Tunnel and corresponds to a shallow position of the lining.

The axial force applied varies in the two experiments. In the first experiment a relatively high force of 800 kN per jack is applied, producing a strong interaction between the three rings. This force is equivalent to half the average force at the Botlek Railway Tunnel. In the second

experiment the axial jacks deliver 100 kN onto the segments, representing an equivalent force of one sixteenth of the average force present at the Botlek Railway Tunnel.

After applying the uniform radial and axial load, these loads are kept constant. In the following steps an ovalisation load is put onto the lining. The ovalisation load is applied by locally increasing or decreasing the radial jack forces resulting in a sinusoidal ( $\cos 2\theta$ ) shape along the circumference of the lining. The maximum values are located between axial jacks 8/9 and 22/23. Minimum values are reached between axial jacks 1/2 and 15/16, see figure 4.3 for numbering. With each step the load is raised, until failure occurs. The failure can be the excessive cracking of concrete or the snapping through of a joint between two segments. In the first experiment the maximum load is reached at an ovalisation load equivalent to about 15% of the applied uniform radial load. In the second experiment this relative ovalisation load is about 10%.

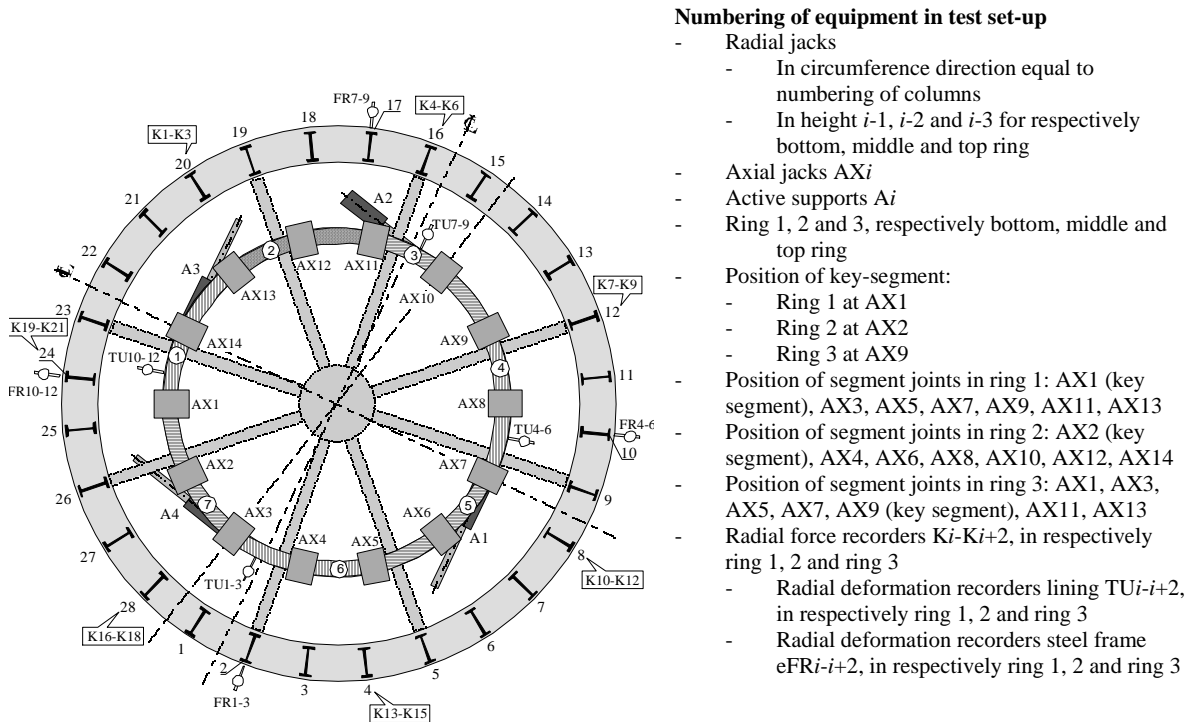


**Figure 4.3:** Schematic overview of test specimen and surrounding steel frame, including jack numbering and numbering of external measurement equipment

## 4.2 Conducted measurements

During the experiments a lot of data is collected. The results of the measurements are used to verify calculations and to validate numerical simulations. The load is determined and controlled by measuring oil pressures in the jacks and by deriving forces from installed pressure boxes. After a force step is applied, data from all the measurement equipment is stored. To obtain a visual representation of the location of measurement equipment and

their belonging numbers, a schematic overview of the measurement equipment numbers is given in Appendix A.

For analysing the behaviour of segments and joints, measurement equipment is placed on the concrete lining as can be seen in figure 4.4. Every concrete segment is equipped with strain gauges on three different places on both sides of the concrete. They are placed in a vertical and horizontal direction to determine axial and radial strains. The top ring is also equipped with diagonal gauges to be able to calculate principal stress/strain directions. From the data the curvature in the segments can be determined. Based on the curvatures the bending moment can be determined. For uncracked cross-sections this can be calculated by using a bending stiffness belonging to a certain normal force. If a segment is cracked it is more difficult to determine the actual bending moment. Perhaps a decisive answer can be found using numerical simulations of a single reinforced concrete segment. Still it is questionable whether the collected strain data gives a good representation of the real curvature. Nevertheless, comparing two experiments or comparing curvatures of different segments this data can be used very well.

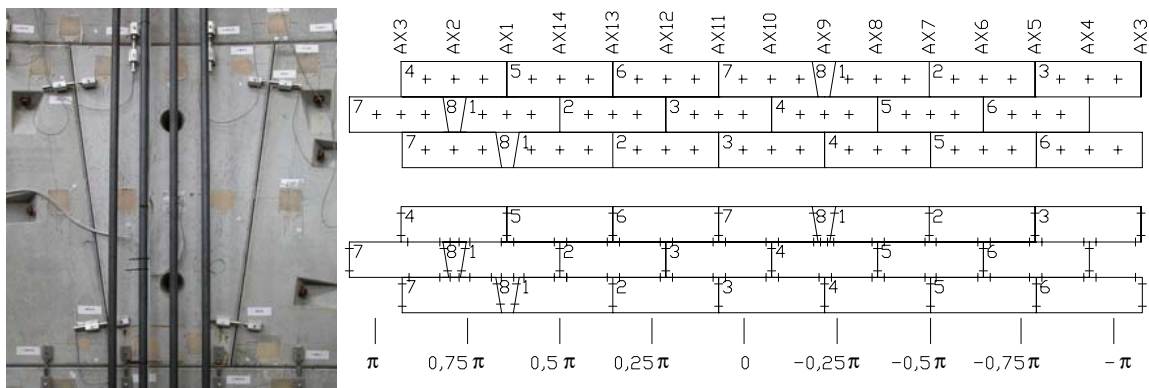


**Figure 4.4:** Measurement equipment placed around key segment (left) and schematic overview of positioning of measurement equipment on the concrete segments of the lining (right), strain gauges (right top) and LVDT's (right bottom)

Over a joint, LVDT devices are placed to be able to determine mutual rotations between the segments. Each segment joint is equipped with two LVDT devices on both sides of the segment. By dividing the measured differences in elongation of two LVDT's on each side of the joint by the segment thickness, the rotation in the joint is obtained. The two ring joints are also equipped with LVDT devices. Along the circumference a total of 32 devices on both sides of the lining are placed. This data can give information on the compression of the plywood and axial rotations. In the most critical segment joints the deformations are recorded continuously to be able to recognise the starting of failure and lower load before an 'explosive' collapse takes place heavily damaging the segments. This offers the possibility to analyse the segments afterwards, especially the dowels, and to be able to perform other tests.

Inside the concrete lining a laser device is situated to measure deformations. This rotating device measured the radial deformations on 6 different levels of the tunnel as a function of the

circumferential angle. Every rotation ended up with approximately 100.000 measurements with an accuracy of 0,1 *mm*. Because of its configuration no rigid body translations and rotations can be observed and the radial deformations of the lining are not known per point but as a function of the circumferential angle. Due to tangential translations of the lining the exact deformation behaviour can not be easily analysed by using this data. On the other hand, looking at this data, a good image of the global lining deformation can be obtained. In Vervuurt and Den Uijl (2006) curvatures for one segment are determined from the strain and laser measurements. The results are compared showing discrepancies. The data from the laser device gives higher curvatures compared to the curvatures determined by the strain devices. This might be explained by the fact that strain gauges on the tensile side of the concrete do not give reliable output, caused by cracking of the concrete. For the non-linear stage these discrepancies are significant but are smaller in the linear stage. Compared to analytical ring moments the laser data shows a good agreement.

On four locations, outside of the concrete lining, where maximum radial deformations are expected, radial deformation measurements take place. In figure 4.3 this equipment is indicated with TU1-TU12. This data gives a good representation of ovalisation deformations.

### 4.3 Earlier performed tests

The full-scale test facility was used from 1999 to august of 2005. In table 4.1 a chronologic overview of performed tests is given. The first series of tests involved the so called load at once tests, in which all three rings were equally loaded by uniform and ovalisation radial loading. Only SLS loads were put onto the lining and the results were useful to verify analytical models. In Blom (2002) a comparison between radial deformations of the lining and a developed analytical solution is performed for coupled segmented rings and a very good agreement is found. Comparing the strains on the concrete elements, corrected for axial forces and lateral contraction, with the analytical solutions and the 3D FE model, also showed a good comparison.

Being able to predict the forces and stresses in the lining very well under SLS loading, the tests continued with the sequential loading test. In these tests the bottom and middle ring were loaded simultaneously by uniform and ovalisation loads causing these two rings to deform. Since an axial pressure is present the non-loaded top ring also deforms due to the ring interaction. After this taken place the top ring is loaded by uniform and ovalisation loads. Finally, the top ring is deformed by ‘additional’ and ‘direct’ deformations. This test simulated the moment the new assembled ring is pushed out of the protecting steel shield of the TBM. During this process the lining is gradually loaded by the surrounding soil leading to unequal deformations of the lining in axial direction. From the experiments Blom concluded that when the top ring is loaded, 40% of the loading is remaining in the top ring, and 60% is migrating to the middle and bottom ring. Of this 60% a part of 40% remains in the middle ring, whereas 20% migrates to the bottom ring. Again, a good agreement between measured values and the analytical solution, frame analysis and 3D FEM analysis was found.

Basic load cases were tested again and described in Vervuurt (2003). These tests were performed in the SLS and compared to numerical models using shell elements and implementing

normal force dependent, non-linear rotational springs. A good agreement was observed between the FE model and the experiment. Discrepancies found between the FE model and the experiment were in the order of 10%.

Shortly after completing previous tests, the effect of the inaccurate placement of segments was studied. In these tests, one segment was inaccurately placed with a gap of 2 mm or 4 mm. In both cases cracking of the segment was observed. As can be expected, the cracks in the 4 mm case were more severe. Concluded was that the maximum allowable gap between two segments is 2 mm in order to prevent unacceptable cracking.

		1999	2000	2001	2002	2003	2004	2005
Load at once test (Blom 2002)	SLS	xxx						
Sequential loading (Blom 2002)	Constr.		xxx					
Basic load cases (Blom 2002)	SLS			xxx	xxx			
Inaccurate placed segments (Vervuurt 2003)	SLS				xxx	xxx		
Ultimate load capacity (Vervuurt and Den Uijl 2006)	ULS							xxx

**Table 4.1:** Chronologic overview of earlier performed tests

## Chapter 5

# Experimental results

The analysis of the experimental results is an important issue. A careful look at the data can give a lot of insight in the behaviour of the lining. During loading different stages can be distinguished. These parts are elucidated separately below, starting with an analysis of the global lining behaviour.

Most critical cross-sections along the circumference of the lining are cross-sections in which bending moments are maximal, caused by the ovalisational loading, or cross-section in which one or two joints are located. In the four points in which bending moments are maximal, the segments and joints are aligned differently resulting in less or more critical cross-sections. On the other hand, cross-sections in which lower bending moments are present can also be critical caused by the presence of joints.

Two of the four cross-sections on the lining possessing maximum bending moments are fitted out with one or two joints. These two cross-section are located at  $-0,5\pi$  and  $+0,5\pi$ , see figure 5.1. The cross-section at  $-0,5\pi$  is fitted out with segment joints in two out of a total of three rings whereas the cross-section at  $+0,5\pi$  is fitted out with one segment joint. The cross-section containing two joints is most critical and reaches its bending moment capacity first. The other two points on the lining possessing a maximum bending moment, are located at  $0\pi$  and  $-1\pi$  and do not include a joint at that particular cross-section. The segment joints are located just besides the line possessing a maximum bending moment. On one side a cross-section containing one joint and on the other side a cross-section containing two segment joints is present. Obviously the cross-section containing two segment joints is most critical and is shown in figure 5.2. Recapitulating, there are three cross-sections (at  $-0,5\pi$ ,  $0,07\pi$  and  $0,93\pi$ ) containing two segment joints and are loaded with high bending moments. If plastic hinges develop somewhere in the lining it is expected that they will start in these cross-sections.

### 5.1 Ovalisation deformation of lining

To get an accurate understanding of the behaviour of the lining, it is important to know how the lining deforms during the two experiments. For this purpose the laser measurements can be used very well. Disadvantage is that it cannot be derived what portion of deformations is caused by joint rotations and what portion is caused by curvatures in the segments. To be able to say something about these portions, the deformations of the lining can be calculated

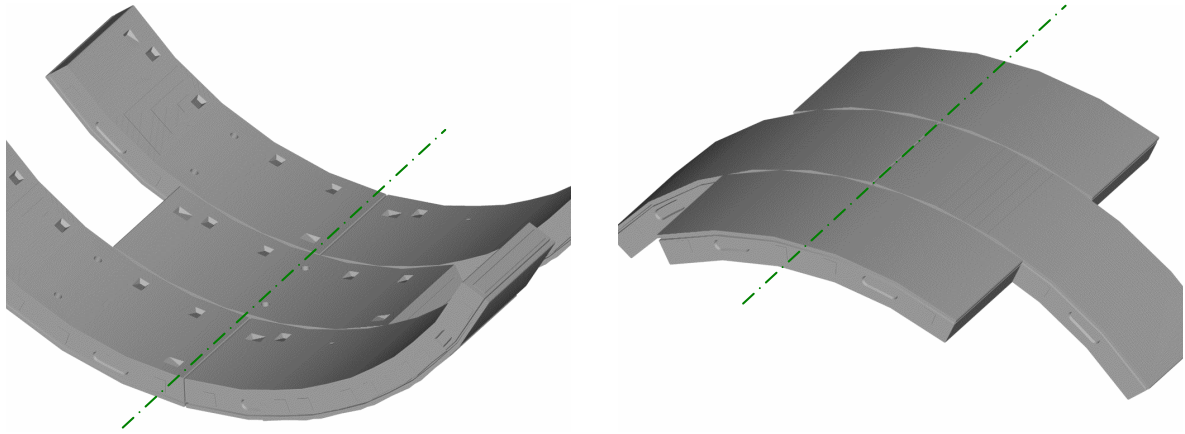


**Figure 5.1:** Critical cross-sections in tunnel lining, one segment and two joints at circumferential position  $-0,5\pi$  (left), two segments and one joint at circumferential position  $+0,5\pi$  (right)

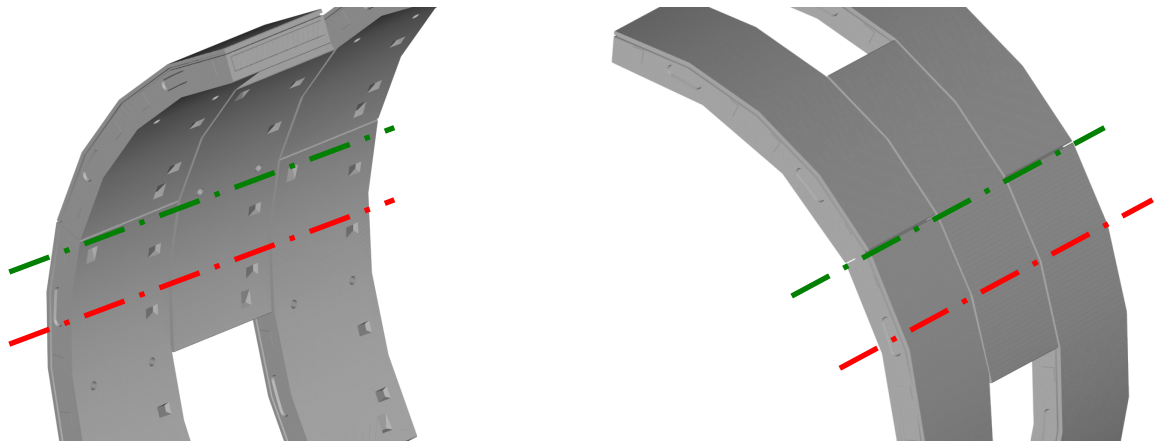


**Figure 5.2:** Critical cross-sections in tunnel lining shown by green line, one segment and two joints at circumferential position  $0,93\pi$  (left) and at  $0,07\pi$  (right), red line is cross-section with maximum bending moment

based on joint- and segment measurements performed during the experiments.

It is assumed that most deformations are caused by rotations located in the segment joints. To calculate the deformed shape of the lining, based on joint rotations, the segments are represented by straight lines between the joints. When no load is put onto the lining the angle between the lines connected with a joint is given in equation 5.1. The angle between two lines of which one line represents a key segment will be somewhat lower.

$$\phi_{j;initial} = \frac{360}{7} = 51,4deg \quad (5.1)$$

From the recorded deformations, on both sides of a joint, a rotation in a joint is calculated, equation 5.2. The values  $\Delta l_{outside}$  and  $\Delta l_{inside}$  are the recorded displacements with LVDT's on both sides of a segment. Add up this rotation to the rotation found in equation 5.1 and the angle between two segments is known. When multiplied by an enlargement factor  $m$ , small deformations can be made visible, equation 5.3.

$$\phi_{j;measured} = \frac{\Delta l_{outside} - \Delta l_{inside}}{d} \quad (5.2)$$

$$\phi_j = \phi_{j;initial} + m\phi_{j;measured} \quad (5.3)$$

The rotations of the eight joints in a single ring can now be calculated. In theory, the summation of the eight measured rotations,  $\sum_{j=1}^{n=8} \phi_{j;measured}$ , should be zero, but in practice deviations caused by inaccurate measurements occur. To represent the deformed shape of the lining more accurate a correction factor is included in the joint rotation which spread out the error. The corrected measured joint rotation is given in equation 5.4 and the new definition of the complete joint rotation is given in equation 5.5.

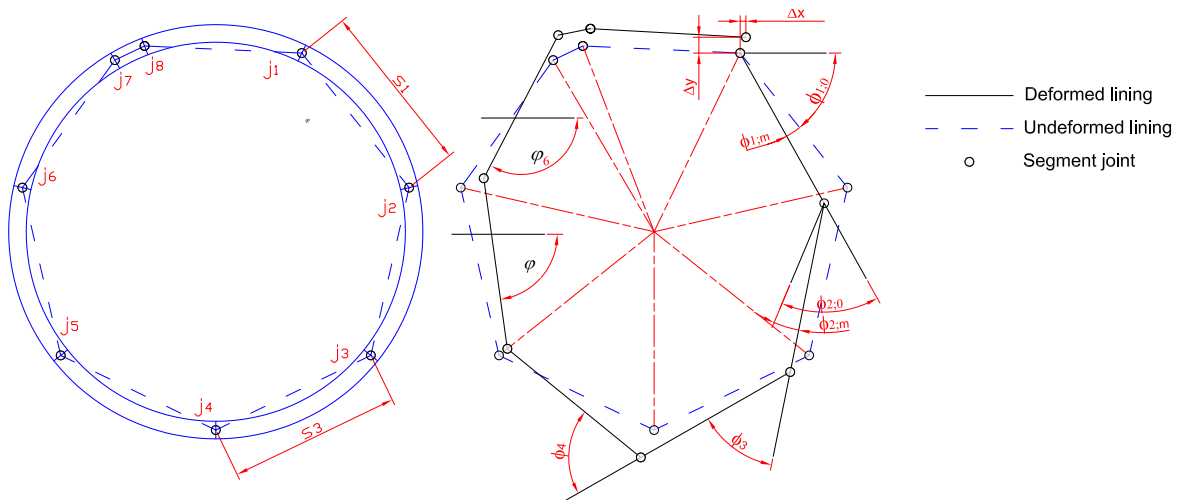


**Figure 5.3:** Clarification of calculation to determine deformed shape of lining based on joint rotations

$$\phi_{j;measured;cor} = \phi_{j;measured} \left( 1 - \frac{\sum_{j=1}^{n=8} \phi_{j;measured}}{\sum_{j=1}^{n=8} |\phi_{j;measured}|} \right) \quad (5.4)$$

$$\phi_{j;cor} = \phi_{j;initial} + m\phi_{j;measured;cor} \quad (5.5)$$

When the distance between the joints is known, a line can be plotted representing the deformed lining, based on the eight calculated joint rotations. The straight distance between two joints is calculated from equation 5.6. When calculating the distance between two points, from which one or two points are a joint between a counter segment and a key segment, another formula has to be used. For clarification of symbols see figure 5.3.

$$l_s = 2 * 4525 * \sin \left( \frac{360}{14} \right) \quad (5.6)$$

When drawing the deformed shape of the line one has to start with segment one. To be able to determine the position of the next joint, the position and angle of the first segment has to be calculated from equation 5.7 .

$$\varphi_s = \frac{X_{j+1} - X_j}{Y_{j+1} - Y_j} \quad (5.7)$$

Based on the distance between two neighbouring joints, the initial angle of a segment and a joint rotation the X- and Y-coordinate of the next joint is calculated with equations 5.8 and 5.9.

$$X_j = X_{j-1} + \sin(\varphi_s + \phi_{j-1;cor}) * l_s \quad (5.8)$$

$$Y_j = Y_{j-1} + \cos(\varphi_s + \phi_{j-1;cor}) * l_s \quad (5.9)$$

With equation 5.8 and 5.9 the coordinates of every joint are calculated. Because of the inaccuracy of the data the lining might not form a closed line. To overcome these discrepancies, the coordinates are corrected once again. The gap at the end of the line is divided in an X-distance and a Y-distance and equally spread over the eight joints resulting in a closed line.

$$X_{j;cor} = X_{j-1} + [\sin(\varphi_s + \phi_{j-1;cor}) * l_s] + \frac{\Delta X_{gap}}{8} \quad (5.10)$$

$$Y_{j;cor} = Y_{j-1} + [\cos(\varphi_s + \phi_{j-1;cor}) * l_s] + \frac{\Delta Y_{gap}}{8} \quad (5.11)$$

Based on the new coordinates the deformations of the lining can be plotted. When the curvatures in the segments are also incorporated a more accurate plot of the deformed lining can be calculated. These calculations are based on the same principals as the derivation previously shown, only now the coordinates of more points are calculated. These additional points are the locations where in the experiments strain gauges are situated. Based on strains on both sides of the concrete segments curvatures are calculated. Multiplying these curvatures with an influence length, figure 5.4, the rotation in a point is determined. From these rotations the coordinates of points along the circumference of the lining can be plotted. The influence length of the curvatures in a segment are shown in figure 5.4. Having calculated joint and segment rotations a correcting is carried out just as explained in equations 5.4, 5.10 and 5.11,

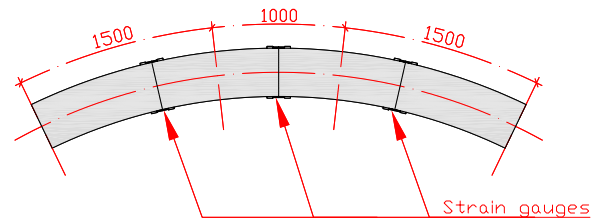


**Figure 5.4:** Influence length of curvatures in a segment

only now 30 points are involved.

The deformations are plotted starting from joint number one. The plotted line will also return to this point and the deformed shape of the lining is observed. Problem is that the deformed shape has to be repositioned in the correct position. Because little information about the position of the shape can be derived from measurements, the shape is centered to the middle of the undeformed lining and rotated in such a way that deformations of two joints are on a horizontal line. This principle is graphically shown in figure 5.5. It has to be emphasized that this rotation is not based on measurements. The figures only represent the shape of the deformations.

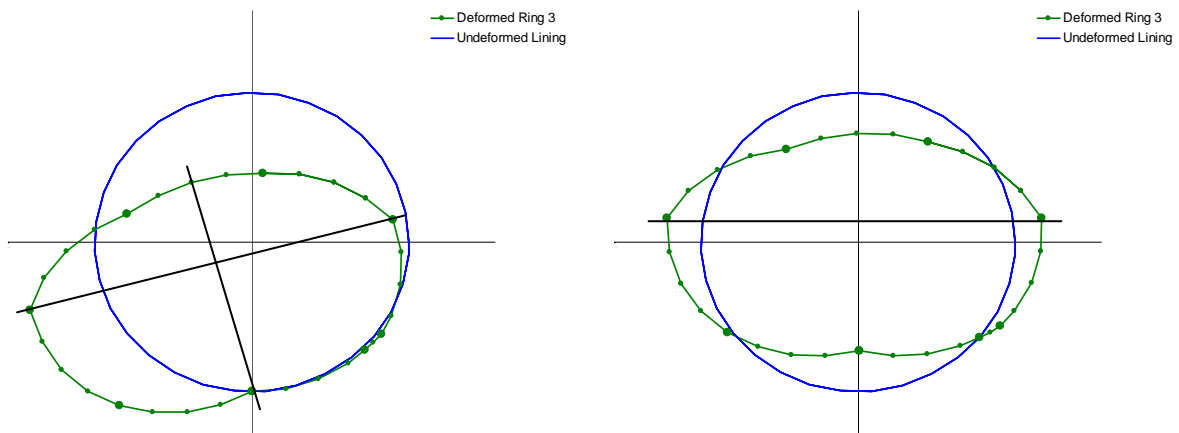


**Figure 5.5:** Positioning of deformed shape shown for ring 3, not rotated (left) and rotated (right)

From the performed calculations the deformed shape of the lining can be made visible. Moreover the deformations caused by joint rotations and deformations caused by segment curvatures can be analysed separately. This will increase understanding in lining behaviour and is more valuable compared to laser measurements. In Appendix B a spreadsheet is included from which the calculation of deformations of ring 1 for a particular load step is clarified.

## 5.2 Global observed lining behaviour

The geometry of each of the three rings is symmetrical with respect to the y-axis when the keystone is not considered. Deformations and strains are also found to be symmetrical with respect to this axis. In figure 5.6 the maximum deformations of the lining are drawn for experiment C01 and C02. These deformations are based on the measured rotations in the joints and the measured strains on the surfaces of the segments. As can be seen from these figures, it is clear how the load acted on the lining. Deformed states of lining in other load steps can be found in appendix C for experiment C01 and in appendix D for experiment C02.

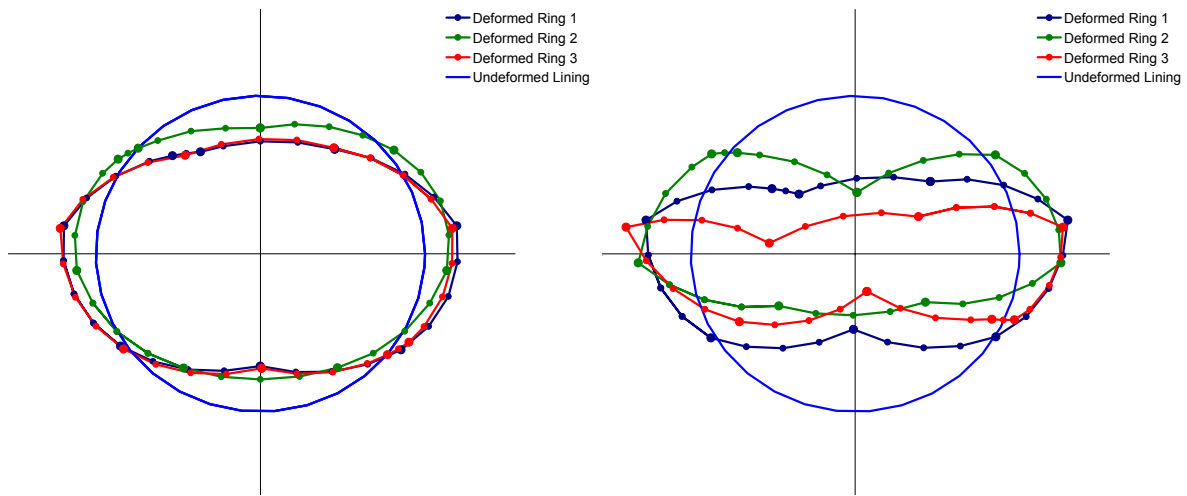


**Figure 5.6:** Deformed shape of lining, step 30, enlargement factor 50, experiment C01 (left) and experiment C02 (right)

In the left figure (figure 5.6) the maximum deformations of the first experiment are shown. It can be concluded that less deformations occur in experiment C01 compared to C02. This is a result of the stronger interaction between the three rings caused by the high axial pressure. Also a reduced stiffness of some segments, as a result of previously developed cracks in C01, has consequences for the deformations in experiment C02.

From the picture shown above it is seen that deformations of the top and bottom ring are larger compared to the middle ring. During the full-scale experiment this is not noticed and later on in this chapter the reason for these apparent deviations in deformations is explained. The rings which have joints placed on the same circumferential location, ring 1 and ring 3, deform almost exactly the same in C01. In the second experiment this conclusion is incorrect although ring 1 and 3 still deform more compared to ring 2. An explanation for the smaller deformations of ring 1 is the fact that four of the 8 joints in this ring encounter more resistance due to the fact that the active tangential supports are attached to the lining at these joints.

The behaviour of the lining can be represented by showing the maximum deformation of the lining plotted versus the applied ovalisation load. In figure 5.7 (C01) and figure 5.8 (C02) the average deformation of four points on the lining, which possess maximum deformation, are shown. This ovalisation is based on measurement devices placed on four points outside

of the lining and only measures radial deformations. In figure 4.3 this equipment is indicated with TU1 to TU12. This equipment reached its limiting measuring distance at the end of the second experiment resulting in unreliable values in this branch. For this branch the deformations are based on data collected from the laser measurements.

In experiment C01 a non-linear branch in deformations is reached after an ovalisation load of  $25 \text{ kN/Jack}$ . At  $36 \text{ kN/Jack}$  a horizontal plateau is reached, indicating failure. For the second experiment non-linear effects are noticed at  $15 \text{ kN/Jack}$  and a plateau is reached at  $24 \text{ kN/Jack}$ .

Deformations are caused by joint rotations and segment curvatures. In the figures 5.7 and 5.8 the ovalisation deformations only caused by joint rotations, based on calculations described in chapter 5.1, are given. In the linear branch of experiment C01, 43% of total ovalisation deformations are caused by joint rotations increasing to 55% when maximum load is reached. The part of deformations that is caused by joint rotations, increases even further to 58% when the load is reduced to zero again.

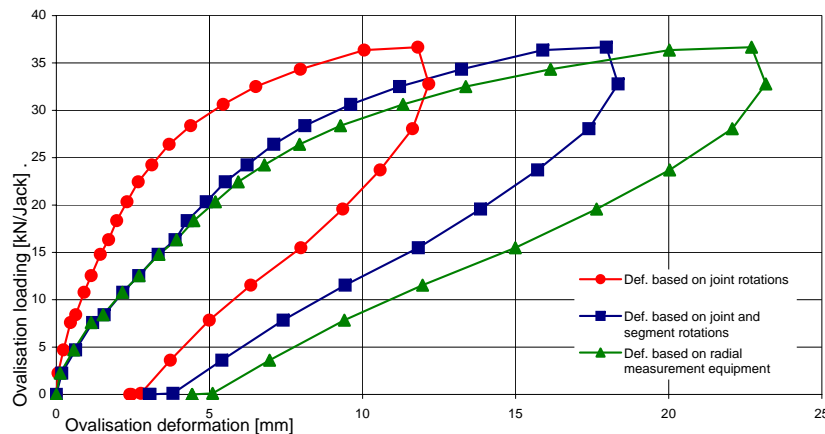


**Figure 5.7:** Average total ovalisational deformation of three rings plotted and subdivided into deformation only caused by joint rotations and caused by joint rotations and segment curvatures, experiment C01

In the first stage of the second experiment the part of deformations caused by joint rotations is exactly the same compared to the first experiment. When increasing the load, the ovalisation by joints starts to increase more compared to C01 at  $15 \text{ kN/Jack}$ . At failure, the joint rotations dominate deformations by about 90%. This percentage is measured after slip of the ring joints has taken place.

The rotations in the joints are responsible for deformations in the lining. Approaching deformations more accurate the curvatures in the segments have to be incorporated. Based on calculations described in chapter 5.1 an ovalisation deformation based on joint rotations and segment curvatures is plotted in figure 5.7 for experiment C01 and 5.8 for experiment C02. This should result in an improved approach of measured deformations. In fact, it should be the deformation which is measured with the radial equipment outside the lining (TU1-TU12),

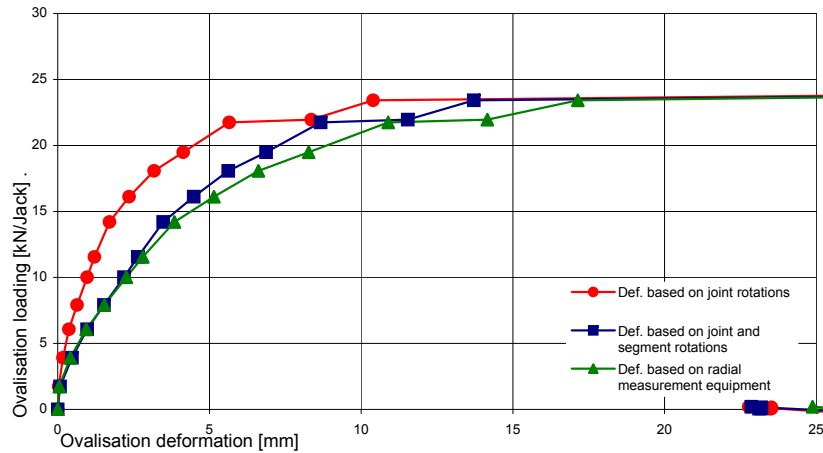


**Figure 5.8:** Average total ovalisational deformation of three rings plotted and subdivided into deformation only caused by joint rotations and caused by joint rotations and segment curvatures, experiment C02)

but this is clearly not the case. Although the ovalisation deformation based on joint rotations and segment curvature approaches the measurements (TU1-TU12) more accurately, in the non-linear branch discrepancies are recognised. This is expected to be the result of cracking of the segments. When a crack originates near a strain gauge the measured strain drops although deformations grow located in the crack. This is the reason why a complete ovalisation deformation can not be calculated based on joint and segment measurements. Nevertheless, including segment curvatures a very good image of the deformations is formed.

In the second experiment a severe increase in deformations takes place between  $20 \text{ kN/Jack}$  and  $25 \text{ kN/Jack}$ . The joint rotations increase in this branch whereas the strains do not increase proportional to the joint rotations. From figure 5.8 it can be concluded that an ongoing rotation of the joints is almost completely responsible for the increase in deformations.

In the first experiment, compared to the second experiment, joint rotations are less responsible for overall deformations. The deformations based on strain measurements are larger but not increasing very rapidly, caused by the fact that cracking occurs which cannot be measured but was observed during the experiment.

### 5.2.1 Experiment C01

In the previous analyses the deformations are calculated as the averages of the three rings. In this section the behaviour of the separate rings for experiment C01 is studied. In figure 5.9 the deformations of the lining, caused by joint rotations and measured with TU1-TU12, are outlined per separate ring. As previously mentioned the deformations of ring 2, based on joint and segment measurements, seem to be smaller compared to ring 1 and ring 3. This is not noticeable out of results from measurements outside the lining. These measurements say that all three rings deform more or less the same. It is expected that cracks are responsible for this discrepancy as is explained in the following paragraphs.

In figure 5.9, total ovalisation deformations and deformations based on joint rotations, are presented per separate ring. What is interesting to see in this picture is the portion of joint rotations which is responsible for the overall deformations. The joint rotations in ring 1 and ring 3 possess 45-70% of total deformations. Especially in the non-linear branch mainly the joint rotations are responsible for the total deformations. Joint rotations in ring 2 possess only 25% of total deformations and remain constant during the whole test and don't deviate more than 1%. Even more interesting is the minor increase in joint deformations in ring 2 at maximum loading although a severe increase in total deformations is observed. The segment curvatures in ring 2 are thus far greater compared to ring 1 and ring 3. Because ring 2 deviates from the other two rings a close up of this ring is presented in figure 5.10. In this graph the different available test results are compared to each other.

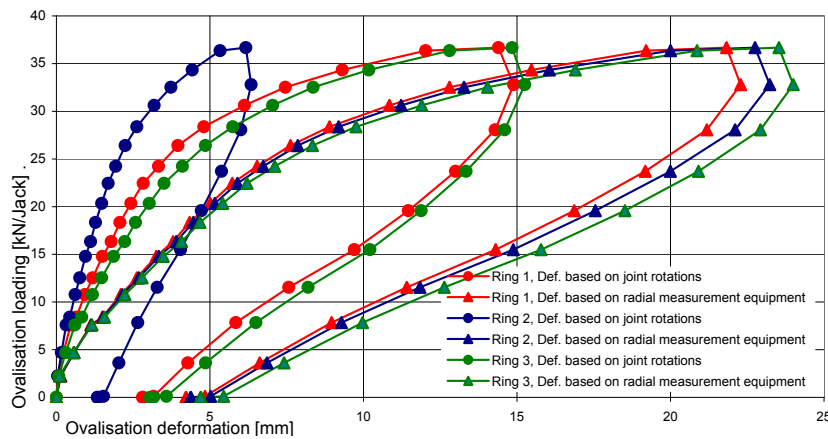


**Figure 5.9:** Ovalisation deformation of lining, experiment C01, deformations plotted separately for each ring, total deformation plotted and deformation only caused by joint rotations

In figure 5.10 the results of the calculated deformations based on joint rotations and segment curvatures, in the linear branch, are exactly the same as measured by radial equipment. This similarity indicates that reliable deformations are calculated based on joint rotations and segment curvatures. The moment that the load reaches  $18 \text{ kN/Jack}$  a discrepancy between calculated and measured deformations starts to appear. Investigating all strain gauges along the circumference of ring 2 learned that at that moment the strain in segment 7 drops all of a sudden. Before the drop occurred a very large strain was measured in this segment. It turned out that a longitudinal crack was already present in the middle of this segment. The abrupt drop of strains can be explained by a sudden further development of the crack. When this crack starts to become more severe the rotation of the complete segment is not measured anymore by the strain gauges and localizes in the crack. At that moment the deformation calculated starts to deviate from the measured deformation (TU1-TU12). The difference between this calculated deformation, based on joint rotations and segment curvatures, and the deformation, measured by radial deformation equipment, can say something about the order of cracking in a ring.

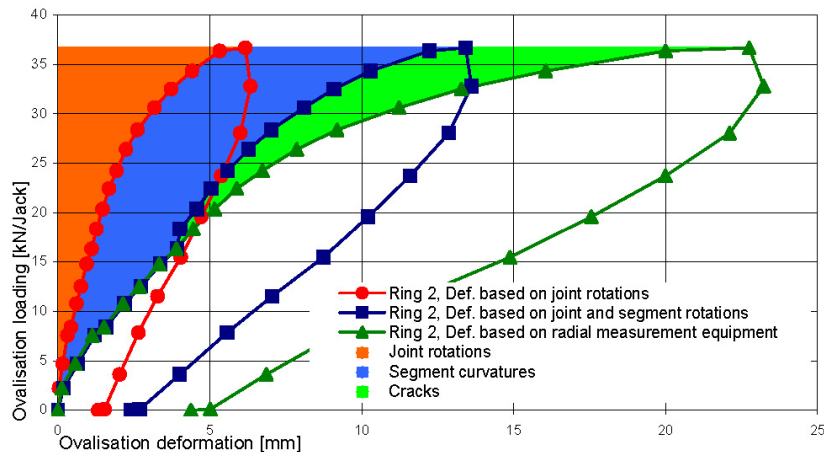


**Figure 5.10:** Deformation of ring 2, total deformation, deformation caused by joint rotations and deformation caused by joint rotations and segment curvatures, experiment C01

It is clearly confirmed that in ring 2 the joint rotations are very small compared to ring 1 and ring 3, and that the main deformations are caused by segment curvatures. In figure 5.10 an excessive increase in segment curvatures, as well as cracking, is shown in the final stages of loading. Observations during the experiment also confirmed the cracking of ring 2 during the experiment. When looking at the calculated deformations, based on joint rotations and segment curvatures, for the two neighbouring rings (Appendix E), only minor deviations from the deformations measured by the equipment outside the lining are noticed. This means that cracking is not dominating in the two outer rings, which is confirmed by observations of these rings during the experiment. In ring 1 and ring 3 the deformations are mainly caused by joint rotations. In ring 3 this part is even larger than in ring 1 which can be explained by the fact that ring 1 is somewhat more restrained by its active supports leading to little bit more segment forces. The curvatures of the segments do increase in these two rings but not as severe as they did in ring 2. Also the difference between the curvatures and the measured deformations is small, concluding that no severe cracking of the segments took place in the top and bottom ring. It can also be said that these segments did not reach their maximum capacity.

It has to be concluded that a strong interaction between the three rings was established. The cross-sections which possess two segment joints are the weakest spots and started to rotate heavily. Because of the strong axial interaction, the segments in ring 2 have to follow these rotations. In the final stages of loading an ongoing rotation of joints in the top and bottom ring starts to take place which is followed by the segments in the middle ring. This failure is accompanied by cracking of the segments in the middle ring.

The strong axial interaction, because of a relatively high axial force, resulted in the migration of forces to the middle ring. Eventually this ring was loaded until its maximum capacity was reached. At that moment no additional forces from the two adjoining rings could be carried resulting in failure.

## 5.2.2 Experiment C02

In this section the behaviour of the separate rings in experiment C02 is studied. In figure 5.11 the deformations of the lining, caused by joint rotations, are outlined per separate ring. Most deformations in experiment C02 are observed in ring 3 and ring 1. These are two rings with the same circumferential configuration of the joints, except for the key segment, so they should possess the same deformations. In experiment C01 the deformations of ring 1 and ring 3 were almost equal. In this experiment ring 3 shows larger deformations. Again this can be explained by the fact that the bottom ring encounters some hindrance from its active supports. Caused by the low axial interaction between the three rings different deformations of the separate rings took place.

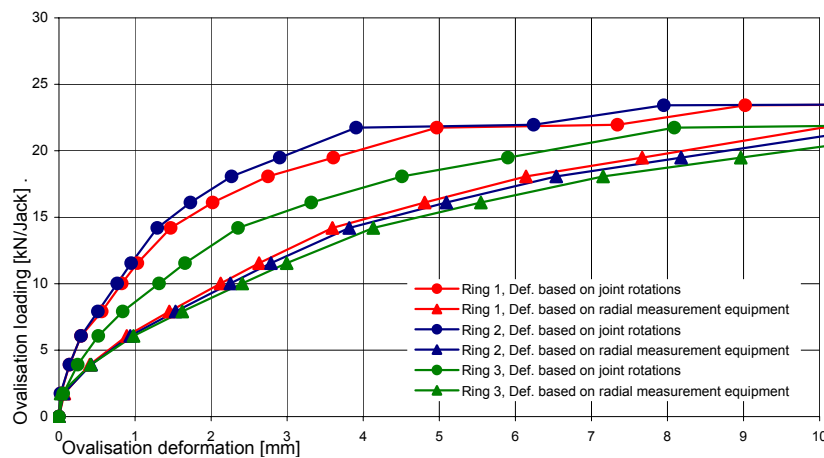


**Figure 5.11:** Ovalisational deformation of lining, experiment C02, deformations plotted separately for each ring, total deformation plotted and deformation only caused by joint rotations

From figure 5.11 it can be concluded that in this experiment the joint rotations are governing regarding overall deformations. Especially in ring 1 and ring 3 the joints are responsible for the largest rotations. Just like in the first experiment, the joint rotations in ring 2 are smaller compared to ring 1 and 3, although this difference between the three rings in experiment C02 is less. In figure 5.12 the relations between joint rotations and segment curvatures are graphically presented for ring 2. In Appendix E, the results of these calculations and measurements are shown for all three rings separately. When comparing the calculated deformations, based on joint rotations and segment curvatures, with the measured radial deformations (TU1-TU12) no discrepancies are found in the early start of the linear branch. Compared to the first experiment a deviation between the two lines start to occur earlier which can be explained by the fact that the segments were already cracked.

In the middle ring the joint rotations possess a smaller part compared to ring 1 and 3. The percentage of rotations caused by joint rotations is more or less equal as calculated for the first experiment. This means again that forces from ring 1 and 3 are transferred to and carried by ring 2. Until 22 kN/Jack of ovalisation load a strong interaction between the three rings is observed. After this loading is reached, a sudden increase in deformations is observed. When looking at figure 5.12 it learns that contrarily to C01 at which cracking initiated failure of

the lining, the joints are responsible for this jump. The deformations caused by the joints show a severe increase which is not observed in the deformations by strains or cracking. This behaviour of sudden increase in joint rotations is found in all three rings.

Ring 3 deforms the most out of the three rings and joint rotations govern the overall deformations. The localised rotations in the joint result in different radial deformations between ring 2 and 3 which result in interaction forces. The rotations are transferred to ring 2 leading to segment curvatures in this ring. From observations during the experiment it was found that additional cracks developed in this middle ring. At  $22 \text{ kN/Jack}$  the interaction forces could not be transferred to the second ring any longer and slip of the ring joints took place.

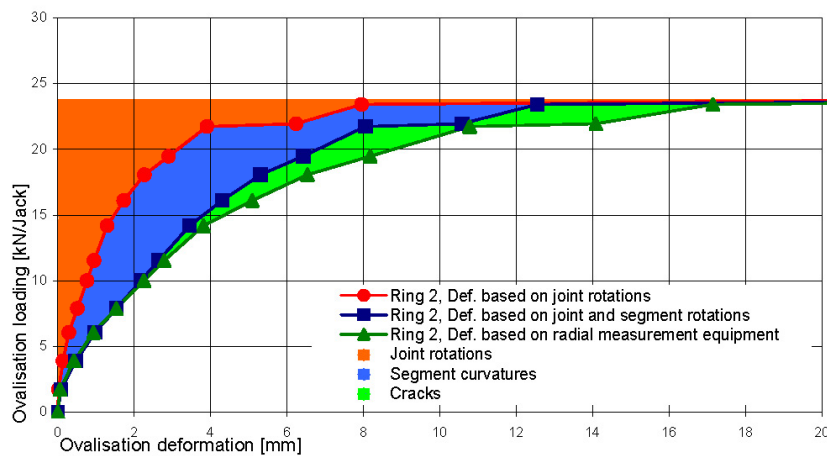


**Figure 5.12:** Deformation of ring 2, total deformation, deformation caused by joint rotations and deformation caused by joint rotations and segment curvatures, experiment C02

Because of slip of the ring joints a redistribution of forces in the lining is expected. Deformations and joint rotations increase until a new equilibrium situation is reached. This new equilibrium situation could possibly be reached by the participation of the structural dowels, but this has to be further investigated.

The joints in ring 1 and 2 also show a sudden increase in rotations although these are less severe compared to ring 3. From measurements it is concluded that the strains in the second ring also increase after slipping of the ring joints. This increase in strains is not as severe as the increase in joint rotations but it is indicating that the interaction forces in the ring joints remain or increase during slip of the ring joints. No unloading of the concrete segments after slip is noticed.

### 5.2.3 Comparing experiment C01 and C02

Based on figures 5.10 and 5.12 the portion of joint rotations, segment curvatures and cracking responsible for deformations is shown for ring 2. Both experiments show that in ring 1 and ring 3 joint rotations are governing for overall deformations. Because of the stretched bond layout of the segments, and interaction between the three rings, these joint rotations are transferred to ring 2 leading to large segment curvatures in ring 2. This is exactly what is

shown in the two graphs, in ring 2 the segment curvatures are governing instead of joint rotations. The difference in deformations caused by joint rotations between the three rings, is smaller in experiment C02 compared to C01, indicating that the interaction between the three rings was not optimal in the second experiment. Due to a less cooperation between the three rings in experiment C02 the lining did not fail by the excessive cracking of the segments but by an ongoing rotation of the joints.



## Chapter 6

# Critical Cross-Sections

In the previous chapters the global behaviour of the lining was treated. It was clear that three points on the lining started to rotate heavily during loading. These points were the cross-sections containing two segment joints and one concrete segment. If somewhere in the lining the maximum bending moment capacity of segments is reached than it will be in one of these cross-sections. To further investigate the behaviour in these sections the strain gauges located on the segments may be used. Due to large curvatures in these segments the concrete is cracked. Strain gauges on the tensile side of the concrete will therefore measure very high strains or very low strains depending on the location of the cracks in comparison to the location of the strain gauges. As a result, the curvatures cannot be easily determined in these sections and only the compression strains are reliable. Therefore, only the strains on the compression side of the concrete are investigated in this chapter.

### 6.1 Compression strains in experiment C01

The three critical cross-sections are located at a circumferential angle of  $-0,5\pi$ ,  $0,07\pi$  and at  $0,93\pi$ . If a plastic hinge develops in one or more of these three sections this should be visible by looking at the compression strains. In figure 6.1, the strains on the compression side of the concrete are shown for the segments in the three critical cross-sections. The values are taken from the strain gauges placed in the middle of the concrete segment. Strains only due to ovalisation and uniform radial loads are shown by subtracting strains recorded at reference step 10. The compression strain due to the normal force, introduced by the uniform radial load is calculated manually and is subsequently added up resulting in the strain in the concrete without the influence of lateral contraction.

The strains in the three cross-sections are almost equal. A linear and a non-linear branch can be distinguished in the curves. The transition between the linear and the non-linear branch is the very early starting of cracking of the concrete. On the tensile side of the concrete the tensile strength is reached and reinforcement will take over resulting in a smaller concrete compression zone. To get the same resulting compression force, the strain has to increase which is exactly what is seen in the graph. At an ovalisation load of  $36 \text{ kN/Jack}$  the maximum load is reached. At this point the load was kept constant while deformations were still growing. The strain gauges show an increase in compression. This may be indicated as a

plastic hinge developing. The plastic hinge develops at the same time in all three critical cross-sections. When three plastic hinges are formed an instable lining is created implying failure.

Two less critical cross-section are located at  $0,36 \pi$  and at  $0,64 \pi$ . These two cross-sections are also composed of one segment and two segment joints and are exposed to 64% of the bending moments (in a continuous lining) compared to the three most critical cross-sections. The compression strains recorded on these two less critical segments are also included in graph 6.1 and are more or less equal. All lines start to behave non-linear at a strain between approximately  $0,2\text{‰}$  and  $0,3\text{‰}$ .

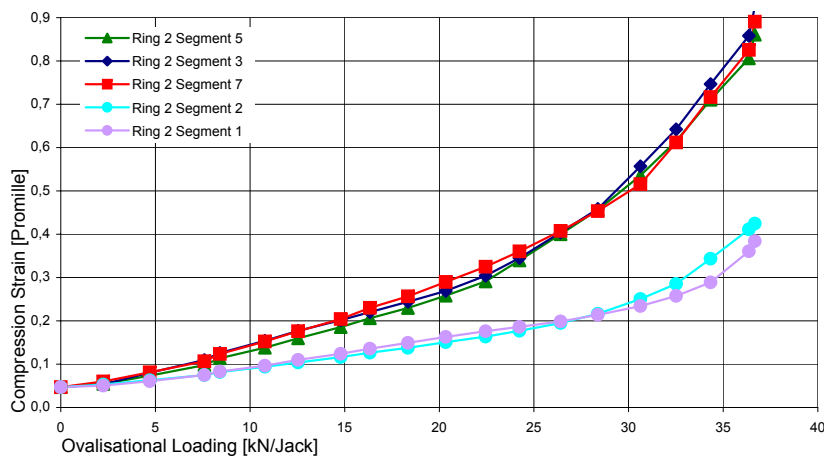


**Figure 6.1:** Measured strain on the compression surface of some critical segments

The concrete segments are lightly reinforced possessing a reinforcement ratio of  $0,16\%$ . According to the Dutch code a minimum required amount of reinforcement for FeB500 and B45 of  $0,21\%$  is needed. Therefore, the tensile strength of the concrete is of major importance to its structural behaviour. To investigate the influence of different tensile strengths, bending calculations are performed using the  $\sigma$ - $\epsilon$  relations for concrete in tension as shown in figure 6.2. In the same figure, a bending moment-curvature relation for a single concrete tunnel segment subjected to an increasing bending moment and a constant normal force is shown for the same tensile strengths. From this graph it is concluded that even for very low tensile strengths the maximum bending moment is reached before the steel yields. If the tensile strength of the concrete is above the  $4 \text{ N/mm}^2$  the reinforcement is not able to take over tensile forces at the moment of cracking. This behaviour might be very important regarding structural behaviour of the lining.

For the bending moment-curvature relations in figure 6.2 also compression strains can be derived. These compression strains are shown in figure 6.3. When comparing these different graphs for different tensile strengths with figure 6.1, it is concluded that a good agreement is found with tensile strengths around the  $4 \text{ N/mm}^2$ . In the final branch of loading the compression strains from the experiment do not follow the calculated strains. This can be explained by the fact of a changing normal force in the segment, a different fracture energy

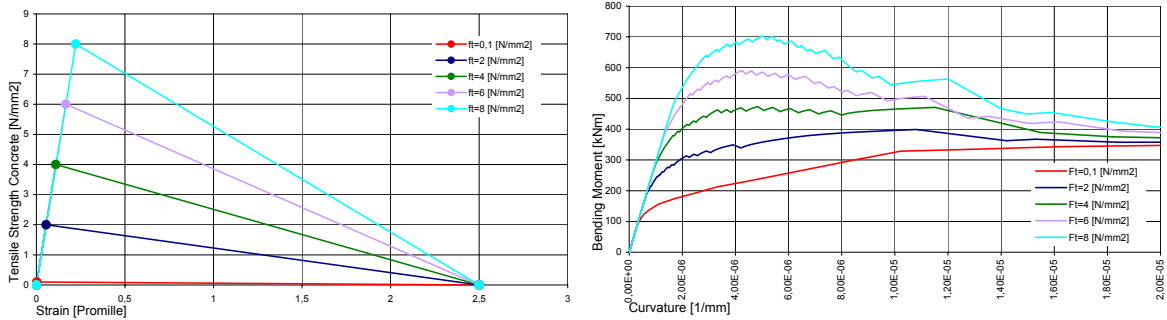


**Figure 6.2:** Tensile stress-strain relation of concrete for different values of the tensile strength (left) and bending moment-curvature relation for different values of the concrete tensile strength (right)

of the concrete or by another bending moment present than expected.

If the concrete segments in the experiment behave like the bending moment-curvature relation in figure 6.2 failure would be initiated by a sudden increase in deformations. When the bending moment capacity of some segments is reached a severe increase in rotations will be measured and reinforcement will start to yield. More important is the fact that this reinforcement will not be able, even at large curvatures, to carry the full bending moment again. At full capacity, before yielding of the steel, the concrete will start to crack heavily and failure will occur. From observations during the experiment this behaviour is confirmed. At  $36 \text{ kN/Jack}$  the load is not further increased due to the visible origination of cracks in some segments. If the reinforcement was able to take over the tensile forces an equilibrium situation should be reached and deformations should stop growing but even during unloading of the lining deformations were increasing. This means that a tensile strength of around the  $4 \text{ N/mm}^2$  was present in the concrete and, that for calculating the bending moment capacity of a single segment, the tensile strength is to be incorporated.

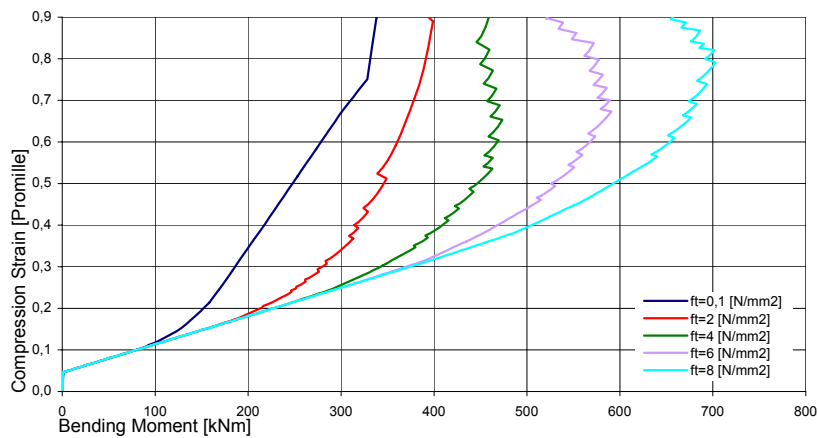


**Figure 6.3:** Strain on the compression side of a single segment subject to normal force and an increasing bending moment, results obtained from FE analyses

## 6.2 Compression strains in experiment C02

In the previous paragraph it was concluded that a tensile strength of around the  $4 \text{ N/mm}^2$  was present in the concrete. The experiment ended with the excessive cracking of the concrete resulting in failure. At the start of the second experiment the critical segments are thus cracked. From figure 6.2 it is clear that this might have a very large influence on the behaviour of the segments. This different behaviour should be recognizable from the compression strains on the same critical segments in the second experiment. In figure 6.4 the results from the second experiment are compared with results from the first experiment. The non-linear branch in the compression strain diagram is reached at a lower loading point. From this it can be concluded that the tensile strength in the second experiment is lower than in the first experiment. In the same graph the strains of the three sections are averaged and compared to the FE calculations. To be able to compare these graphs the bending moments in the lining are estimated based on a continuous lining. The total bending moment over the three rings is calculated analytically with subtraction of the expected bending moments in the neighbouring joints.

From the previous paragraphs it may be concluded that the different tensile strength in both experiments is responsible for the larger ovalisation deformations in the second experiment. Just like the compression strains found on the segments the ovalisation deformations found in the second experiment are larger and the non-linear branch is initiated earlier. Whether this is explained by the tensile strength of the concrete or by less interaction between the neighbouring rings maybe clarified performing FE calculations, described in chapter 10.

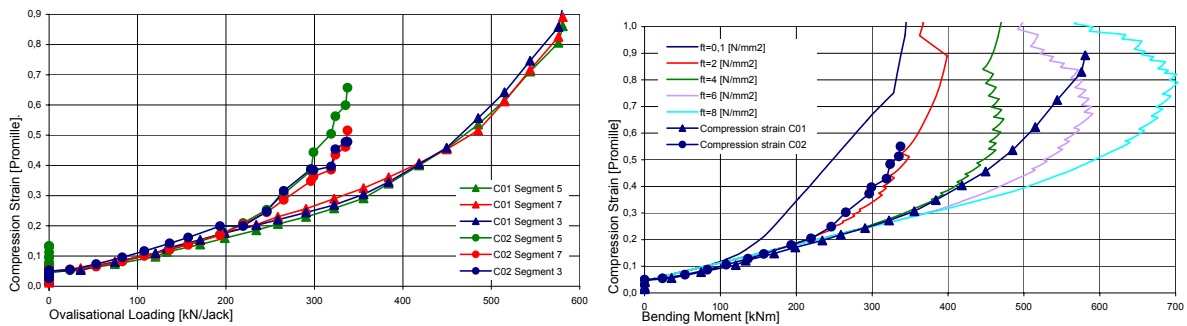


**Figure 6.4:** Compression strain in the three critical cross-sections in experiment C01 and experiment C02 compared (left) and average compression strain in the critical cross-sections compared to compression strains of FE calculations of a single segment for different values of the tensile strength (right)

## Part III

# Numerical Analysis



# Chapter 7

## Numerical analysis

### 7.1 Finite element modelling

For developing a realistic tunnel model, two things have to be modelled for which different possibilities are available. The modelling of the concrete lining and the modelling of the surrounding soil. Due to the fact that no soil is present in the full-scale test set-up, the modelling of soil is not treated here but is referred to Frissen et al. (1997). Boring through the soil in cooperation with the injected grout finally determines the load on the tunnel lining. In Verweij (1995), a complex FE analysis of this complete process of cutting and constructing is performed. The FE model which is developed in this master thesis does not contain the surrounding soil. The goal is to investigate the lining behaviour under an ovalisation load similar to the experiments. If it is possible to simulate the test results and understand the structural behaviour of the lining the next step could be including the surrounding soil. Because the structural behaviour is then known exactly the influence of the soil on structural behaviour and deformations can be analysed.

#### 7.1.1 Different element types for the modelling of a tunnel lining

In the following paragraphs different possibilities for modelling the three rings of the experiment are summarized. The modelling of the segments can be performed in two or three dimensions and different element types can be used. Correct modelling of the interaction between the segments is vital for a realistic behaviour. The interaction occurs at the contact areas in the segment and ring joints. Basically the segment joints can be left out simulating a continuous ring, or the joints can be modelled as a hinge or be given a rotational stiffness.

**Beam elements** The easiest way to model a tunnel is to make use of beam elements. In DIANA, basically three different types of elements may be used. The first types are the classical beam elements with directly integrated cross-sections. The cross-sections must be specified with the general parameters ‘area’ and ‘moment of inertia’ and therefore cannot be used in physically non-linear analyses. The second types are the fully numerically integrated classical beam elements. Because they are numerically integrated over their cross-section and along their axis they may be used in geometrical and physical non-linear analyses. Both types are based on the Bernoulli theory which does not take into account shear deformation and in which it is assumed that the cross-sections remain plane and perpendicular to the slope of

the beam axis. The third types of beam elements are based on the Mindlin-Reissner theory which do account for shear deformation. They may also be used in geometrical and physical non-linear analyses.

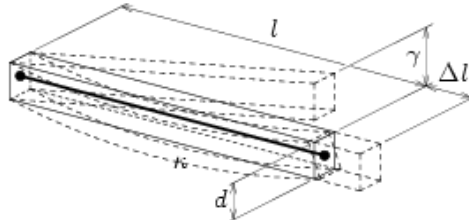


**Figure 7.1:** Characteristics of beam elements

To approximate the curved shape of the lining, higher order elements can be used. Furthermore, two or three dimensional elements may be selected describing translations in two or three directions. One dimensional elements possess two translational and one rotational degrees of freedom per node. Thereby, bending moments in the two other directions are neglected. Two dimensional elements possess three translational as well as three rotational degrees of freedom per node and can account for bending in two local directions and torsion. When restraining two rotational degrees of freedom this element will behave like the one dimensional element. Using beam elements for a FE model of the lining will result in a very simple model. The calculations do not need much computing power and the results are very comprehensible and physical phenomena can be recognized. Advantage of the low computing time is the possibility to change parameters and determine its influence on global lining behaviour. Being able to perform a lot of calculations in a very short time opens the possibility for doing probabilistic calculations like monte carlo.

Segment joints can easily be incorporated in the model by implementing linear or non-linear rotating springs. To investigate the influence of interaction between multiple rings, ring joints have to be modelled in between two tunnel rings. In existing models this interaction is modelled using coupling bars. These bars should be given such a length and stiffness that they behave like the actual joint and take forces in radial and tangential direction. They are located at places where in practice the packing materials are applied. It is also possible to model translational springs and assigning the ‘real’ stiffness of the ring joints.

Using beam elements results in simple FE models which give a lot of insight in occurring forces. The models can easily be constructed and a lot of insight in the behaviour of the construction is quickly gathered. Disadvantages are the limited possibilities for modelling of contact areas and the analysis of stresses on a more detailed level.

**Plane elements** To analyse strains and stresses along the thickness of the segments, plane elements may be used in which the coordinates of the element nodes must be in one flat plane. These are two dimensional elements which can be in plane strain or in plane stress. Plane stress elements are characterized by the fact that the stress components perpendicular to the face are zero ( $\sigma_{zz} = 0$ ) and may be applied if there is no out of plane bending. Plane strain elements are characterized by the fact that the strain components perpendicular to the

element face are zero ( $\epsilon_{zz} = 0$ ). Higher order elements may be used to get more accurate results. Compared to beam models, these models require more elements and the interaction in the joints is modelled differently. In the segment joints interface elements or contact elements can be applied. More material properties have to be assigned to an interface element resulting in a more realistic rotational behaviour. An advantage is the possibility to incorporate the influence of normal forces on the rotational stiffness. In the ring joints interface elements can describe the shear in radial and tangential direction as well as the resistance against rotation implicitly. Because the surface of the contact area between two segments of two different rings is modelled in two dimensions, the contact surface can also be modelled with two or three dimensional interface elements leading to a more realistic introduction of interaction forces into segments.

**Shell elements** To incorporate effects like the lateral contraction of concrete and axial jack forces, shell elements can be implemented. The loads may act in any direction between perpendicular to the surface and parallel to the surface. These elements describe forces in the third direction, which are not described by beam or plane elements. Typical applications of curved shell elements are the analysis of curved structures like shell roofs, storage tanks and ship or aircraft hulls. When only considering a single ring when modelling a tunnel lining, identical results will be found for beam models as well as for shell models. Shell models approximate reality more accurate when investigating the behaviour of multiple coupled adjoining rings on which an axial force is applied. Solving is more time consuming compared to plane elements but still results are comprehensible, bending moments as well as stresses and strains are outputted. The joints in a tunnel lining can be modelled exactly the same way as described previously.

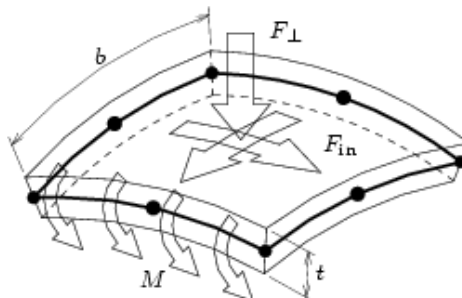
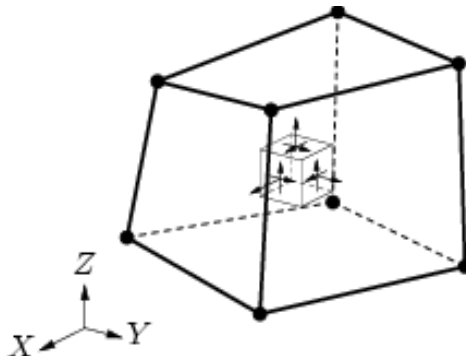


Figure 7.2: Characteristics of shell elements

**Solid elements** Solid elements should give the most detailed answers but because of the tendency to produce large systems of equations they are only used when other elements are unsuitable or if inaccurate answers are produced. They are difficult to develop and solving is time consuming. Because no bending moments but strains and stresses are outputted it is difficult to understand the structural behaviour of the complete FE model. Typical applications of solid elements are the analysis of voluminous structures like concrete foundations and off-shore structures, thick walls and floors, and soil masses. Just like for plane elements interface elements are used for segment and ring joints when modelling a tunnel lining.



**Figure 7.3:** Characteristics of solid elements

**Modelling of the joints** As previously described, the influence of joints on the global lining behaviour is significant. Most accurate results can probably be reached by using three dimensional models containing solid elements. This way the interaction between segments can be modelled realistically. By using friction interface models at the contact areas the resistance against shear and rotation is modelled. The concrete at these contact areas can be modelled linear elastic but also non-linear to incorporate plasticity and cracks. The development of these three dimensional interface elements is difficult and in combination with three dimensional modelling of the lining a very large system of equations is built. An alternative for getting realistic joint and segment behaviour is to only model the joints using complex interface elements. The segments can be modelled using shell elements resulting in a significant decrease in system size.

Easier would be to model the interaction by springs instead of interface elements. Segment joints can be modelled by applying rotational springs. To obtain a realistic behaviour a moment-rotation relation is implemented simulating reality. A non-linear Janssen or Gladwell relation can therefore be implemented. Another option is to perform complex three dimensional FE analyses on the rotational behaviour of a joint. In these models the effects of reduced contact thicknesses and non-linear material properties are incorporated. The found moment-rotation relation is accurate and can be simulated by a simple rotating spring that can be implemented in another FE model.

A problem that arises is the fact that the implemented relation is only valid for a certain normal force. When increasing the load the behaviour changes. Because of an ovalisation load the normal force along the circumference of the lining is also non-uniform resulting in different moment-rotation relations at different spots. Because the normal force has no influence on the rotational stiffness in the linear branch these elements can be used as long as rotations do not become non-linear. When segment joints start to behave in the non-linear branch it is questionable whether the rotating spring elements have to be changed by other more accurate elements which do incorporate for changing normal forces. In a segment joint also a radial deformation can take place resulting in shear of the contact areas. This effect can be neglected by tying translational deformations or by implementing translational interface elements.

An alternative for modelling segment joints is to locate a single beam element in between two segments. When giving this beam no tensile strength, the beam element can simulate rotations according to Janssen for different normal forces. Also the effect of a reduced contact thickness and plastic material behaviour can be implemented [Vervuurt 1997]. This method is probably a good way of modelling segment joints in beam models but requires a lot of testing to obtain accurate results and numerical stability might be a problem.

Just like for segment joints, the ring joints can be best modelled using three dimensional interface elements. In reality a friction between concrete and plywood is present as well as a shear force in the plywood itself. The material properties can be obtained from a translation-elongation diagram obtained from experiments. In these joints also a rotation in axial direction can take place. This can once again be modelled by a rotating spring or can be neglected by tying rotational degrees of freedom.

### **7.1.2 Results of earlier constructed FE models of tunnel linings**

In Vollema (1996) a comparison is made between the different possibilities described above to model a tunnel lining. These comparisons are performed using linear elastic material properties. For the results distinctions are made between single and multiple ring models.

In single ring models the maximum bending moments and normal forces are found on the quadrants of the lining. In multiple ring models maximum bending moments occur in cross-sections with multiple joints. When all concrete segments and ring joints possess an infinite stiffness, hardly any deviations in results are found between the different element models, just like the number of rings modelled does not have any influence.

When modelling a single ring with or without segment joints a shell model shows a stiffer response compared to beam models. This can be explained by the presence of membrane forces in shell elements. For the model including joints, the shear force in shell models is higher compared to beam models.

Larger bending moments are found when modelling two adjoining rings with beam elements, coupled by springs at the position of the segment joints. This is explained by the fact that the moment in two rings at a place of a segment joint has to be carried by one segment. At the position of a ring joint, moments are transferred to the adjacent ring, which results in higher bending moments in that segment. If the springs are moved a quarter of a segment, lower moments were found because on the spots where a ring joint is present both segments can carry the loading.

The positioning of the springs will have no effect [Vollema 1996] on maximum values for shear forces. When using more springs a little bit higher shear forces are found. The number and position of the springs is of major importance for bending moments and stresses. Using more springs lowers bending moments in the segments. In all models no differences are found in normal forces.

## 7.2 Single tunnel segment

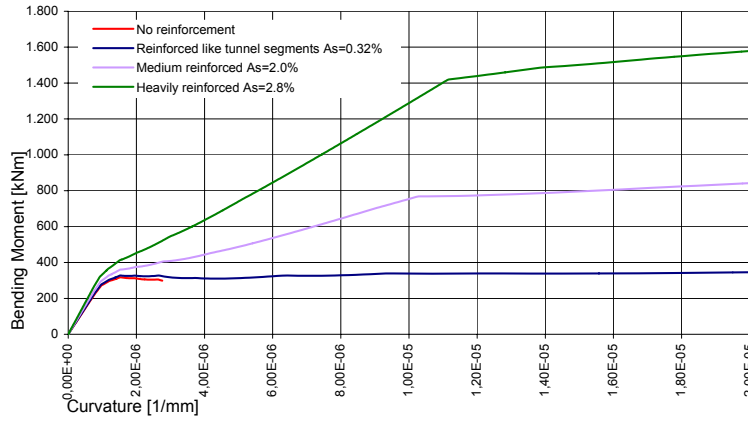
In the literature review the behaviour of the segment joints and the ring joints is extensively outlined. Theoretical analyses as well as the results of experiments are described leading to a good impression of their behaviour. Another important component of the lining are the tunnel segments itself. In this chapter the behaviour of a single segment is analysed using FE analysis.

The most important property of a single segment is the ultimate bending moment capacity. This bending capacity is very easily calculated analytically by assuming that the concrete takes all compression forces and the reinforcement carries all tensile forces. This results in a bending moment capacity of the segment of  $320 \text{ kNm}$ . The assumption of not taking into account the tensile capacity of concrete is based on the fact that at ultimate curvature most of the concrete in the tensile zone is cracked and that the uncracked part of the tensile zone is negligible small. In contrast to this approach, the tensile properties of the concrete tunnel segments might not be negligible, depending on the reinforcement ratio. In the following section the importance of the tensile properties are discussed and the bearing capacity of the tunnel segments is estimated.

### 7.2.1 Bending moment-curvature relation of a tunnel segment

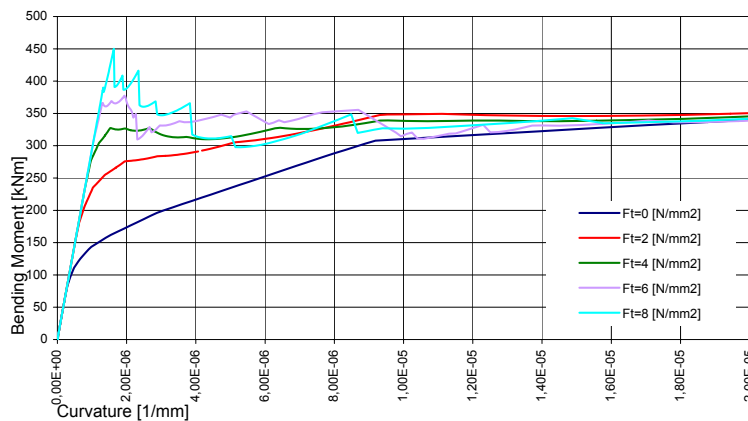
For studying the bending behaviour of a single tunnel segment, it is useful to plot a moment-curvature relation. For this purpose a single segment is modelled as a straight beam with length  $4.000 \text{ mm}$ , subject to a constant normal force and an increasing bending moment. This segment is subdivided into 40 finite beam elements resulting in a constant element length of  $100 \text{ mm}$ . As previously mentioned, a very low amount of reinforcement is located in the segments. The effect of the amount of reinforcement on the bending moment-curvature relation is presented graphically in figure 7.4.

In case no reinforcement is applied the concrete takes all tensile forces resulting in a maximum bending moment capacity of  $338 \text{ kNm}$ . After reaching this peak moment the bending moments will drop with increasing curvature until the segment fails due to a fully developed crack. For 'normal' amounts of reinforcement the reinforcement takes the tensile forces from the concrete and the maximum bending moment is reached when the reinforcement reaches its yield strength. The more reinforcement is applied, the higher the bending moment capacity will be. For the reinforcement amount as used in the tunnel segments, the amount is just enough to take over the tensile forces in the concrete. At increasing curvatures the stresses in the reinforcement cannot increase resulting in a constant, not increasing, bending moment. Failure will occur the moment the ultimate strain of the reinforcement is reached, or the moment the ultimate compression strain of the concrete is reached. The calculation of the bending moment-curvature relations is performed taking into account a tensile strength of  $4 \text{ N/mm}^2$  for the concrete. If a higher tensile strength is applied it is obvious that the applied amount of reinforcement is not enough to take over all tensile forces. In figure 7.4 also two curves are plotted for higher percentages of reinforcement. The effect is obviously an increase in bending moment capacity. More important to notice is that for these higher reinforcement ratio's the influence of the tensile properties of the concrete is negligible.



Input data	
Element type	CL9BE
Element length	100
Beam height	400
Beam width	1500
Nr. int. points	31
Nr. elements used	40
Sim. performed	force contr.
YOUNG	36.000
POISON	0,2
CRKVAL	4
TENSIO	Hordyk
GF	0,1
CRACKB	50
YIELD	DRUCKE
YLDVAL	26 0,17 0,17

Figure 7.4: Effect of amount of reinforcement on bending moment-curvature relation



Input data	
Element type	CL9BE
Element length	100
Beam height	400
Beam width	1500
Nr. int. points	31
Nr. elements used	40
Sim. performed	force contr.
YOUNG	36.000
POISON	0,2
TENSIO	Hordyk
GF	0,1
CRACKB	50
YIELD	DRUCKE
YLDVAL	26 0,17 0,17
$A_{steel}$	$864mm^2 = 0,32\%$

Figure 7.5: Effect of tensile strength of the concrete on bending moment-curvature relation

From the bending moment-curvature relations shown above, it is concluded that the applied amount of reinforcement in the tunnel segments not raises the bending moment capacity after reaching the tensile strength of the concrete. For this reason the influence of the tensile properties of the concrete might be of major importance to the bending behaviour of the segments. To investigate this, the amount of reinforcement is set to the amount as used in the experiments, and the tensile strength of the concrete is studied by changing its value. For five different values of the tensile strength, bending-moment curvature relations are obtained and shown in figure 7.5.

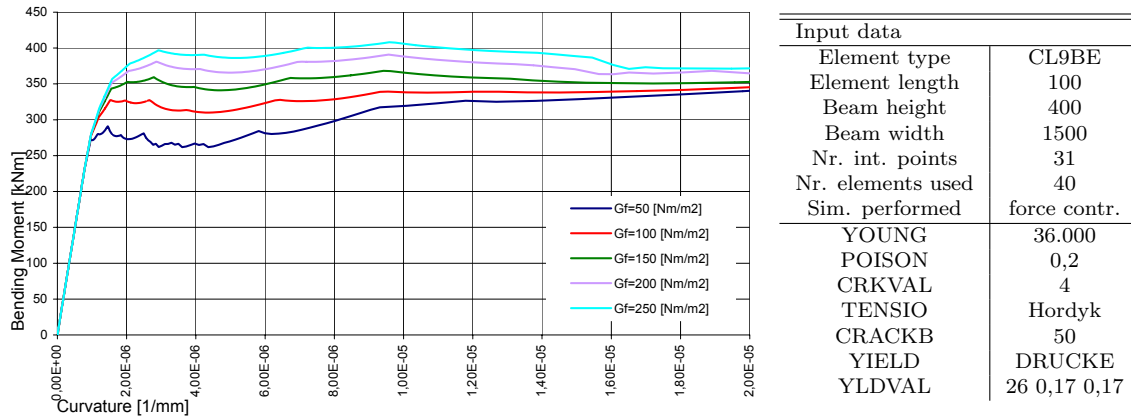


Figure 7.6: Effect of fracture energy on bending moment-curvature relation

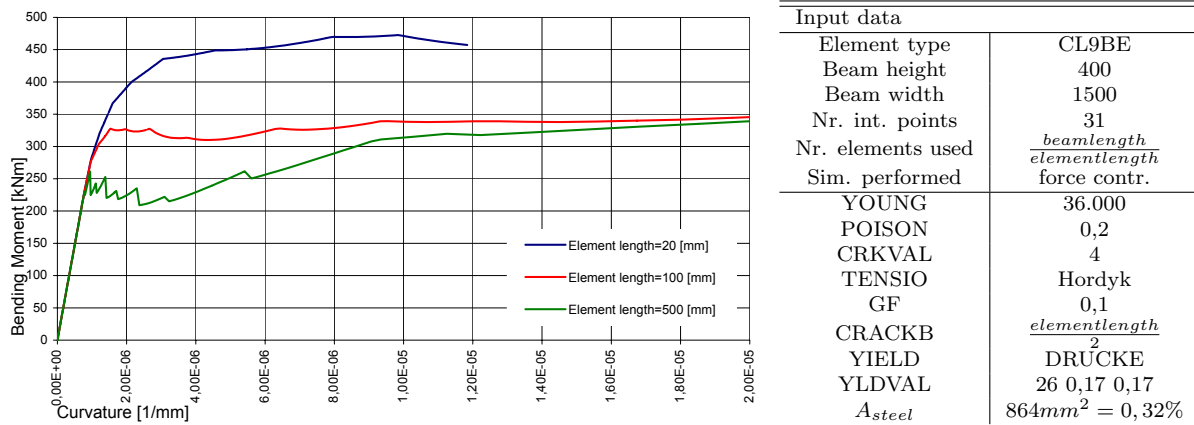


Figure 7.7: Effect of element size on bending moment-curvature relation

It can already be concluded that if tensile strengths higher than  $4 N/mm^2$  are applied, a peak bending moment is reached without reaching the yield strength of the reinforcement. The tensile strength of the concrete, which is usually disregarded, results in cases that the peak bending moment overcomes the bending moment of limit design. The point that the plotted curves deviate from the linear branch, the maximum tensile strength of the concrete is reached and a non-linear behaviour is recognized. With increasing curvatures the bending moments drop to the point in which the reinforcement is ‘activated’. How quick this is reached depends on the softening behaviour of the concrete which is characterised by the fracture energy. To investigate the influence of the fracture energy on the bending behaviour, again some FE calculations are performed in which the fracture energy of the concrete is changed. The influence of this parameter is shown in figure 7.6. For the higher values of the fracture energy the bending moment can significantly increase after reaching the tensile strength at the outer fibres of the concrete.

The analyses performed in the previous paragraphs are based on FE calculations on a single tunnel segment. During calculations it became clear that the results of the calculations are

very mesh dependent. In figure 7.7 the results of different used element sizes are shown. Using a course mesh resulted in a relatively low bending moment capacity in comparison to using a fine mesh which resulted in a high bending moment capacity. This mesh dependent behaviour seems to be only of influence in the non-linear branch of the bending moment-curvature relation and obviously has something to do with the softening parameters of the concrete. This in combination with the fact that it is expected that the tensile parameters have a large influence on the bending behaviour, it is very important to know how cracks develop in concrete and how DIANA processes the softening behaviour.

## 7.2.2 Softening behaviour of concrete

Before going into detail about the numerical aspects of dealing with softening of the concrete, a brief review of the tensile properties of concrete are discussed. For understanding the fracture behaviour of the concrete Hillerborg (1976) proposed the ‘fictitious crack model’. In this model a distinction is made between a ‘visible crack’ and a ‘fictitious’ crack ahead of the visible crack, see figure 7.8. In this model a ‘visible’ crack does mean a crack which cannot transfer tensile stresses, whereas the ‘fictitious’ crack can transfer tensile stresses. The stress in the softening branch depends on the crack opening in the ‘fictitious crack’. The relation between crack opening and stress is obtained from a deformation-controlled uniaxial tensile test.

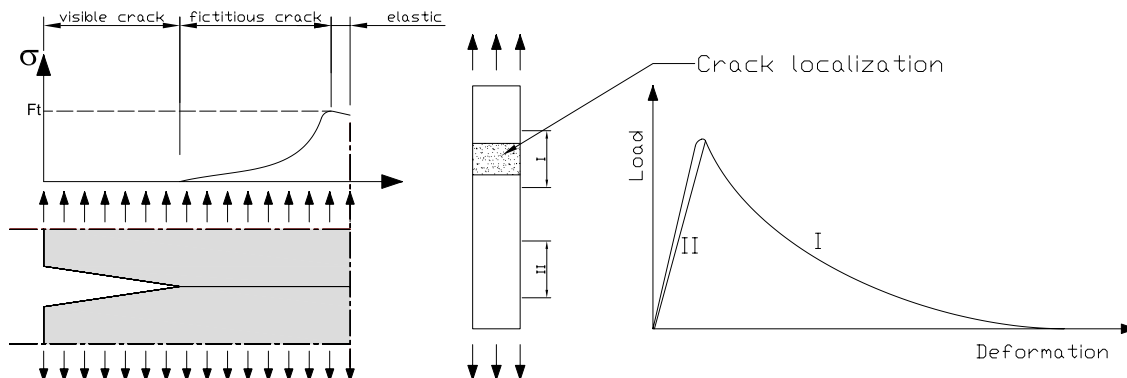


**Figure 7.8:** Fictitious Crack Model proposed by Hillerborg in 1976 (left), concrete bar strained uniaxial in tension (middle) and load-deformation relation for concrete bar (right)

When a bar is strained in tension, in a deformation-controlled experiment, it first reacts elastically and the obtained linear load-deformation relation can directly be replaced by a stress-strain relation for the material. At the moment the tensile stress reaches its strength, strains start to localize within a narrow zone in which micro cracks develop, zone I in figure 7.8. Stresses that can be transferred don't suddenly drop to zero but decrease with increasing deformations. This process will occur in the weakest cross-section of the concrete bar whereas the remaining cross-sections remain elastic, meaning that stresses drop according to a linear stress-strain relation. In the cross-section in which cracking starts it is not longer valid to use a stress-strain relation, because the strains are influenced by the length over which is measured. Caused by the localization of cracks, the concrete bar can be split up into a stress-strain relation for the concrete outside a crack and a stress-crack opening relation

for the crack itself. In figure 7.8 a concrete bar loaded by a tensile force and its resulting load-deformation relation for the cracking zone as well as for the elastic zone is shown.

The obtained crack-stress relation from an uniaxial tensile test is valid for an infinitely small width and causes problems when modelling with finite elements. To create the possibility of having cracks on arbitrary locations, a smeared crack approach is used. This so called Crack Band Model approach was firstly proposed by Bazant (1976). The basic idea of this model is to characterize the material behaviour in the fracture zone in a smeared manner through a strain-softening constitutive relation. When the tensile strength of the concrete in a certain element is reached the stress-crack opening relation, obtained from the uniaxial tensile test, is transformed into a stress-strain relation. The stress-strain relation is formed such that every single element is able to describe a single crack, hence, every element possesses such a stress-strain relation that measuring over a complete element a crack-stress relation according to an uniaxial tensile test is obtained. The equivalent strain is calculated according to equation 7.1 and depends on the distance,  $h_{cr}$ , between two integration points perpendicular to the crack direction.  $h_{cr}$  is also called the crack bandwidth.

$$\epsilon_{cr} = \frac{W}{h} \quad (7.1)$$

The transformation of a stress-crack width relation into a stress-strain relation is explained graphically in figure 7.9 by introducing a material parameter  $G_f$  which is called the fracture energy. The fracture energy is the area under the stress-crack relation and represents the energy absorbed in the crack formation per unit area of the cross-section, hence, per unit area of crack. This fracture energy is a material parameter and together with the crack bandwidth the stress-strain relation is determined. By setting the crack bandwidth equal to the length of an element, every single element is able to simulate one single crack.

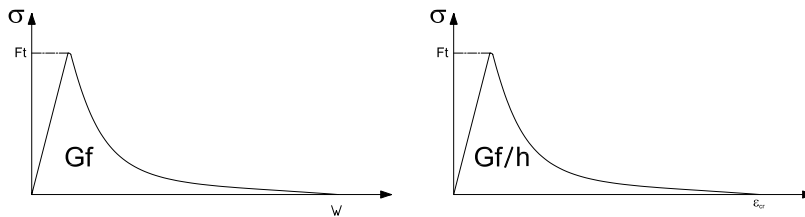


**Figure 7.9:** Crack-stress relation of a uniaxial strained bar (left) and corresponding stress-strain relation in which  $h_{cr}$  is the crack bandwidth of a finite element

By transforming the stress-crack width relation into a stress-strain relation, the initiation of cracks can now be simulated using finite elements independent of the used element size. The softening curve of the concrete deals with the stresses in such a way that the corresponding strain results in the correct crack width. So, when using beam elements a softening curve is applied to deal with the crack width. When using long elements a ‘light’ softening curve has to be applied to describe the same crack. When using short elements a ‘heavy’ softening curve has to be applied to describe the same crack. The influence of the element size on the stress-strain relation is explained graphically in figure 7.10.

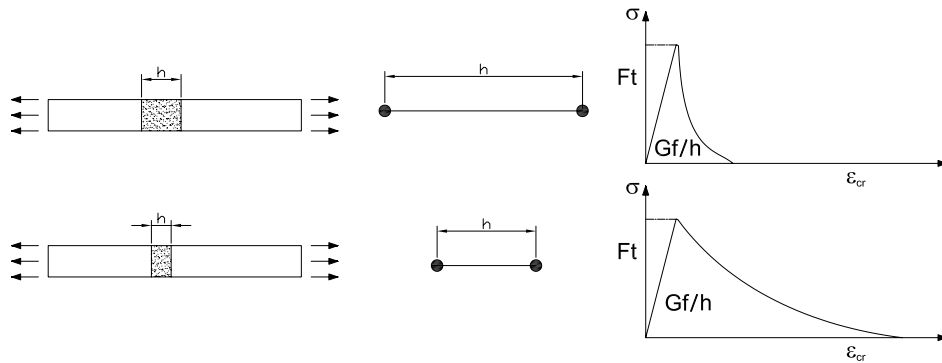


**Figure 7.10:** Effect of element length on stress-strain relation, course element (top) and fine element (bottom)

For bars, uniaxial strained, the maximum load capacity is reached at the moment that the tensile strength is reached and is *independent* of the shape of the softening curve. In contrast to these simple bars, the bending moment capacity of a concrete beam is *dependent* on the shape of the softening curve. Softening may increase the peak bending moment capacity of a beam. To illustrate this behaviour, a simply supported notched unreinforced concrete beam is subject to bending using FE calculations. Only the element at mid span is given non-linear concrete properties as the rest of the notched beam is modelled elastically. By changing the length of the element at mid span indirectly different stress-strain relations are assigned to the beam. This FE calculation is described in Hordijk (1991) and the load-deflection diagram is shown in figure 7.11. From the graph it is concluded that the load capacity of an unreinforced concrete beam is affected by the shape of the softening curve. The effect of the shape of the softening diagram on the load bearing capacity of concrete beams is extensively treated in Alvaredo and Torrent (1987).

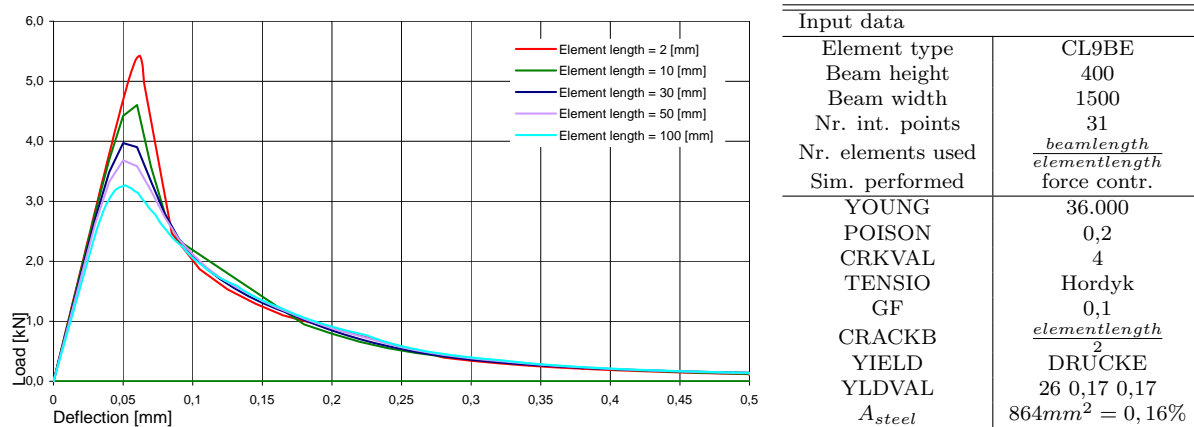


**Figure 7.11:** Influence of crack bandwidth on the force-deflection relation of a three point bending test

The variable softening diagrams are responsible for the mesh sensitive behaviour observed in figure 7.7. To avoid spurious mesh sensitivity and achieve objectivity for concrete beams

subject to bending, it is necessary to assure that the energy dissipation due to fracture per unit length and width is constant. Therefore the length of elements should not vary too much.

If straining a concrete bar uniaxially the fictitious crack model can be well used and is defined by two parameters  $G_f$  and  $f_t$ . The crack bandwidth is derived from the distance between the integration points which is the same as the crack bandwidth in this case. For a beam subject to *bending* the crack bandwidth cannot any longer be derived from this distance. Therefore, this crack band model is characterized by three instead of two parameters  $f_t$ ,  $G_f$  and  $w_c$ , in which  $w_c$  is the crack bandwidth. The width of the crack band can be assumed to be approximately  $w_c \approx 3 \times d_{max}$  according to Bazant and Oh (1983) in which  $d_{max}$  represents the maximum aggregate size. This conclusion was drawn on the basis of curve fitting experimental obtained data, although  $w_c$  values ranging from  $d_{max}$  to  $6 d_{max}$  gave also good results. In Bazant (1989) the influence of the parameter  $w_c$  is estimated to be rather weak for situations with isolated cracks but important for situations in which parallel closely spaced cracks do occur, like concrete beams with the presence of tension reinforcement. In that case the parameter  $w_c$  basically determines the minimum possible crack spacing.

$$S_{r,max} = 3,4c + 0,425k_1k_2\frac{\phi}{\rho} = 468mm \quad (7.2)$$

The minimum possible crack spacing can be derived from the material and geometrical properties of the beam. According to EuroCode 2 the maximum crack spacing  $S_{r,max}$  is given by equation 7.2. The minimum crack spacing is half of the maximum crack spacing which results in  $468/2=234 mm$ . The occurring crack spacing in a uniaxial restraint bar varies between these two values. According to Walraven and Galjaard (1997) more or less the same values are found. After the experimental full-scale tunnel tests were performed a map including all visible cracks and their positions was drawn. On the most heavily loaded segments crack spacings of around the  $300 mm$  were found after completion of experiment C01, whereas after completion of C02 more densely spaced cracks were found. The exact spacings were not determined after the experiments but it indicates that closely spaced cracks are possible.

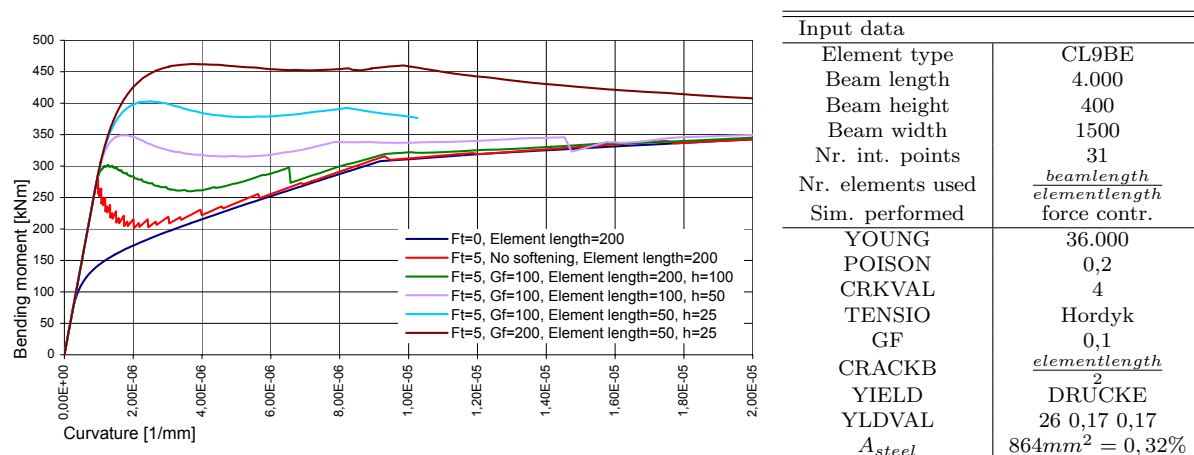
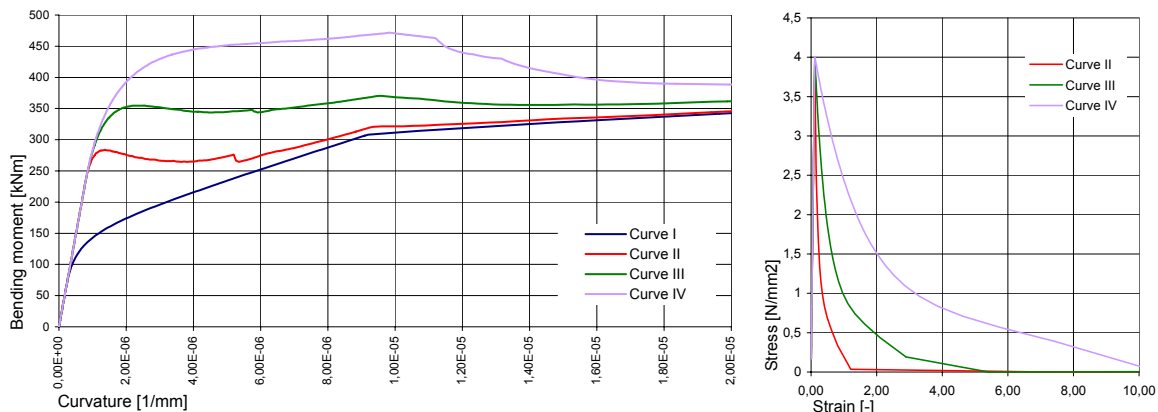


Figure 7.12: Bending moment-curvature relations for different concrete properties

Due to the fact that the softening properties of the concrete are uncertain and more important are of significant influence on the segment behaviour, a bending moment-curvature relation can be based on things which are known for sure, or what the segments can carry at least without the incorporation of softening. In figure 7.12 a bending moment-curvature relation is plotted which is based on concrete without tensile properties. This represents a lower limit for the bending behaviour of the concrete. A likely tensile strength of the concrete is  $4 \text{ N/mm}^2$ . This strength is almost certainly reached during the experiment and by assigning no tension softening, brittle behaviour, the red line in figure 7.12 is also almost sure a lower limit. By assigning conservative softening properties to the concrete the green line can also be considered as a lower limit. By shortening the length of the finite elements to  $100 \text{ mm}$  a crack bandwidth of  $50 \text{ mm}$  (quadratic elements including two integration points along its length) is reached which is equivalent to three times the maximum aggregate size of the concrete. The obtained curve using these concrete properties is still a likely situation. For higher values of the fracture energy or by decreasing the element length even further, higher bending moment-curvature relations are obtained, but it is uncertain whether the found bending moments were reached during the experiment.



**Figure 7.13:** Four different bending moment-curvature relations which are imported in the complete lining model (left) and used tension softening diagrams (right) (independent from element size)

To deal with the uncertainties described above, four bending moment-curvature relations are given in figure 7.13 which are implemented separately in the FE model of the complete tunnel lining. The blue line gives a lower limit meaning that the obtained FE results should give a lower load capacity of the lining compared to the experimental obtained load capacity. The green and red lines in figure 7.13 are possibly somewhat closer to reality, compared to the blue line, but it is not certain whether the concrete segments were really able to carry those bending moments. The peak bending moment reached by the most optimistic curve is  $470 \text{ kNm}$ . This is reached by a somewhat ‘heavy’ softening curve but with a tensile strength of  $4 \text{ N/mm}^2$ . In table 7.1 all relevant input parameters belonging to the four different bending moment-curvature relations are given.

Curve I		Curve II		Curve III		Curve IV	
YOUNG	36.000	YOUNG	36.000	YOUNG	36.000	YOUNG	36.000
POISON	0,2	POISON	0,2	POISON	0,2	POISON	0,2
CRACK	1	CRACK	1	CRACK	1	CRACK	1
<b>CRKVAL</b>	<b>0</b>	<b>CRKVAL</b>	<b>4</b>	<b>CRKVAL</b>	<b>4</b>	<b>CRKVAL</b>	<b>4</b>
TENSIO	5	TENSIO	5	TENSIO	5	TENSIO	5
<b>GF</b>	<b>0</b>	<b>GF</b>	<b>0,1</b>	<b>GF</b>	<b>0,15</b>	<b>GF</b>	<b>0,2</b>
<b>CRACKB</b>	<b>100</b>	<b>CRACKB</b>	<b>100</b>	<b>CRACKB</b>	<b>50</b>	<b>CRACKB</b>	<b>20</b>
TAUCRI	1	TAUCRI	1	TAUCRI	1	TAUCRI	1
BETA	0,01	BETA	0,01	BETA	0,01	BETA	0,01
YIELD	Drucke	YIELD	Drucke	YIELD	Drucke	YIELD	Drucke
YLDVAL	26	YLDVAL	26	YLDVAL	26	YLDVAL	26
	0,1736		0,1736		0,1736		0,1736
	0,1736		0,1736		0,1736		0,1736

**Table 7.1:** Input data to obtain the four bending moment-curvature relations as shown in figure 7.13

The bending moment-curvature relations obtained above will be implemented in the FE model of the complete tunnel lining. This complete model has an element length of 200 *mm* meaning that for Curve III and IV the crack bandwidth  $w_c < h_{cr}$ . When  $w_c < h_{cr}$  the localisation of cracks is described less accurate but it is estimated that it does not affect the structural behaviour. Care should be taken during the analysis and the interpretation of the results in the cracked segments. Only when analysing the localisation and development of cracks it might be better to build a new FE model with decreased element sizes.

### 7.3 Simplified tunnel model

To investigate the influence of plastic hinges in the lining a simple FE model is considered. Three tunnel rings are modelled without segment joints and are coupled by springs representing the ring joints. The continuous rings are equally loaded by an ovalisation radial load of  $10\text{ N/mm}$  and the calculations are performed according to the theory of linear elasticity. After applying this load, a plastic hinge is installed in ring 1 and ring 3. These two hinges are installed on the same circumferential location as where the bending moments, due to the ovalisation load, reach their maximum values. Subsequently the load is doubled to  $20\text{ N/mm}$ . As a result of the installed plastic hinges, the bending moment capacity in those spots is reached, leading to a redistribution of bending moments. Because no plastic hinge in the middle ring is present, bending moments are transferred to this middle ring by the ring joints, modelled as springs. Bending moments are also redistributed in the ring itself. The results are treated in the following paragraphs.

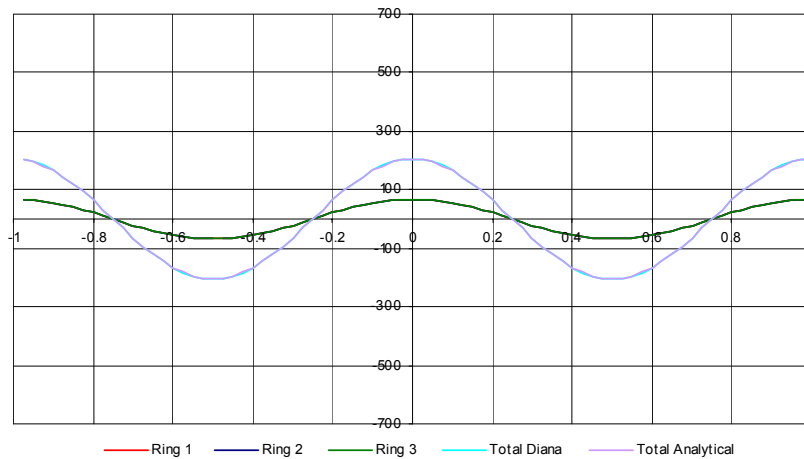


**Figure 7.14:** Overview of bending moments in the lining, three continuous rings without plastic hinges, load  $10\text{ N/mm}$ , ring 1, 2, 3 and the analytical derived bending moments possess the same curve

At an ovalisation load of  $10\text{ N/mm}$ , the bending moments are equal in all three rings and agree with analytically expected values (7.14). After applying the load, two plastic hinges are installed at one of the four spots where maximum bending moments are present. This is simulated by removing one element from ring 1 and ring 3 and put nodal moments on the two ends of the removed element. When this moment is applied the ovalisation radial load is doubled. The bending moments in ring 1 and ring 3, at the place of the plastic hinges, cannot increase leading to a redistribution of bending moments. In figure 7.15 the results of the bending moments in the lining at an ovalisation load of  $20\text{ N/mm}$  are shown including the combined bending moments in the ring and the analytical expected combined bending moments. Because bending moments in ring 2 are higher than expected, based on analytical values, it can be concluded from this graph that a part of the bending moments in ring 1 and ring 3 are transferred to the middle ring. It can be seen that bending moments in ring 1 and ring 3 do not increase and that ring 2 carries additional loading. However, the bending moments in the three rings combined are not the same as the analytically expected bending

moment at that point. This indicates that a part of the forces is redistributed in the ring itself. This is explained by the fact that redistribution of bending moments to the middle ring leads to a larger curvature of the cross-section at that spot in ring 2. These additional curvatures are compensated by an additional curvature along the whole circumference of the lining. In case of a more complex system this can also be compensated in other segment joints or plastic hinges along the circumference of the lining.

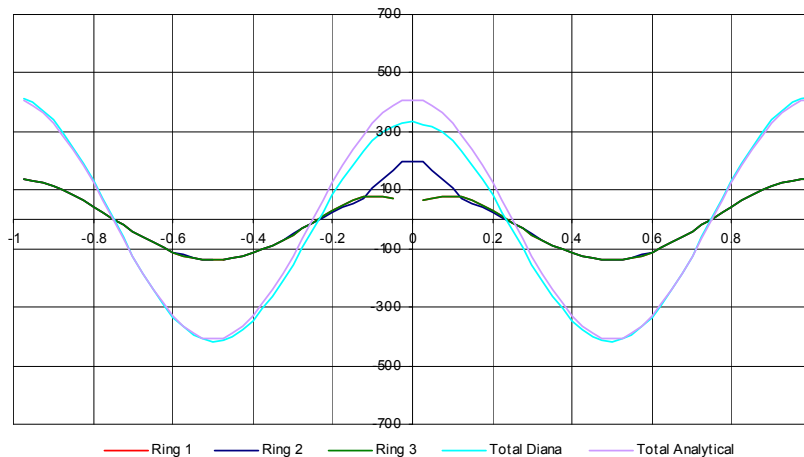


**Figure 7.15:** Overview of bending moments in the lining, three continuous rings with plastic hinges in ring 1 and ring 3 at  $0 \pi$ , ovalisation load  $20 \text{ N/mm}$ , ring 1 and 3 possess the same curve

The portion of bending moments that is transferred by a redistribution to the middle ring or by a redistribution in the ring itself is related to the stiffness of the ring joints. A high spring stiffness leads to a high redistribution of bending moments to the middle ring. A low spring stiffness leads to redistribution of bending moments in the ring itself. In the extreme case of no interaction between the three rings all bending moments are redistributed in the ring itself. For different values of the spring stiffness the percentage of redistribution to the middle ring or in the ring itself is shown in figure 7.16. In case of an eternal spring stiffness half of the bending moments are transferred to the middle ring and half of the bending moments are redistributed in circumferential direction. Realistic values for the spring stiffness, when using plywood or concrete-to-concrete contact is established, lay in the range varying between  $10^5 \text{ N/mm}$  and  $10^7 \text{ N/mm}$  resulting in a redistribution in the ring itself of 52% to 66%. This percentage is not only affected by the stiffness of the ring interaction but also by the distance between the two installed moments in a single ring. It is expected that this distance will influence results but it is not investigated how much.

When increasing the load only by a little, just after the two plastic hinges in ring 1 and ring 3 are installed, bending moments are mostly redistributed in circumferential direction. Increasing the loading even further also redistribution to the middle ring takes place. When the loading is doubled, a stable situation is reached meaning that redistribution of moments will take place according to figure 7.16.

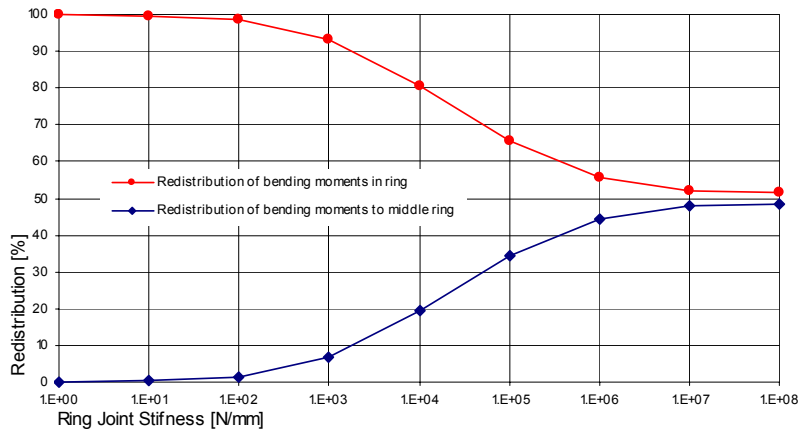


**Figure 7.16:** Redistribution of bending moments

Having applied a load of  $20\text{ N/mm}$ , the maximum bending moment is present in ring 2 at the circumferential position of the hinges in ring 1 and ring 3. The element at that point in ring 2 is removed and an equivalent nodal bending moment is installed, resulting in an ongoing plastic hinge in axial direction along the cross-section. When increasing load again, the only way of redistribution of forces is by redistribution in circumferential direction. The results of three rings loaded by an ovalisation radial load of  $30\text{ N/mm}$  and three plastic hinges at the same position in all three rings is shown in figure 7.17. It is seen that the bending moment at  $0,00\pi$  is not increased whereas along the remaining part of the lining the bending moments are higher than analytically expected. Because the calculation is performed linear elastic, the bending moments are directly related to the curvature in the concrete. The additional rotations in the plastic cross-section are compensated by the entire lining and therefore higher bending moments are found along the whole circumference compared to analytical values.

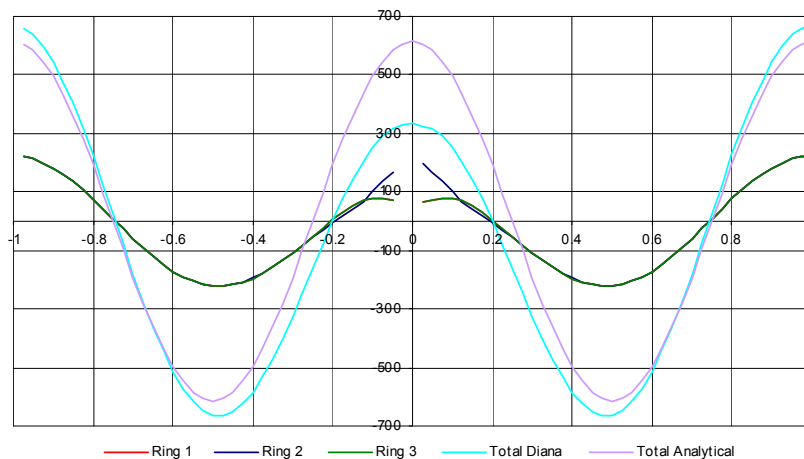


**Figure 7.17:** Overview of bending moments in the lining, three continuous rings with plastic hinges in every ring located at  $0\pi$ , load  $30\text{ N/mm}$ , ring 1 = ring 3



## Chapter 8

# Description of FE Models

In order to obtain a detailed description of the actual behaviour of the experimental tunnel lining a three dimensional FE model using solids should give the most detailed results provided that a very fine mesh is used. On the other hand, those models require a large amount of processing capacity. Another large problem of complicated three dimensional models is that they are less comprehensible and the detailed output results are difficult to correlate to physical processes. Also, from an engineering point of view there is a need for simple and reliable FE models. To predict the ultimate load capacity due to an ovalisation load, one and two dimensional models are probably the best option. To validate the numerical calculations two models are built, a one dimensional model using beam elements and a two dimensional model using plane stress elements. These two models are described in the following sections.

### 8.1 1D FE model

In this section the simplest model of all is described using beam elements. This 1D model will require a very short processing time and a lot of insight in the structural behaviour is quickly gathered. The axial jack forces cannot be incorporated and the material properties of the plywood in between succeeding rings therefore have to be changed manually when another axial force is applied. The geometry and the physical properties of the 1D model are separately treated in the following sections.

#### 8.1.1 Geometry of FE Model

The FE model is composed of three rings to be able to compare results with experimental results from the full-scale test. Each ring is, just like the experiment, built up out of 7 normal segments and 1 key segment. To model the segments, 2 dimensional 3 noded beam elements (**CL9BE**) are used. The normal strain  $\epsilon_{xx}$  varies linearly over the cross-section and is integrated at 11 points. Every segment in the FE model contains 22 elements, except the key segments which are built up out of 5 elements. Every node of an element possesses 3 degrees of freedom subdivided in 2 translational and 1 rotational degree of freedom, figure 8.1. Bending moments are only described in one direction which results in no axial bending moments. Because axial jacks apply external forces in that direction and because of the non-parallel alignment of the segments according to figure 2.2, it is expected that bending moments are present in this direction. Because the concrete segments possess a height of 1.500 mm they

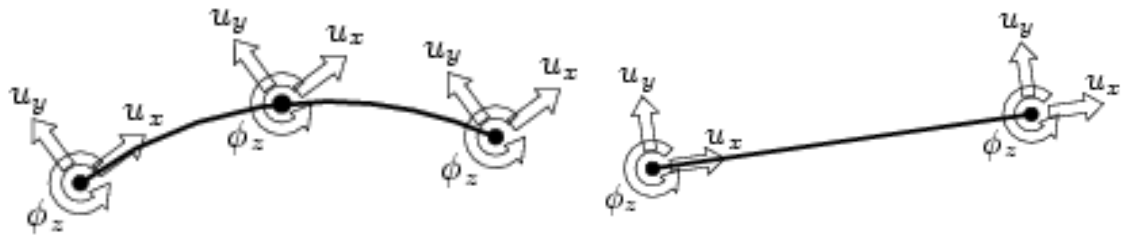


**Figure 8.1:** Degrees of freedom for CL9BE beam element (left) and L7BEN beam element (right)

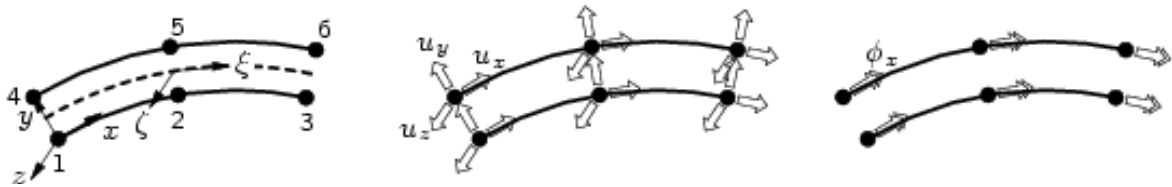


**Figure 8.2:** Topology (left), translational degrees of freedom (middle) and rotational degree of freedom (right) for a CL24I interface element

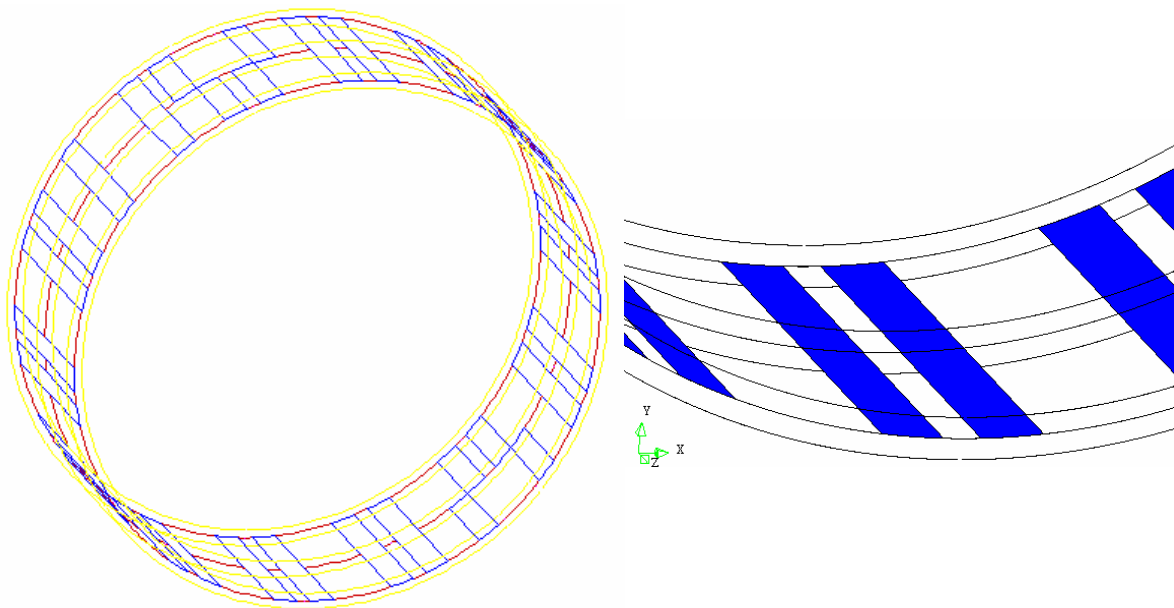


**Figure 8.3:** Schematic overview of total FE model including three tunnel rings composed of beam elements, reinforcement and ring interfaces (left) and close-up of segments and ring interfaces shown as blue areas (right)

are very stiff and because these moments are not important for studying the effects of ovalisation loads these bending moments are not incorporated in the FE model.

The joint connections are subdivided in the segment joints and ring joints. The segment joints are modelled using the Janssen concept. According to Janssen an equivalent beam with a length equal to its reduced joint height should be included. This results in a  $170\text{ mm}$  in length beam between two segments. To describe the rotational behaviour within this single element, no tensile strength is assigned to it. When exceeding the tensile strength, as a result of the occurring bending moment which cannot be compensated by the normal force, the bending stiffness is reduced and the joint opens. In the FE model an increase in the rotation is then noticed. In these joints the effect of shear or slip of the joint is not incorporated. It is thought that shear in radial direction will only have a minor influence on the ultimate load bearing capacity of the lining.

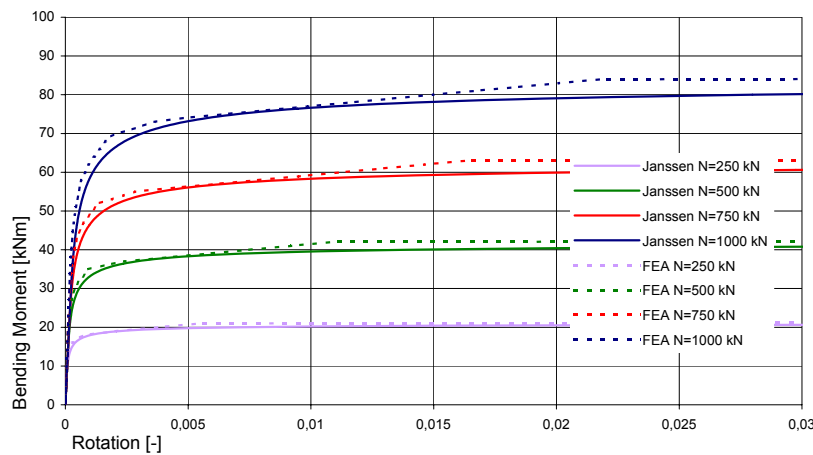


**Figure 8.4:** Theoretical bending moment-rotation behaviour according to Janssen compared to FEA calculations for different values of the normal force, using L7BEN beam elements

With 8 joints in a single ring, each possessing a length of  $170\text{ mm}$ , a large part of the circumference is occupied by the segment joints where in reality concrete segments are located. The same rotational behaviour can be modelled using a shorter element and simultaneously reducing its Young's modulus. In the used FE model a single element (**L7BEN**) with a reduced length of  $25\text{ mm}$  is implemented. For degrees of freedom see figure 8.1. The **L7BEN** element is chosen above a **CL9BE** to force joint deformations to be pure bending (no shear deformations are accounted for using **L7BEN** elements). In figure 8.4 the rotational behaviour of a single joint is compared to Janssen for different levels of the normal force. The Young's modulus is set to  $5.300\text{ N/mm}^2$  to simulate behaviour according to Janssen. Later on this Young's modulus is reduced ( $2.000\text{ N/mm}^2$ ) to account for the experimentally found lower initial stiffnesses according to figure 2.15. From the graph it is concluded that for all shown normal forces a perfect agreement with the Janssen relation is found. Therefore, this single beam element between two segments perfectly describes the rotational behaviour of a joint.

In order to investigate global lining behaviour in the ULS, the modelling of the ring joints is vital. Looking at deformations caused by ovalisation loads, only sliding of two neighbouring segments has to be modelled. When, for example, investigating the effect of the beam action of subsequent rings, the mutual rotational behaviour of adjoining rings has to be included. This can be modelled by including the compression of the plywood in axial direction. This way a gap on one side of the lining can be formed resulting in global axial bending of the lining. No such behaviour is important in assessing lining behaviour when loads do not change in axial direction, like in the full-scale experiment. In the used FE model only the tangential and radial sliding of the plywood is therefore implemented by 3 dimensional six (3+3) noded interface elements (**CL24I**), counting 3 translational and 1 rotational degree of freedom per node. Because this element is implemented in a 2 dimensional FE model, 1 rotational and 1 translational degree of freedom is restrained, both in axial direction. The material properties are as such that shear translations are uncoupled. Only in the non-linear branch, if a shear strength is implemented, this can result in a little bit higher strength than inputted. In the experiment, as well as in the FE model, every segment is connected with a neighbouring ring by four spots on each side of the segment. The dimensions of the located plywood sheets are  $150 \times 400 \text{ mm}^2$ . The beam elements which have to be connected possess a length of  $200 \text{ mm}$  and therefore two interface elements are applied per sheet of plywood. This results in  $2 \times 5$  interaction points connected per sheet of plywood, resulting in a realistic introduction of forces.

In the full-scale experiments the load on the tunnel lining is applied by hydraulic jacks. Although the force from the jacks is more evenly spread by wooden Azob plates, not an ideal line load is applied. In the FE model an ideal sinusoidal line load is applied. Translations in the axial direction of the tunnel and rotations in radial and tangential direction are restraint because it is a 2D model. Translational deformations in tangential direction for four nodes located on the quadrants of the lining are restraint in ring 1 simulating the active hydraulic supports. Ring 2 and ring 3 do not have additional boundary conditions.

### 8.1.2 Material properties of FE Model

Due to the fact that the lining is loaded until cracking of the concrete or an excessive increase in ovalisational deformations is reached, non-linear behaviour of all components in the FE model is included. To create the possibility of having cracks on an arbitrary location, the multi directional fixed crack or smeared cracking theory is implemented. The fundamental difference of smeared cracking compared to the total strain crack models is the decomposition of the total strain into an elastic strain and a crack strain. This decomposition of the strain allows for combining the decomposed crack model with for instance a plastic behaviour of the concrete in a transparent manner.

Prior to cracking the concrete is modelled isotropic and linear elastic. When the principle tensile stress is exceeded, or the tension cut-off criterion is violated by a combination of principal stresses, an orthotropic stress-strain relation is applied. The local axis system is transformed orthogonal to the principal stresses and a non-linear tension softening relation according to Hordijk et al. (1986) is applied orthogonal to the originated crack. Because the crack is fixed, principal stresses can rebuild in a direction inclined to the first crack. To reduce these shear forces a shear retention factor  $\beta$  is implemented. When using a rotating smeared crack concept no shear retention factor has to be chosen because the maximum principal tensile stress

is kept under control while it rotates. An overstiff response may be recognized when using the fixed crack concept, because of local stress rebuild in inclined directions which leads to severe stress locking on a global level. Therefore, the shear retention factor should be taken as low as possible and preferably zero to improve the fixed smeared crack results. More recent research seems to indicate that it is better to assume that the crack orientation rotates with the direction of the maximum principal stress, which means that shear stresses on the crack plane can never arise.

Because all concrete segments in the FE model are meshed to elements with a length of approximately 200 mm, the softening behaviour is more or less equal for all beams. As previously explained, this mesh is very coarse so that a more ‘heavy’ softening curve is needed to keep the same bending behaviour compared to using a fine mesh. For the compression regions the yield condition of Drucker-Prager is used which is a smooth approximation of the Mohr-Coulomb yield surface. Because the compression forces in the segments stay relatively low it is not expected that the yield criterion affects the results.

The ring joints are modelled using interface elements. Only material properties are given in the tangential and radial direction of the lining. The translations and rotations in axial direction of the lining are restraint. In the tangential and radial direction an uncoupled stress-deformation relation is given. In the first experiment an axial force of 800 kN/Jack results in a total axial force of 11.200 kN. With 4 plywood sheets per segment a resulting force of  $\frac{11.200}{7 \times 4} = 400$  kN per plywood sheet is present. If  $\mu = 0,8$  is applied a total shear force of  $400 \times 0,8 = 320$  kN per sheet can be transferred. Presuming an initial stiffness of  $10^6$  N/mm the shear strength of the sheets is reached at a displacement of  $\frac{320.000}{10^6} = 0,32$  mm. The shear strength has to be converted to a stress per square millimetre,  $\frac{320.000}{150 \times 400} = 5,33$  N/mm<sup>2</sup> and results in a stiffness of  $\frac{5,33}{0,32} = 16,67$  N/mm<sup>1</sup>. This stiffness is implemented in the FE model. If the axial force changes, like for the second experiment, another stress-displacement diagram has to be calculated. The  $\mu$ , which is based on table 2.1, has also to be reconsidered.

## 8.2 2D FE Model

A more detailed numerical model including the shear distribution over the height of the segments is obtained by using plain stress elements in stead of beam elements. Plane stress elements are characterized by the fact that the stress components perpendicular to the face are zero. These elements may only be applied if there is no bending outside the plane of the structure. Because the axial jacks are the only external forces which can cause bending moments in this axial direction the plane stress elements may be used. Advantage of this approach is that in this model the strain can vary non-linearly over the height of the concrete segments. Also the cracking of the concrete can be analysed in more detail using this approach. In the previously described beam model the interaction forces between the rings are modelled using line interfaces. A more realistic approach is achieved by applying plane interfaces. This way forces are transferred and introduced more evenly and point loads are omitted.

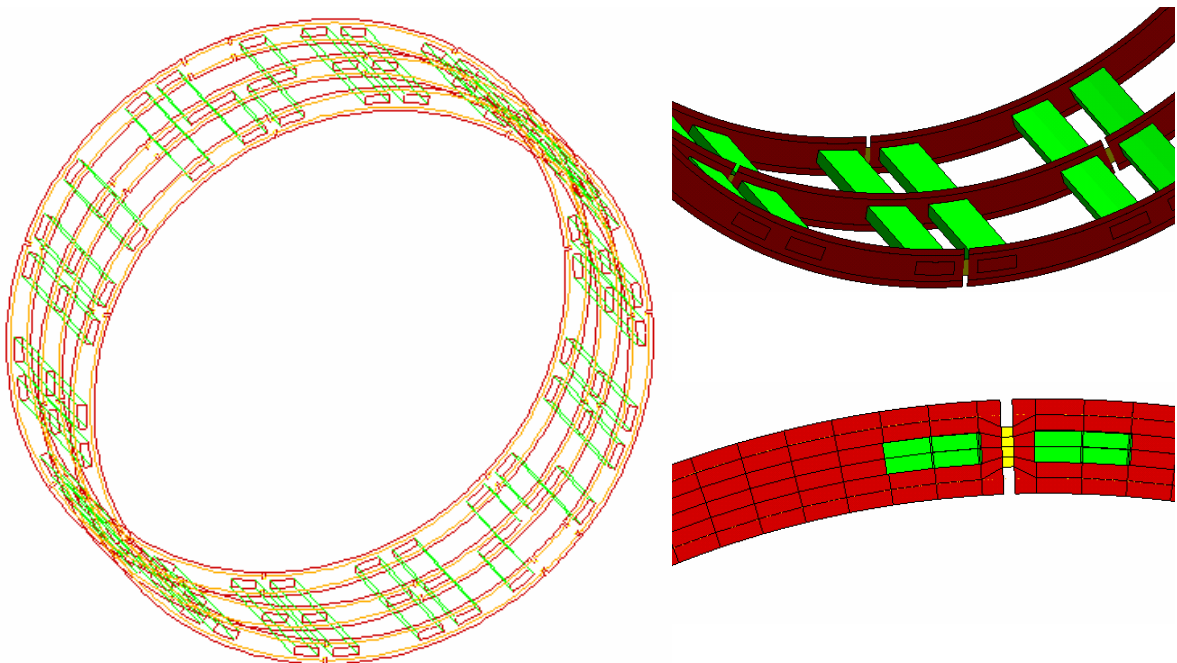


**Figure 8.5:** Schematic overview of total FE model including beam elements, reinforcement and ring interfaces (left), close-up of lining (right top) and mesh division of segments, segment interfaces and ring interfaces (right bottom)

### 8.2.1 Geometry of FE Model

The geometry is kept the same as in the experiment and the beam model. The lining is composed of three rings, each containing 5 normal segments, 2 counter segments and 1 key segment. A schematic overview of the lining is found in figure 8.5. The concrete segments are modelled using quadrilateral shell elements. This is an eight-noded quadrilateral isoparametric curved shell element. Each node accounts for translations in the global X, Y and Z directions and local rotations in the X and Y direction, represented graphically in figure 8.6.

By restraining the local translational degree of freedom in the Z direction and local rotational degrees of freedom in the X and Y direction a plane stress element is obtained. To avoid membrane and shear locking a  $2 \times 2$  integration scheme over the area is applied. Over the segmental thickness of a concrete tunnel segment, 6 plane stress elements are applied. With the mentioned integration scheme this results in 12 integrations points along the height of the segment which is one more compared to the beam elements.

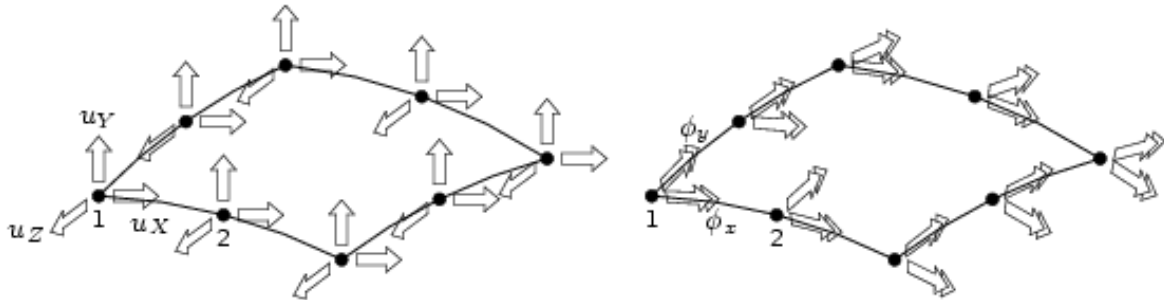


**Figure 8.6:** Translational (left) and rotational (right) degrees of freedom for a CQ40S quadrilateral shell element

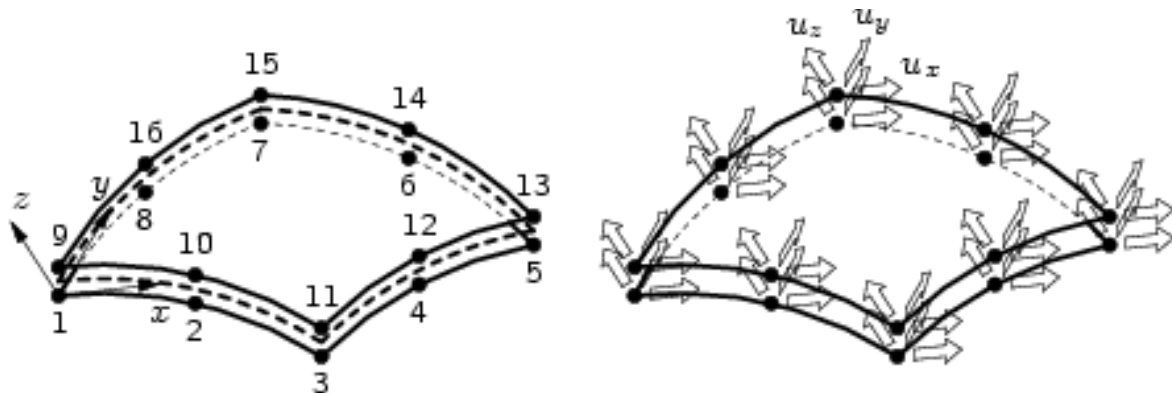


**Figure 8.7:** Topology (left) and translational degrees of freedom (right) for a CQ48I interface element

With the developed 2D plane stress model a different approach is needed for modelling the segment joints. When a single beam element is applied in this 2D model and is placed in between the middle node of one segment to the node of the connecting segment, strange local effects may introduce. A solution to this problem is to restrain the side of a segment by applying a stiff beam element over the height of the segment. A more realistic solution is to apply interface elements or distributed springs along the distance of the contact area which is the joint height  $170 \text{ mm}$ . The thickness of the joint, or the distance between the two segments, is  $50 \text{ mm}$ . By only assigning a compression stiffness to these springs, the theoretical behaviour according to Janssen is simulated. To get the exact moment-rotation relations belonging to this joint, four of the six edges are connected with four of the six edges of the connecting segment. The mesh at the edge has to be locally adjusted to get the corresponding joint height. To get a good behaviour, the edges are connected using interface elements (CL12I).

The CL12I element is an interface element between two lines in a 2D configuration, for local axes see figure 8.8. The normal stiffness is given such a value that the rotational behaviour is according to Janssen. The comparison of rotations under different normal forces between the interface element and the theory according to Janssen is shown in figure 8.9. Just like for the L7BEN elements a good agreement is found. In the complete lining model the initial stiffness is reduced to simulate experimentally found stiffnesses according to figure 2.15.

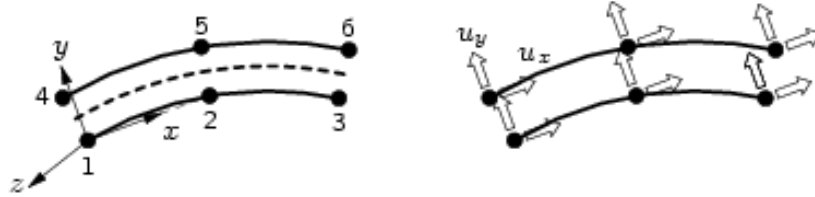


Figure 8.8: CL12I interface element, topology (left) and degrees of freedom (right)

The CL12I also has a degree of freedom in local x-axis (figure 8.8) which describes the ‘shear’ behaviour in a joint. Because this is not taken into account in the 1D beam model this is also not taken into account in this model by assigning a high stiffness in this direction. If wanted, more realistic properties can be assigned by determining the stiffness using the friction coefficient of concrete-to-concrete surface contact. The force introduction into the segments can be analysed in more detail because of the 2D character of the plane stress and the interface elements.

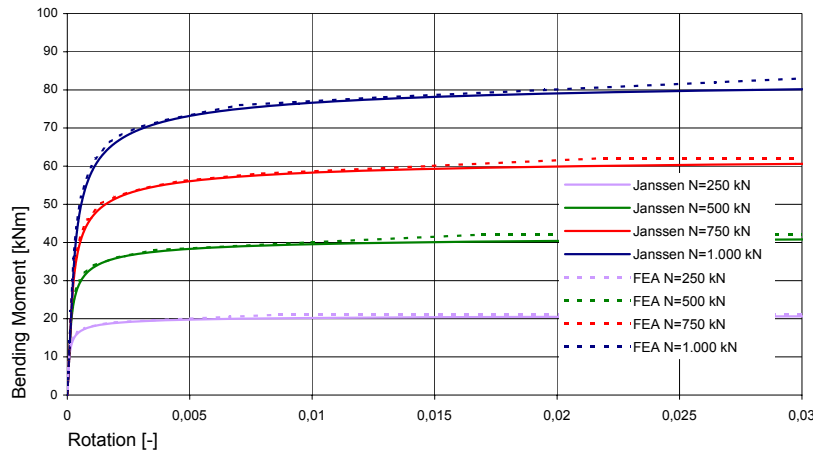


Figure 8.9: Theoretical bending moment-rotation behaviour according to Janssen compared to FE calculations for different values of the normal force, using CL12I interface elements

Modelling in two dimensions offers the possibility to model the interaction forces between the three rings more accurately. The line interface elements, as used in the beam model, can be replaced by plane interface elements. The plywood sheets used in the experiment do have dimensions of  $150 \times 400 \text{ mm}^2$ . In the FE mesh these dimensions correspond to 4 elements. Every strip of plywood is modelled using four plane quadrilateral elements (CQ48I). Every

strip of plywood is now simulated by interaction forces acting on a total of 21 nodes. The positioning of these interface elements is seen in figure 8.5. Again, just like for the CL24I interface element in the 1D model, the shear and normal direction can be given material properties. The latter one is restraint by assigning a large stiffness.

### **8.2.2 Material properties of FE Model**

More or less the same properties are assigned to this model as are assigned to the 1D beam model. The concrete is modelled exactly the same using the multi directional fixed crack concept. The material properties belonging to the interface elements are modelled somewhat differently but in the end they possess the same overall behaviour.



## Chapter 9

# Results of FE calculations

Due to the fact that the lining is slender no major differences between the 1D and the 2D FE model are expected at a global level. Some discrepancies may be noticed in the segment and ring joints because they are modelled in more detail in the 2D model. When plane sections do not remain plane or when cracking results in strange deformations, also some discrepancies may occur. To validate both models a calculation is performed using the same material parameters and the results are compared. If a good agreement is found between both models, detailed analyses can be made by using the 2D model and an influence or parameter study can be performed using the 1D model. The reason for this is the large processing time of the 2D model. When studying stresses along the height of the beam or studying the propagation of cracks, the 2D model is more attractive but normal forces and bending moments cannot be obtained very easily.

### 9.1 Comparison between the 1D and 2D FE models

First of all, the deformations of the lining in the two models are compared. This comparison is performed by implementing material properties according to Curve III as described in table 7.1. These material properties are not according to the full-scale test and are only used for performing a comparison between the 1D and the 2D model! Just like in chapter 5.2, the average maximum deformation on four points of every lining is defined for computing the deformations. In figure 9.1 the ovalisational deformation of the two FE models is compared and concluded that a very good agreement is found. The deformations match almost exactly. These deformations are larger than observed in the full-scale experiment and a lower load bearing capacity is reached. Later on in section 9.2 more accurate material properties are implemented to simulate the full-scale test.

The stress distribution along the height of the concrete segments is compared for three different load steps. The 1D FE model is constructed from beam elements which possess 11 integration points along its height whereas the 2D FE model is built up out of 6 rectangular elements each possessing integration points on two different heights, resulting in a total of 12 integration points along the height of a segment. For the 1D model the cross-sections remain plane which results in a smooth stress distribution. In the 2D model the cross-sections do not have to remain plane, caused by the fact that a cross-section is built up out of 6 rectan-

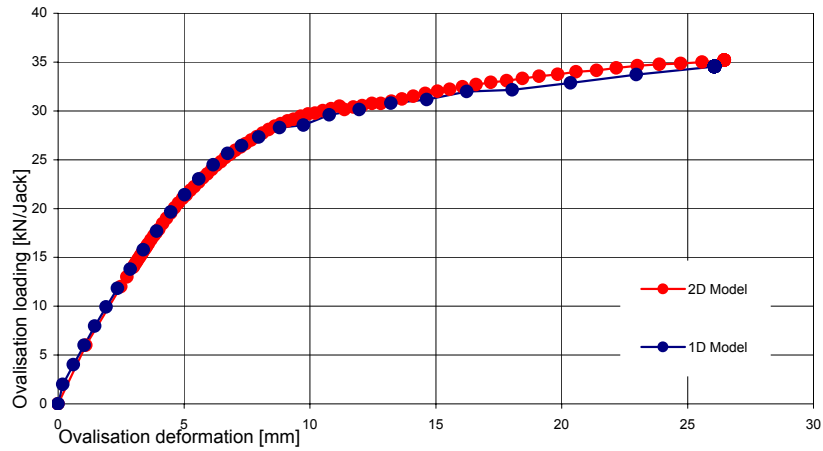


**Figure 9.1:** Comparison of FE deformations of lining between 1D model and 2D model

gular elements. In figure 9.2, the stresses obtained from the 1D and 2D FE calculations are compared. For the load at  $20\text{ kN/Jack}$  and  $25\text{ kN/Jack}$  the results show a good agreement but for the load at  $30\text{ kN/Jack}$  the 1D and 2D results show some discrepancies. Studying neighbouring cross-sections learns that especially the softening branch shows differences between neighbouring cross-sections in the same concrete segment. At  $30\text{ kN/Jack}$  the segment is heavily cracked. Some cracks are loading and some are unloading because of the initiation of new cracks and the further cracking of existing cracks. Also the height of the compression zone and the ultimate compression stress show some discrepancies at  $30\text{ kN/Jack}$ . Overall rotations over the complete segment seem to agree, so discrepancies seem to be caused by different crack patterns.

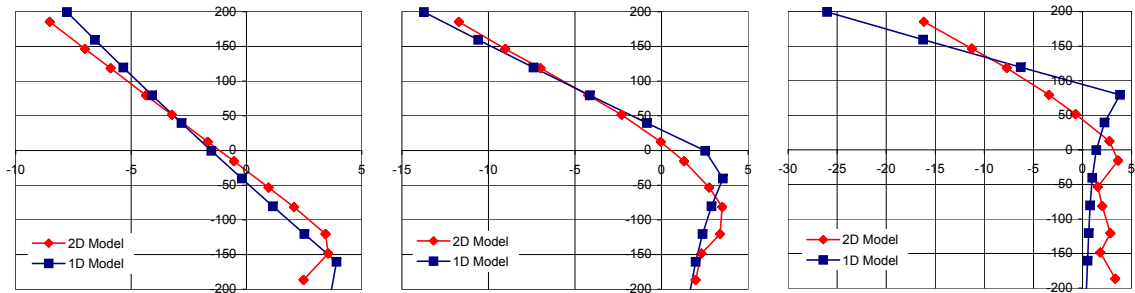


**Figure 9.2:** Stress distribution along height of beam at midpoint of segment 5 in ring 2 drawn for three different load steps (left =  $20\text{ kN/Jack}$ , middle =  $25\text{ kN/Jack}$ , right =  $30\text{ kN/Jack}$ ), comparison between 1D and 2D FE Model. Stress in  $N/mm^2$  on x-axis and distance from center line of segment in  $mm$  on y-axis

The segment joints are modelled differently in both models. In the 1D model the joints are modelled using a single beam element and the joints in the 2D model are modelled using six interface elements. In figure 9.3 the rotations of three segment joints are presented graphically. The joint in ring 1 between segment 4 and segment 5 is subject to high bending moments whereas this cross-section only contains 1 concrete segment. Therefore large rotations are

found and when comparing the rotations between the 1D and the 2D model a very good agreement is found. For the less loaded joint between segment 1 and segment 2 in the same ring a minor discrepancy is found in the non-linear branch. For the most heavily loaded joint in the middle ring again a very good agreement is found between rotation results of the 1D and 2D model.

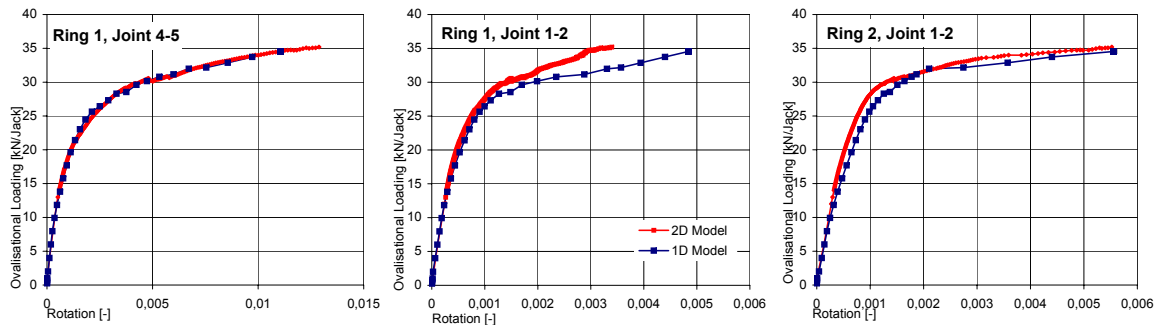


**Figure 9.3:** Rotation in segment joints calculated with 1D and 2D FE model

From the previous two paragraphs it may be concluded that the behaviour of the tunnel lining in both models is almost similar. The only thing left to check are the locations where cracks initiate and how they develop in both models. In both models the element length is exactly the same from which it may be expected that cracks initiate in the same segment and at a similar location. When the ovalisation load is increased, some discrepancies might be noticed due to the fact that cross-sections remain plane in the 1D model contrarily to the 2D model. The 2D model may better describe the development of cracks when they stay close to the surface.

The first cracks start to initiate at an ovalisation load of  $17 \text{ kN/Jack}$ . This occurs in both models at the same load in the same segment, namely segment 5 in ring 2. Both show five minor cracks. When increasing the load, more cracks start to initiate and existing cracks develop. The following segments in which cracks arise are segment 3 and segment 7 in ring 2 at an ovalisation load of  $19,5 \text{ kN/Jack}$  in the 1D model. In the 2D model these two segments start to crack at an ovalisation load of  $21,5 \text{ kN/Jack}$ . Increasing load even further results in the initiation of cracks in more segments and rings. Both models indicate the location of cracks in the same segments. In figure 9.4 all cracks in ring 2 at an ovalisation load of  $30 \text{ kN/Jack}$  are represented graphically. Both models show cracks located in the same segments but the number and depth of the cracks differ. More cracks are found in the 1D model and more of those are propagated deeper into the segments compared to the 2D model. This can be explained by the fact that plane sections remain plane in the beam model whereas this is not the case in the plane stress model composed of 6 elements along the height of a segment. Because the 1D model shows more cracks, the crack widths of single cracks are less compared to cracks in the 2D model. This results in more or less similar deformations when looking at a whole segment. This is also confirmed by the fact that ovalisation deformations are equal just like rotations in the joints which implies that deformations in the segment should also be more or less equal.

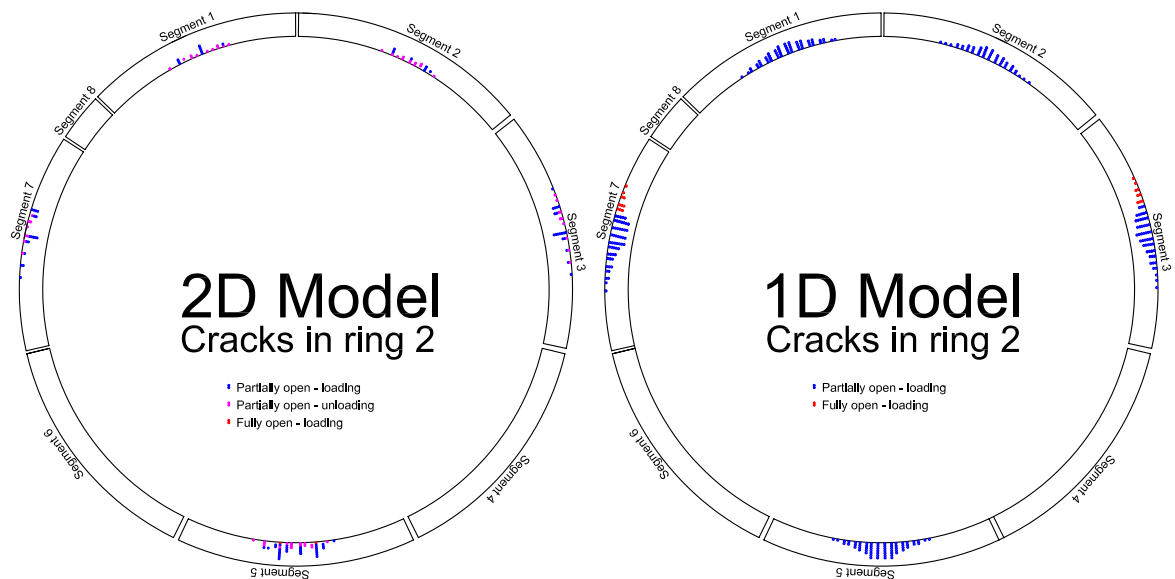


**Figure 9.4:** Cracking in segments in ring 2 at an ovalisation load of  $30 \text{ kN}/\text{Jack}$ , material properties not in accordance with full-scale experiment, just a comparison between the 1D and 2D FE model with material properties according to curve III

The development of cracks seem to be more realistically presented by the 2D model. The deeper cracks are not as closely spaced as in the 1D model. In segment 5 of ring 2 in the 2D model this is clearly shown by the unloading of cracks in the neighbouring cross-sections of a deep developed crack. Of some deeper developed cracks the neighbouring cross-sections do not even show cracking in contrast to the 1D model. In the beam model a number of deep cracks are closely spaced and no unloading of neighbouring cross-sections is shown. This is also shown in figure 9.5 in which the crack strains in the middle section of segment 5 of ring 2 are shown for three different load steps. In these last analysis it is emphasised that the development of cracks in both models cannot be modelled very accurately because of the relatively course mesh as explained in chapter 7.2. By refining the mesh the propagation of cracks may give even more realistic results. In the previous analysis a comparison between the 1D and the 2D model with the same element length is given and upon that it may be concluded that even with this course mesh the 2D model give more realistic results regarding the initiation and propagation of cracks.

The results of FE calculations with 1D beam elements and 2D plane stress elements were compared in this paragraph. From the results it is concluded that the 1D model gives more or less the same results as the more advanced 2D model. Even though the propagation of cracks shows some differences between both models it may be concluded that the global behaviour of the tunnel lining is the same in both models. Because of the very low computation time and the ability to analyse structural behaviour more easily the 1D beam model is used from now on. Only for studying cracks and comparing the location and spacing of cracks both models are used.

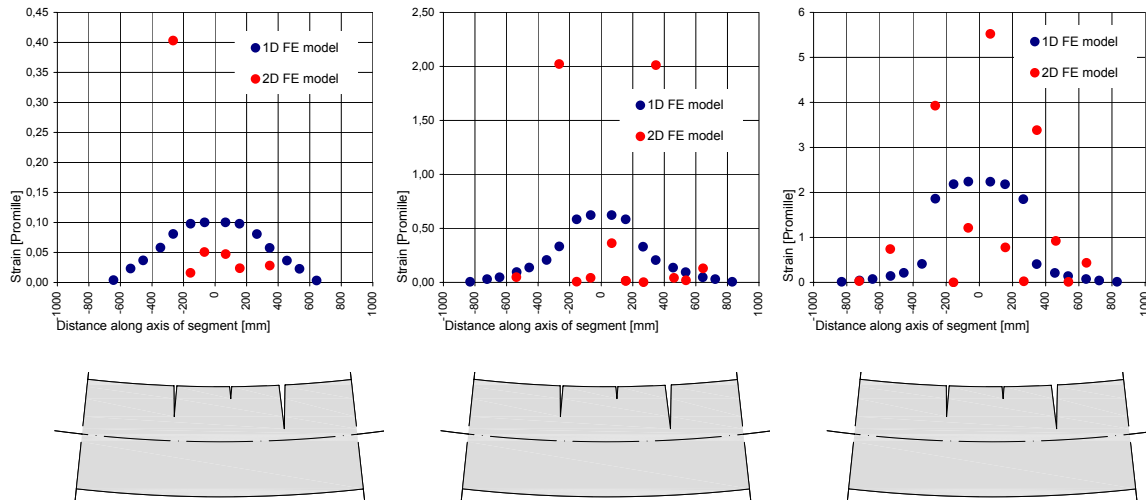


**Figure 9.5:** Crack strain in outer fibres in critical segment of middle ring in 1D and 2D FE model at 10 kN/Jack (left), 25 kN/Jack (middle) and 30 kN/Jack (right), material properties not in accordance with full-scale experiment

## 9.2 Results of 1D FE analysis compared to experimental results of C01

### 9.2.1 External deformations

The results of the FE analysis are used to be able to better understand the structural behaviour of the tunnel lining under ULS conditions. As explained in the previous section, calculations are performed using the 1D FE model. Before going into detail about the structural behaviour of the lining in the ULS, the deformations found in the experiment and with the FE calculations are compared. For this comparison the deformations on the four points of the lining are used as previously discussed in chapter 5.1. Experiment C01 is simulated first. At the end of this experiment some segments started to crack resulting in changing material properties. If the first experiment can be simulated well the lining in the model should be damaged. This damaged lining is used as input for the simulation of the second experiment, C02.

The FE model as elucidated in chapter 8 is used to simulate both experiments. Four simulations are performed in which the different material properties, according to figure 7.13, are implemented. The segment joint stiffness is reduced to 38% in order to simulate the bending behaviour as found during experiments, see figure 2.15. The stiffness of the ring joints is set to  $10^6$  N/mm and equals experimental obtained stiffnesses. The calculation shows for all four curves reliable results until the peak bending moment, according to figure 7.13, in a certain segment is reached. Beyond this curvature the model starts to show unreliable results like the dramatic increase or decrease of normal forces in the segments. At the end of the full-scale experiment it was noticed that the reinforcement in some of the segments more or less reached the yield strength but dramatic yielding was not taking place. The calculations will therefore be stopped the moment the reinforcement steel possesses a plastic strain of 0,875%.

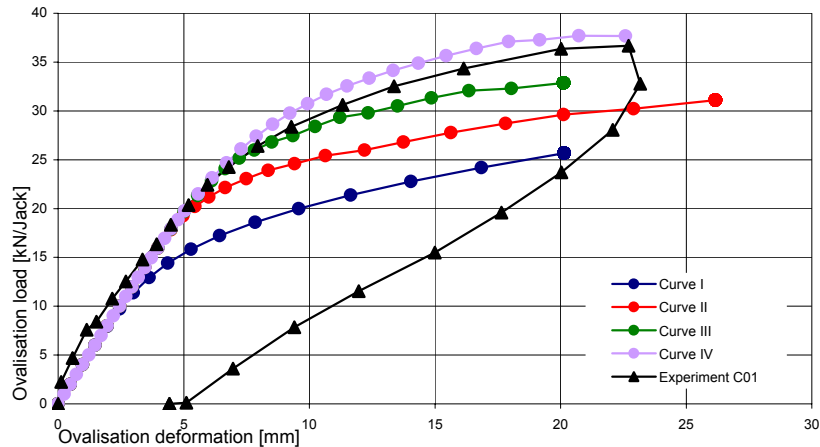


**Figure 9.6:** FE deformations of lining calculated with the four different bending moment-curvature relations compared to experimentally obtained deformations

The material properties of the concrete segments belonging to curve I, figure 7.13, are implemented in the complete lining model. Curve I is based on a tensile strength of  $0 \text{ N/mm}^2$ . It is expected that this results in a very weak behaviour resulting in larger deformations compared to experimentally obtained deformations. This expectation is confirmed by figure 9.6. The transition point between the linear and the non-linear branch is reached at a load of  $15 \text{ kN/Jack}$  whereas this point in the experiment is reached at  $20 \text{ kN/Jack}$ . The non-linear branch shows a too weak behaviour, whereas the rotations in the segment joints agree very well with experimentally obtained data. Using material properties belonging to curve II, compared to the experiment better results are obtained and deformations are also presented in figure 9.6. Deformations are still larger compared to the experiment but the transition point between the linear and the non-linear branch seems to agree quite well. Again, the non-linear branch shows a too weak behaviour. The concrete in curve II is given a tensile strength of  $4 \text{ N/mm}^2$  and a small fracture energy. The obtained deformations will therefore be a reliable lower limit with deformations more close to reality, compared to curve I.

Deformations of the lining, using material properties belonging to curve III and curve IV, seems to approach experimentally obtained data more closely. Curve IV even overestimates the load bearing capacity of the lining. As already expected in chapter 7.2, the softening behaviour of the concrete affects global lining behaviour dramatically. From figure 9.6 it may be concluded that the softening properties of the concrete lay somewhere in between curve III and curve IV. In the next paragraph this is proved by investigating the behaviour of the concrete segments in more detail.

### 9.2.2 Compression strains

During the experiment not only displacements of the lining are obtained but also strains on the concrete segments. By comparing measured strains to output strains from FE calculations the concrete behaviour is analysed in more detail. The compression strain on the most

heavily loaded segment in ring 2 is compared with the FE results, see figure 9.7. It is seen that the point where the linear branch ends and the non-linear branch starts is equal for experimental strains and curve II, III and IV of the calculations. This transition point implies that the tensile strength of the concrete is reached on the outer fibre. Therefore, the strains from curve I start to increase earlier due to the fact that no tensile strength is assigned to the material. The difference between curves II, III and IV is the rate at which the strains are increasing. The compression strain in curve II and III increases more rapidly compared to the experimental strains.

A too rapid increase in strains may indicate that the softening curve is too weak. If the concrete cannot take more tensile forces the curvature increases and the reinforcement takes over tensile forces, the concrete compression zone decreases resulting in a larger compression strain at the outer fibre. When comparing the calculation results with the experimentally obtained data, it is found that only material properties belonging to curve IV seem to agree. The other three curves indicate that the tension softening curve may be too weak.

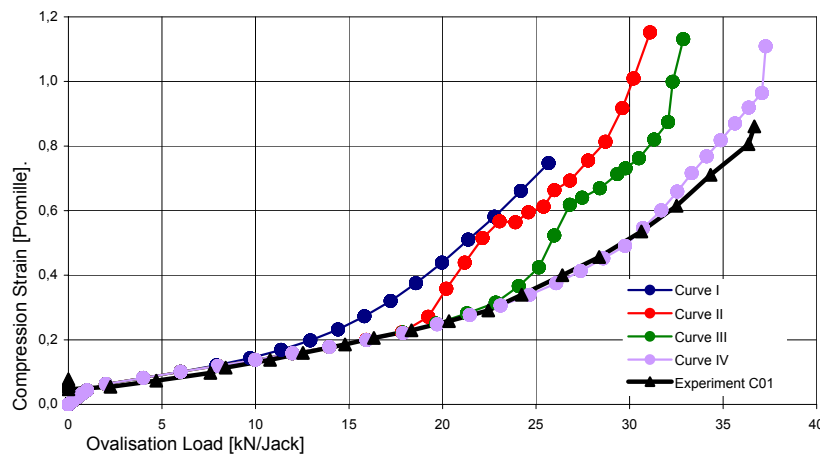


**Figure 9.7:** Compression strain in outer fibre of heavily loaded segment in ring 2, comparison between FE calculations and experimental data

From this paragraph it becomes clear that the tensile properties of the concrete have a strong effect on global lining behaviour just like expected in chapter 7.2. Four different tensile properties are used in calculating deformations and very good results are obtained for certain tensile parameters. Also the strains and curvatures in the elements seem to agree very well with experimental data.

The ‘correct’ properties of the concrete and the bending moment-curvature relations are not known for sure, but with this analysis it is very likely that the properties of the concrete lay somewhere in between curve III and curve IV.

### 9.2.3 Segment joint rotations

In the previous section, global displacements and concrete compression strains seemed to agree well with experimental data. In chapter 5.2 an analysis of experimental data was described leading to a detailed overview of deformations. Deformations were subdivided into total deformations and deformations due to joint rotations. The same analyses are performed using data obtained from the FE calculations. In figure 9.8 a comparison is shown for ring 1 and ring 2. Results of all three rings are given in appendix F. The total deformations as well as the deformations only due to joint rotations show a perfect agreement, especially for ring 1. Deformations due to joint rotations in ring 2 seem to show some discrepancies in the non-linear branch.

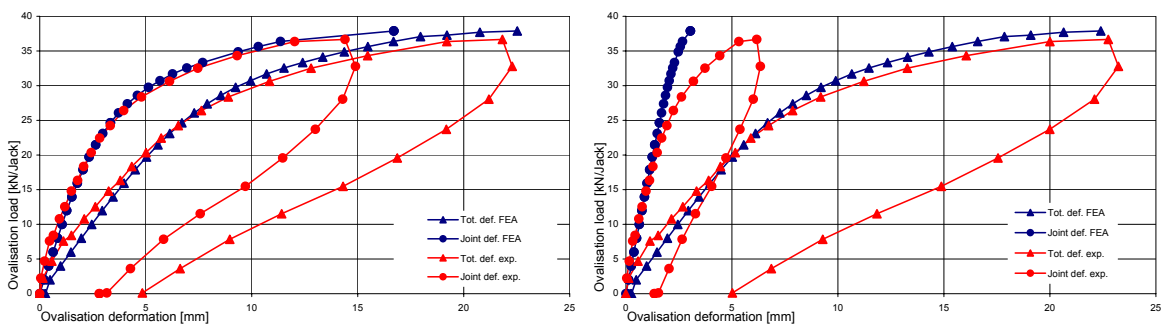


**Figure 9.8:** Total deformations of lining and deformations based on joint rotations, FE results compared to experimental data, ring 1 (left) and ring 2 (right)

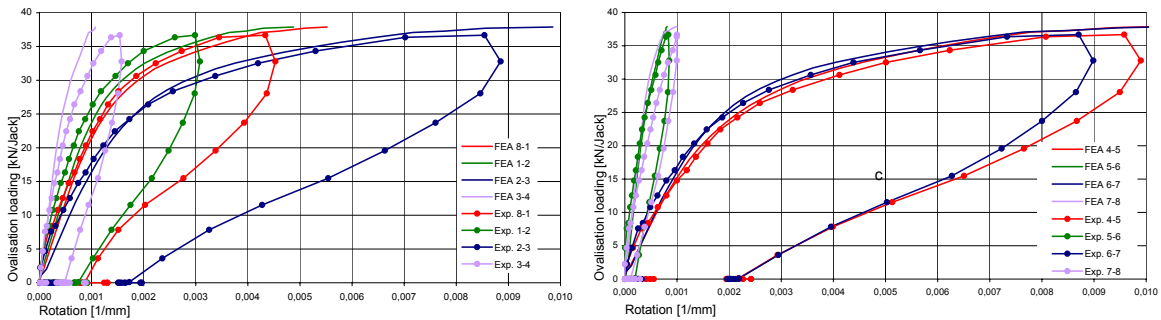


**Figure 9.9:** Rotations in joints in ring 1, FE results compared to experimental data

The presented total deformations and deformations due to joint rotations (figure 9.8) show a good agreement but are calculated using very much data points. The deformations do not tell anything about the accuracy of the FE model at joint level. Therefore, the joint rotations in ring 1 are given separately and plotted versus the ovalisation load in figure 9.9. In the left graph, rotations of joint 8-1 to 3-4 are given and in the right graph joint rotations in joints 4-5 to 7-8 are given. In appendix F the same results are presented for ring 2 and ring 3. From the graphs shown it is concluded that also on a more detailed level the FE model shows very good results compared to experimental data.

### 9.2.4 Additional capacity of segment joints

To apply the axial force on the lining, 14 hydraulic jacks are installed on top of the upper ring. Between a jack and a concrete segment a steel plate is installed to introduce the force in a more spread manner. The bottom ring is also provided with such plates which act as a support. Some of these plates are located just above or below a segment joint and affect the rotational behaviour of the joint by transferring additional bending moments. In Vervuurt and Den Uijl (2006) this additional capacity is estimated to be within the  $15 \text{ kNm}$  and  $50 \text{ kNm}$  per segment joint in experiment C01. Due to the low axial force applied in C02 it is expected that the additional joint capacity is negligible small and may be disregarded when simulation the second experiment.

The additional joint capacity directly affects the load bearing capacity of the lining in the first experiment. To investigate this effect the steel plates are included in the 1D FE model by adding rotating springs in between the segments in ring 1 and ring 3. These springs are given a bi-linear bending moment-rotation diagram, from which the horizontal plateau equals the additional bending moment capacity. The initial stiffness is set equal to the initial stiffness of the segment joints which is a third of the theoretical derived stiffness according to Janssen. Most heavily rotating segment joints now possess a bending moment capacity which is  $15 \text{ kNm}$  or  $50 \text{ kNm}$  greater just before maximum load capacity of the complete lining is reached.

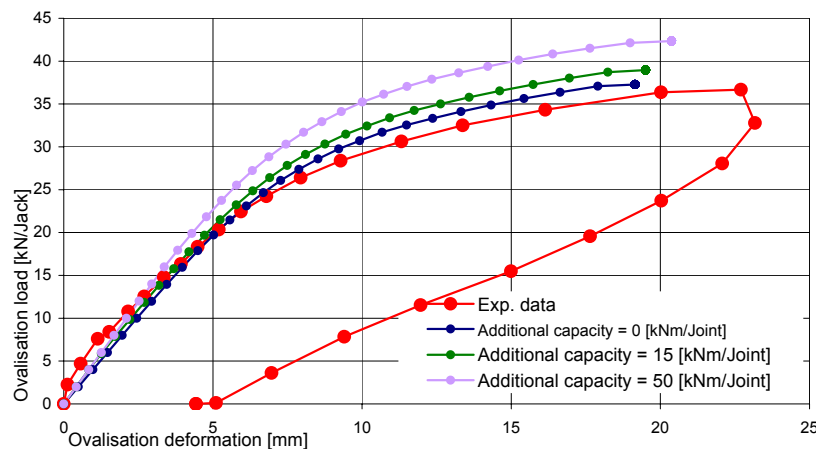


**Figure 9.10:** Ovalisation deformations of lining with additional segment joint capacity

To study the effect of the steel plates on the bearing capacity, two calculations are performed in which the springs are given an additional bending moment capacity of  $15 \text{ kNm}$  and  $50 \text{ kNm}$ . The results of these calculations are shown in figure 9.10. In this figure, the deformations of the lining are compared to a lining without additional capacity. Just as expected, the bearing capacity of the lining is increased. For the FE model which is given an additional capacity of  $50 \text{ kNm}$  per segment joint an increase of  $5,1 \text{ kN/Jack}$  in load bearing capacity is achieved. The increased load bearing capacity of the lining can also be calculated manually. The critical cross-section contains two segment joints. Every segment joint is able to take  $50 \text{ kNm}$  which results in an additional  $100 \text{ kNm}$  bending capacity. With equation 9.1 the

additional load bearing capacity of the complete lining is calculated to be  $4,9 \text{ kN/Jack}$  which is close to results of the FE analysis.

$$M_{cross-section} = 1/3 \times r^2 \times q \times \cos(2\theta)$$

$$100 = 1/3 \times 4,525^2 \times q \times \cos(2 \times -0.50\pi) \Rightarrow q = 4,9 \quad (9.1)$$

By adding additional capacity to the segment joints, the deformations of the lining are reduced and the ultimate load bearing capacity is increased. This is of course only achieved by reducing rotations in the joints. In figure 9.11 the deformations due to joint rotations for ring 1 and ring 2 are compared to experimental values. It is seen that joint rotations in ring 1 are heavily reduced by the steel plates whereas no effect on joint rotations in ring 2 is noticed. From the left graph it may be concluded the FE model without the incorporation of steel plates is most close to reality. At least this model predicts joint rotations more close to experimental values which indicates that the total stiffness of a segment joint is correct. The total stiffness of a segment joint in ring 1 and ring 3 is a combination of the real joint stiffness and the additional steel plates. This leads to the possibility that the real joint stiffness was much lower than implemented in the FE model whereas the additional steel plates delivered some additional stiffness. The relationship between both stiffnesses is hard to determine with the obtained data from the experiment. The only clue can be found when investigating differences between ring 1/3 including steel plates, and ring 2 without additional steel plates.

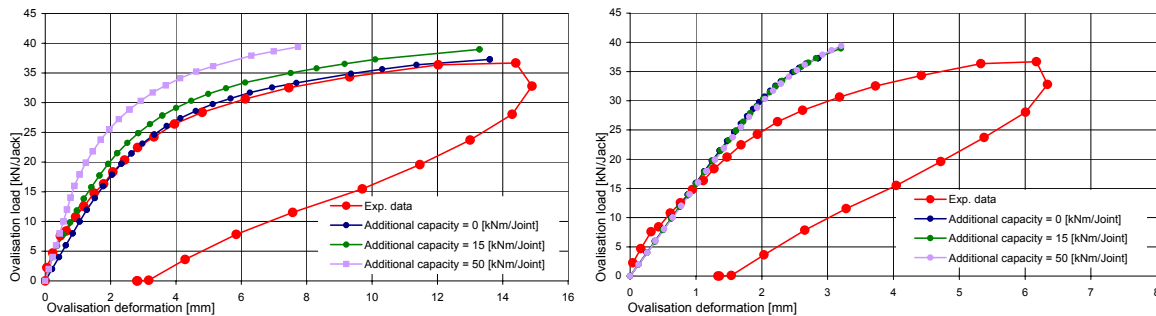


**Figure 9.11:** Deformations caused by joint rotations in ring 1 (left) and ring 2 (right), results of FEA compared to experimental obtained joint rotations

Joint rotations in ring 2 show a too stiff response, compared to experimental found rotations, whereas rotations in ring 1 and ring 3 show realistic rotations. This may be an indication that the estimated joint stiffness is too high. When reducing the joint stiffness the rotations in ring 2 should be more close to reality whereas the rotations in ring 1 and ring 3 are kept the same by adding stiffness coming from the additional steel plates. When looking at the rotations in ring 2 it is concluded that in the non-linear branch the joint rotations are too stiff whereas rotations in ring 1 show good results when no additional steel plates are implemented. So by reducing the joint stiffness and adding some additional joint stiffness in ring 1 and ring 3 it was tried to approach reality, especially joint rotations in ring 2, more closely. Nevertheless, FE calculations showed that joint rotations in ring 2 do not approach reality more closely when reducing joint stiffnesses. Final conclusion is that the overall joint stiffness is estimates correctly, but it is unknown what proportion is caused by the joint and what is caused by the

additional steel plates, but it is estimated that the influence of the additional steel plates is very small.

### 9.2.5 Cracking pattern

At the end of experiment C01 and C02 the lining was observed in detail and the locations of new developed cracks were drawn on a map. This map is shown in figure 9.12. In this figure the situation of the lining at the end of both experiments is shown graphically. Difference is made between cracks which were already present, cracks which were partially developed and cracks which were fully developed over a segment. From the FE calculations the location of cracks is also obtained. Due to the fact that a relatively course mesh is used with respect to crack initiation and propagation, not the existence of every crack is drawn, but the area in which elements are cracked.

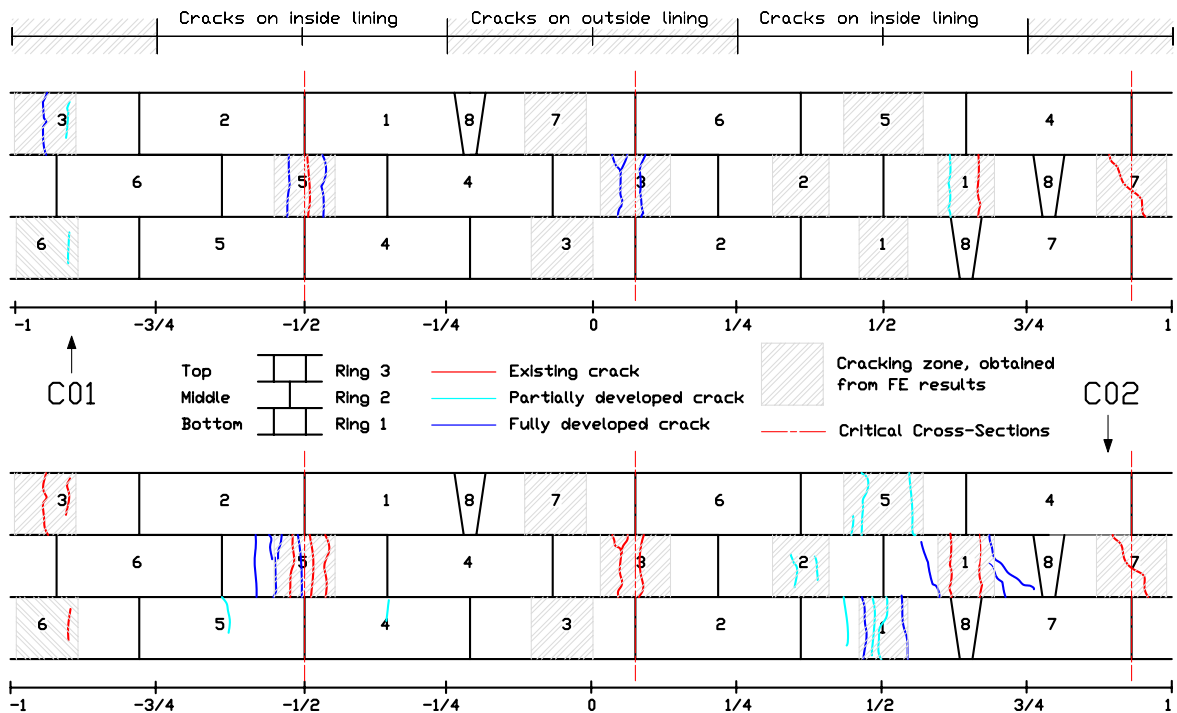


**Figure 9.12:** Cracking pattern observed during full-scale experiments compared to FE results, concrete properties in FEA according to Curve IV

In the figure on top, the comparison between experiment C01 and the belonging FE analysis is presented. At first sight, a good agreement between the FE analysis and the experiment is obtained. Although the FE calculations show more areas in which elements are cracked, the observed locations at the end of the experiment are predicted correctly. Five areas are present in which the FE calculation predicts cracking whereas no cracks are observed at the end of the experiment. This may be explained by the fact that these cracks are not observed, because they were too small to detect, or because the FE model was loaded more heavily or

because the assigned segment properties were too weak. The cross-sections located at  $-0,07 \pi$  (outside lining) and  $+0,50 \pi$  (inside lining) for example, are heavily loaded but no cracks are observed at the end of the experiment. During the second experiment the ovalisation load, which causes the bending moments, is also present and initiates new cracks. When comparing the by FE analysis found cracking pattern with the situation of the lining at the end of the second experiment a better agreement is found. The cross-section located at  $+0,50 \pi$  showed some severe cracks at the end of the second experiment just like predicted by the FE model, but still no cracks are present at  $-0,07 \pi$ . A possible explanation is that deformations did localize at cross-section  $+0,07 \pi$ , instead of at  $-0,07 \pi$  what is predicted by the FE calculation. Because cracks should occur at the outside of the lining the force introduction via Azob plates might have had some influence on the initiation of cracks.

## Chapter 10

# Structural behaviour of the lining

Based on results presented in the previous chapter it may be concluded that a reliable FE model is developed. Comparisons of deformations and compression strains between experimental data, 1D and 2D FE models showed a very good agreement. With the aid of the 1D FE model the structural behaviour of the tunnel lining is further analysed. The interaction forces in the plywood or the rotations in the joints are investigated in detail. First of all the global lining behaviour is studied. Most important aspect in the global lining behaviour is the distribution of bending moments. How bending moments are distributed and how they affect the load bearing capacity is treated in the following section.

### 10.1 Experiment C01

#### 10.1.1 Redistribution of bending moments

The lining in the experiment is loaded in an axial and a radial direction from which the latter one is subdivided into an uniform and an ovalisation part. The axial and the uniform radial force mainly causes normal forces in the concrete which the lining can take very well in contrast to an ovalisation load. A relatively small ovalisation load causes severe deformations of the lining. Differences in bending stiffnesses in the concrete segments and the joints leads to a redistribution of bending moments. Especially when the capacity of a segment joint is reached the redistribution of bending moments may be significant.

Because the three rings are subsequently coupled at the ring joints through plywood sheets, the bending moment at the location of a segment joint is partially transferred in axial direction to neighbouring concrete segments. Another possibility is that bending moments are partially redistributed in the ring itself which affects global lining behaviour. It is expected that bending moments are redistributed in both directions. In the following sections the redistribution of bending moments is investigated and especially its effect on the maximum load bearing capacity of the lining.

#### **Redistribution of bending moments in axial direction**

The axial force on the lining squeezes the plywood in between the concrete segments. Via these plywood sheets bending moments are partially transferred in axial direction to neighbouring segments. In figure 10.1 the bending moments in the separate rings are shown and

compared to analytical values. The analytical bending moments are based on a continuous lining subject to an equal ovalisation load. The location of the segment joints in the rings is given in the same graphs to analyse their effect on the distribution of bending moments. From both graphs it is concluded that bending moments are minimal at the location of a joint and maximal in the middle of a segment. This increase in bending moments at the middle of a segment is more severe for segments in ring 2 than for segments in ring 1 and ring 3.

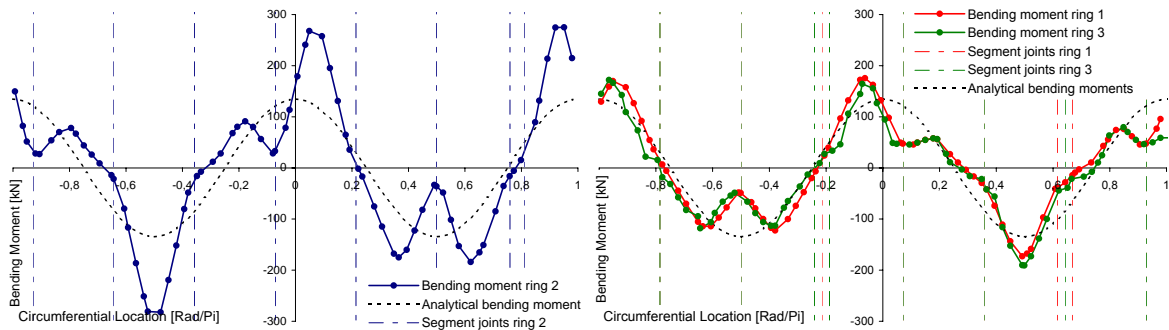


**Figure 10.1:** Bending moment in ring 2 (left) and in ring 1 and ring 3 (right) at an ovalisation load of  $20 \text{ kN/Jack}$

Bending moments in ring 1 and ring 3, at a cross-section located at a joint, are both transferred to the same segment in ring 2. This leads to a severe increase of bending moments in the segments of ring 2 and is clearly confirmed by the left graph in figure 10.1. Bending moments in the middle of a segment are much larger compared to analytical values. At the location of the joints in this middle ring the bending moments are lower and are transferred to ring 1 and ring 3. At these cross-sections only one joint is present over the whole cross-section from which bending moments are transferred to two neighbouring segments. This only leads to a slight increase of bending moments in ring 1 and ring 3, clearly confirmed by the right graph in figure 10.1.

As mentioned earlier, ring 2 is the most heavily loaded ring. In the figure above the critical cross-sections at  $-0,50$ ,  $+0,07$  and  $+0,93 \pi$  are easily recognized. At these sections the curvatures are large, especially when cracks start to initiate and eventually plastic hinges are formed. At higher loads, bending moments cannot be transferred to neighbouring segments leading to a redistribution of forces in the ring itself.

### Redistribution of bending moments in circumferential direction

The existence of relatively weak joints in between segments results in a non-uniform bending stiffness along the circumference of the lining. Therefore, redistribution of bending moments occurs from the beginning of loading. At a relatively low ovalisation load the segment joints reach their capacity amplifying the redistribution of bending moments. Major changes in the global behaviour of the lining are expected when the concrete segments start to crack. Stiffnesses decreases dramatically leading to more redistribution.

In figure 10.2 the bending moments in the segmented lining are compared with analytically determined bending moments in a continuous lining. The difference between both lines is an

indication for the degree of redistribution in circumferential direction. The presented bending moments are plotted as a function of the circumferential angle and are the sum of the bending moments in the three separate rings. For certain cross-sections that are the bending moments in three neighbouring segments whereas in other cross-sections this is a combination of bending moments in joints and segments. The results are based on calculations belonging to concrete properties of curve IV.

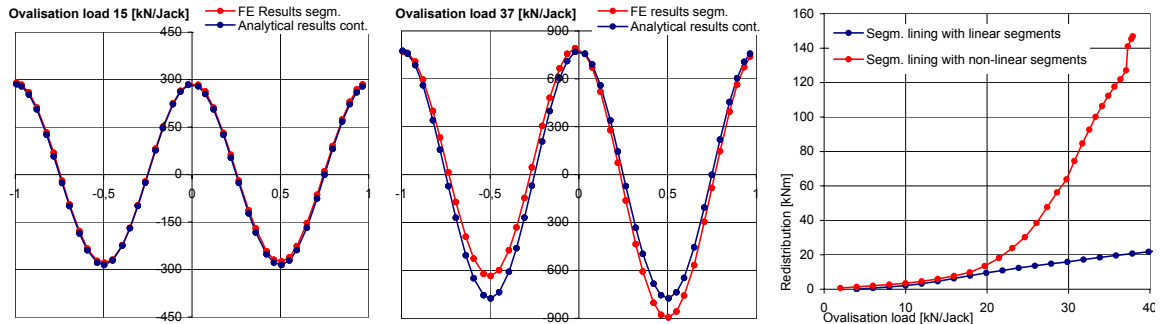


**Figure 10.2:** Redistribution of bending moments in circumferential direction (left and middle) and as a function of the ovalisation load (right)

From the figure above it is concluded that at an ovalisation load of  $15 \text{ kN/Jack}$  almost no differences between the bending moments based on a continuous lining and the segmented lining are noticed. The comparison shown in the middle graph is taken at an ovalisation load of  $37 \text{ kN/Jack}$  in which redistribution in circumferential direction is noticed. At the critical cross-section located at  $-0,50 \pi$  the bending moments are less than analytically expected whereas bending moments at  $+0,50 \pi$  are larger. From these observations it is already concluded that redistribution does occur at higher loading conditions. The difference between the bending moment in cross-sections  $+0,50 \pi$  and  $-0,50 \pi$  is almost  $300 \text{ kNm}$ .

The bending moment in the critical cross-section is subtracted from the analytical expected bending moment and plotted versus the ovalisation load to investigate the redistribution in more detail, right graph in figure 10.2. Even at low ovalisation loads the bending moments in the cross-section do not match analytical values and a linear increase in redistributions is noticed. This is due to the fact that this is a relatively weak cross-section and the joints already reached the non-linear branch. At  $17 \text{ kN/Jack}$  a rapid increase in the redistribution of bending moments is noticed. From that moment on the stiffness of the cross-section is reduced significantly by the cracking of the concrete.

The blue line in the right graph of figure 10.2 represents the difference in bending moments between a segmented and a continuous lining obtained with the same FE model, but calculated using linear concrete properties. This line also shows a linear increase in redistributed bending moments as the ovalisation load increases. The rapid increase at  $17 \text{ kN/Jack}$  is not noticed in this curve leading to the conclusion that at  $17 \text{ kN/Jack}$  the cracking of the concrete is responsible for the severe redistribution of bending moments. At maximal ovalisation load  $140 \text{ kNm}$  is redistributed in circumferential direction.

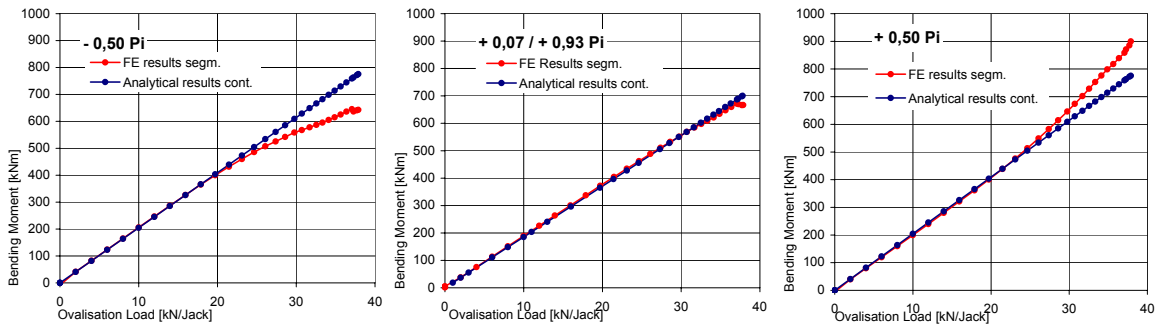


**Figure 10.3:** Redistribution of bending moments in three different cross-sections

The second most critical cross-sections are located at  $+0,07 \pi$  and  $+0,93 \pi$ , which also contain one segment and two joints. It seems from figure 10.2 that bending moments in these two cross-section more or less equal analytical values and are not affected by redistributions. In figure 10.3 the bending moments from three different cross-sections are plotted and compared to analytical values. This figure again confirms the redistribution of bending moments in the critical cross-section at  $-0,50 \pi$  as well as the fact that bending moments at  $+0,07 \pi$  and  $+0,93 \pi$  are not affected by redistributions. In the cross-section at  $+0,50 \pi$  an increase in bending moments is noticed.

### 10.1.2 Increase of normal force

In the previous section it was seen that by a redistribution of bending moments the load capacity of the entire lining is increased. Another increase in load capacity is achieved by an increase of the normal force in certain concrete segments. Before applying the ovalisation load onto the lining an equal normal force is present in all three rings. When increasing ovalisation load it is noticed that normal forces are transferred to neighbouring rings. In figure 10.4 the normal force in the three rings at an ovalisation load of  $37 \text{ kN/Jack}$  is presented graphically. From the left graph it is concluded that normal forces in the middle ring are much higher than normal forces in the top and bottom ring. Especially in the segments at the three critical cross-sections the normal force is much higher whereas the normal force in the neighbouring joints is reduced. Because the increase in bending capacity of the concrete segment is more than the decrease in capacity of the segment joints this transfer of normal forces is advantages concerning the global load bearing capacity.

$$N_{ovalisation} = -1/3 \times q \times r \times \cos(2\theta) \quad (10.1)$$

When taking the sum of the normal forces in all three rings, a small redistribution of normal forces in circumferential direction is noticed. In the critical cross-section at  $-0,50 \pi$  the normal force is somewhat lower and at  $+0,50 \pi$  the normal force is somewhat larger than analytically expected. In figure 10.4 the normal force of segment 5 of ring 2 is plotted versus the ovalisation load. As the ovalisation load is increased the normal force starts to decrease. This is exactly what is expected according to equation 10.1. This equation says that increasing an ovalisation load increases normal forces at  $0,00 \pi$  and  $+1,00 \pi$  whereas normal forces at  $-0,50 \pi$  and  $+0,50 \pi$  decrease. Beyond an ovalisation load of  $25 \text{ kN/Jack}$  normal forces start to grow in this segment reaching  $1.400 \text{ kN}$ . Just before collapse normal forces increase very rapidly.

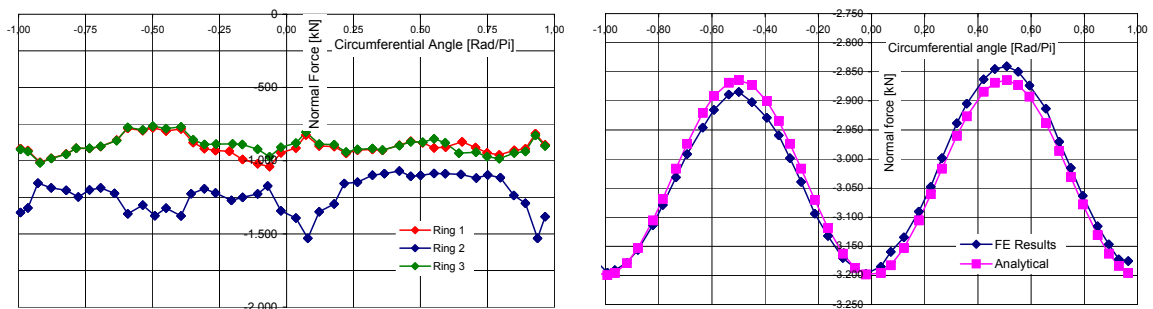


**Figure 10.4:** Normal force in lining at an ovalisation load of  $37 \text{ kN/Jack}$  per separate ring (left) and sum of three rings compared to analytical values (right)

The influence of an increase in normal force on the bending capacity of a single segment is illustrated in figure 10.5. From this graph it is concluded that a normal force of  $1.500 \text{ kN}$  results in a bending capacity of a concrete segment of  $550 \text{ kNm}$  which is an increase of  $80 \text{ kNm}$  when only a normal force of  $1.000 \text{ kN}$  is present. In the critical cross-section at  $-0,50 \pi$  the normal force is  $1.375 \text{ kN}$  which results in a bending capacity of  $532 \text{ kNm}$ , an increase of  $62 \text{ kNm}$ .

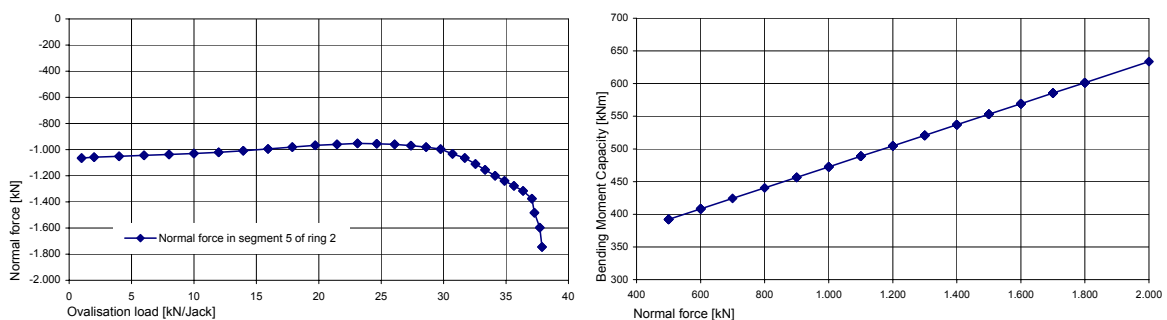


**Figure 10.5:** Normal force in segment located at critical cross-section as a function of the ovalisation load (left) and bending moment capacity of single segment dependent on the normal force (right)

The increase in normal force in the middle ring is advantages with respect to the global load bearing capacity of the lining. The increase of normal force is only caused by the interaction forces between the rings. These interaction forces are in fact the slip or shear forces in the plywood between two concrete segments and are caused by mutual deformations. Deformations in a single contact area are subdivided into radial deformations and tangential deformations. Tangential deformations cause tangential forces which directly results in higher normal forces in certain segments. Radial forces may also create normal forces in a segment, just like an uniform radial forces causes an uniform normal force in a lining. In the FE model most interaction forces between the rings are radially loading the middle ring. This is the reason for the overall increase of normal forces in that ring.

### 10.1.3 Load bearing capacity of the lining

In the previous sections it is explained that by a redistribution of bending moments and a transfer of normal forces between different rings an increase in the ultimate load bearing capacity of the lining is obtained. The ovalisation load applied at failure in the FE model was  $37,7 \text{ kNm}$  and results in a maximum bending moment of  $4,525^2 \times 37,7 \times 1,0 = 772 \text{ kNm}$  in the critical cross-section according to a continuous lining. The capacity of this cross-section without incorporating redistributions is much smaller. In table 10.1 an overview of forces in the critical cross-section is given. In the fourth column the capacity of the different parts is calculated separately. As can be seen, the concrete segment is close to its bending capacity. In the fifth column the ‘real’ occurring bending moments are presented in bold. Also an estimation is given for the bending moment in certain parts when no tensile properties are assigned to the concrete or no transfer of normal forces occurs. These estimated bending moments are based on the curvatures or rotations present in the segment or joint.

Part	Tensile properties yes/no	Normal force [kN]	Bending capacity [kNm]	Present, based on curvature or rotation [kNm]	part of total loading [%]
Segment ring 2	no	1.000	370	299	39 %
Segment ring 2	yes	1.000	472	470	62 %
<b>Segment ring 2</b>	<b>yes</b>	<b>1.366</b>	<b>532</b>	<b>526</b>	<b>69 %</b>
Joint ring 1	-	1.000	85	71	-
<b>Joint ring 1</b>	-	<b>775</b>	<b>66</b>	<b>55</b>	<b>7 %</b>
Joint ring 3	-	1.000	85	71	-
<b>Joint ring 3</b>	-	<b>764</b>	<b>65</b>	<b>54</b>	<b>7 %</b>
<b>Redistribution</b>	-	-	-	<b>124</b>	<b>16 %</b>
<b>Total</b>			<b>663</b>	<b>759</b>	<b>100 %</b>

**Table 10.1:** Overview of bending moments in critical cross-section located at  $-0,50 \pi$  given for an ovalisation load of  $37,07 \text{ kN/Jack}$ , results obtained from FEA using concrete properties according to Curve IV

Based on the curvature in the segment it is calculated that without incorporating tensile properties of the concrete the bending moment in the segment would be  $299 \text{ kNm}$ . When including tensile properties a bending moment of  $470 \text{ kNm}$  should be present. Because also a transfer of normal forces to the mentioned segment occurred the ‘real’ bending moment is  $526 \text{ kNm}$ , which is 69% of the analytically calculated bending moment in that cross-section. From the table it is also made clear that by the transfer of normal forces, from joints to neighbouring segments, the bending moments in the joints are reduced to  $55 \text{ kNm}$ . Another  $124 \text{ kNm}$  is reached by redistribution of bending moments in circumferential direction leading to the analytical calculated  $759 \text{ kNm}$ .

The presented table is based on the results of the 1D FE calculation with concrete properties belonging to curve IV (figure 7.13). Using other concrete properties, like curve II or curve III, affects the bending moment in the concrete segment and will only have a very minor effect on the redistribution of bending moments or transfer of normal forces.

### 10.1.4 Ring interaction

It is expected that during experiment C01 a strong interaction between the mutual rings is present. Therefore, the ovalisation load put onto the lining reached a maximum of  $36 \text{ kN/Jack}$  before failure was recognized. At that point the shear forces, in the plywood and in the two surfaces between the plywood and the concrete, reach their maximum values.

In the FE model the contact areas are modelled using line interface elements. The resulting nodal traction forces are shown in figure 10.6. The blue dots represent the contact points in ring 2 and the connecting wires represent the direction and magnitude of the traction forces. An outward pointing vector means that ring 1 ‘pushes’ ring 2 outwards. An inward pointing vector means that ring 1 ‘pushes’ ring 2 inwards. Every plywood sheet is presented by five dots which are the nodal points in the FE model. The resulting shear force per sheet is also shown which is the sum of the five tractions in the integration points multiplied by their contact area.

Applying the uniform radial load onto the lining results in a constant normal force in the three rings. Because the segment joints possess a relatively weak stiffness in tangential direction they shorten more compared to segments, resulting in a non-uniform shortening of the lining along the circumference. Therefore, mutual tangential deformations between two rings occur causing the interface elements to deform. The resulting interaction forces after applying the complete uniform radial load are graphically represented in the left graph in figure 10.6.

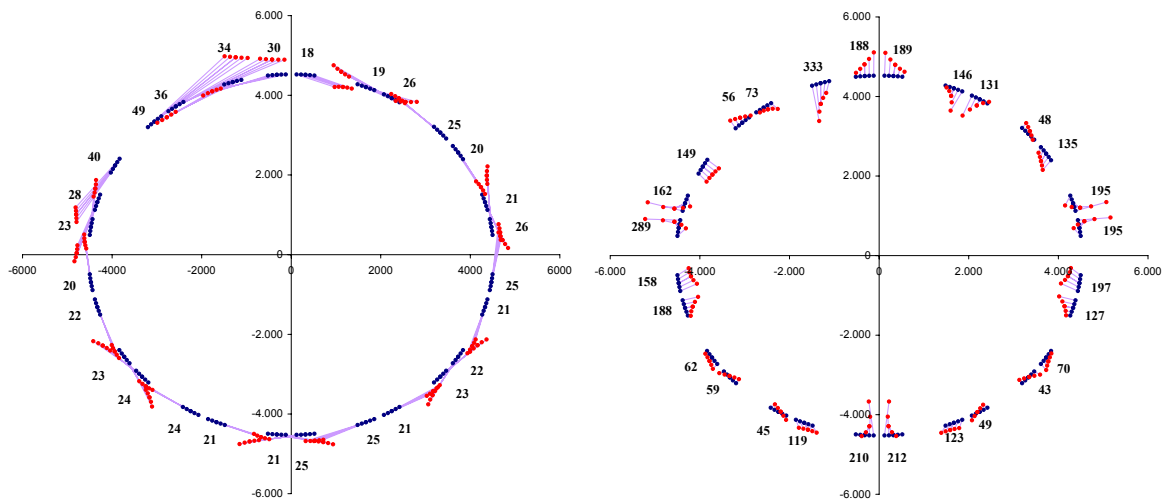


**Figure 10.6:** Interaction forces in  $kN$  between ring 1 and ring 2 after applying the uniform radial load (left) and at an ovalisation load of  $37 \text{ kN/Jack}$  (right), results from FEA using concrete properties according to Curve IV

From the graph it is concluded that the tangential interaction forces, only after applying the uniform radial load, are significant reaching a top value of  $49 \text{ kN}$  and an average shear force of  $25 \text{ kN}$ . In the full-scale test the segment joints also possess a weaker cross-section so it is expected that these tangential interaction forces also occurred in the experiment. But, because the axial force and the uniform radial force are simultaneously applied in step and not subsequently, these interaction forces are expected to be lower than found with FE analyses.

The interaction forces between ring 1 and ring 2 at an ovalisation load of  $37 \text{ kN/Jack}$  are also given in figure 10.6. The maximum interaction force is  $333 \text{ kN}$  and is located at  $0,58 \pi$ . This is an unusual high value and is caused by the fact that this interface element is not closely surrounded by other interface elements. The presented values include the tangential interaction forces due to the uniform radial load. In figure 10.7 the interaction forces are presented from which the tangential forces due to the uniform radial load are subtracted. The deviations at  $37 \text{ kN/Jack}$  between the interaction forces and the interaction forces with subtracted uniform radial interaction forces are relatively small.

$$F_{Shear} = 4F_n^{1/3}$$

$$F_n = (800.000 \times 14) / (28 \times 150 \times 400) = 6,67$$

$$F_{Shear} = 4 \times 0,83^{1/3} = 7,52$$

$$F_{Shear} = 7,52 \times 150 \times 400 = 452 \quad (10.2)$$

It is noticed that the shear forces at  $37 \text{ kN/Jack}$  are primarily directed in a radial direction meaning that governing mutual deformations between the two rings are in radial direction. The average shear force is  $134 \text{ kN}$ . The most heavily loaded interface elements are located at the cross-sections in which the bending moments are maximal possessing an average force of about  $200 \text{ kN}$ . According to equation 10.2 the shear strength of the interface elements is  $452 \text{ kN}$  concluding that the found interaction forces are realistic and no slip of the joints occurred. In the most heavily loaded interface elements the corresponding friction coefficient was at least  $317/400 = 0,79$  which is a realistic value for the used kind of packing material.

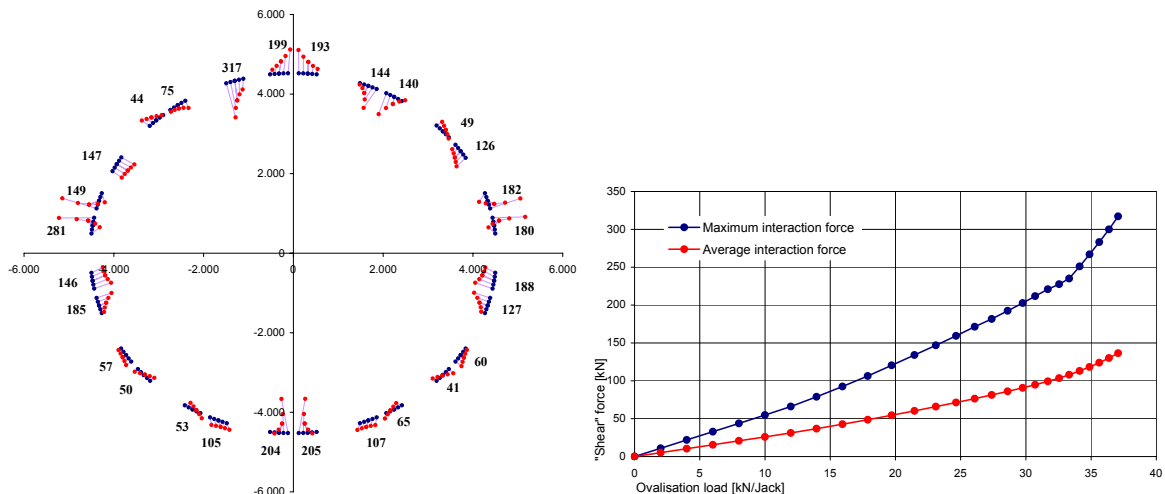


**Figure 10.7:** Interaction forces in  $kN$  between ring 1 and ring 2 from which the interaction forces after applying the uniform radial load are subtracted (left) and as a function of the ovalisation load (right)

In figure 10.7 the average and the maximum shear force is presented graphically as a function of the ovalisation load. These interaction forces are with subtraction of the interaction forces due to the uniform radial load. In this graph it is shown that the shear forces increase

almost linearly at increasing the ovalisation load until  $33 \text{ kN/Jack}$ . Cracking of the concrete seems not to affect the shear forces.

## 10.2 Experiment C02

From previous sections it may be concluded that concrete properties lay somewhere in between values belonging to curve III and IV (figure 7.13). Furthermore can deformations of the lining be simulated very well just like rotations in the joints. The performed analysis were all compared to experiment C01 which is characterized by a high axial load. In this paragraph FE analyses are presented simulating the second experiment which is characterized by a low axial load.

Since some segments started to crack at final stages of loading during the first experiment, not all segments are in a perfect condition at the start of the second experiment. Therefore the lining might behave in a less stiff manner. To include the influence of damaged segments it is necessary to ‘perfectly’ simulate experiment C01 by fitting experimental deformations. After unloading, a damaged lining is obtained which is used at the start of the second experiment.

Another difference between the first and the second experiment is the applied axial force. In the second experiment this axial force is one eighth of the axial force applied in C01. The small axial force mainly affects the behaviour of the plywood. The transferable shear force is lower whereas the initial stiffness is unchanged. Implementing this behaviour in the FE model means modifying material properties belonging to the interface elements between the rings. Instead of a linear stiffness a bi-linear shear-deformation diagram is implemented. The level of the horizontal branch is dependent on the applied axial force and is estimated based on equation 10.3. According to this relation, the maximum transferable shear force per plywood sheet is  $226 \text{ kN}$ . It is emphasized that this equation is based on experimentally obtained shear strengths for plywood exposed to a normal force varying between  $11 \text{ N/mm}^2$  and  $35 \text{ N/mm}^2$  [Gijsbers and Hordijk 1997], whereas the normal force in the plywood is  $0,83 \text{ N/mm}^2$  in the full-scale tunnel experiment. Therefore these tests are not representative but do give an indication for the strength of the plywood.

$$\begin{aligned}
 F_{Shear} &= 4F_n^{1/3} \\
 F_n &= (100.000 \times 14) / (28 \times 150 \times 400) = 0,83 \\
 F_{Shear} &= 4 \times 0,83^{1/3} = 3,76 \\
 F_{Shear} &= 3,76 \times 150 \times 400 = 226
 \end{aligned} \tag{10.3}$$

The above mentioned equations result in a shear strength of  $226 \text{ kN}$  which corresponds to a very high friction coefficient of  $226/50 = 4,5$ . The experiments by Gijsbers and Hordijk (1997) do indicate that friction coefficients increase at decreasing normal forces, but it is not expected that these high friction coefficients can be reached. The specimen subjected to the lowest normal force  $\sigma_n = 11,5 \text{ N/mm}^2$ , possessed a friction coefficient of  $0,73$  [Gijsbers and Hordijk 1997]. A friction coefficient of  $0,73$  should result in a shear strength of  $50 \times 0,73 = 37 \text{ kN}$  per plywood sheet in the second experiment.

By implementing the shear strength in the material properties of the interface elements the load bearing capacity of the complete lining is limited. To investigate the influence of the level of the bi-linear branch on the load bearing capacity of the lining a number of FE calculations is performed with different shear strengths for the plywood. In figure 10.8 the implemented material properties of the plywood are shown just as their effect on the global lining deformations.

Before going into detail about the implemented shear strengths, it is necessary to know more about how DIANA deals with these strengths. The mutual deformations between two integration points of two rings connected with an interface are subdivided in a global X and a global Y deformation. Subsequently, the deformations and tractions ('shear' stresses) are calculated per separate direction. If the deformations in one or two directions are larger then the deformations corresponding to the shear strength then the stress is limited. Due to the fact that the mutual deformation is subdivided into two directions the resulting strength is not always equal. The interaction force is lower when the resulting mutual deformation in the interface element is in the y-direction then when the resulting mutual deformation is subdivided into two directions. Depending on the circumferential location and the mutual deformation between the two rings, the *uncoupled* relation results in different shear strengths along the circumference of the lining and is a shortcoming of the FE model. In reality this relation is *coupled* resulting in a shear strength independent of the mutual deformation direction.

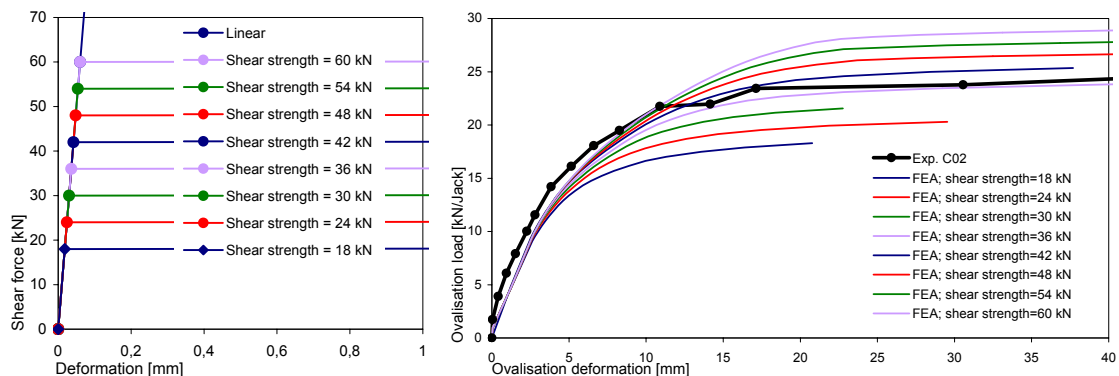


**Figure 10.8:** Several stress-deformations diagrams for the plywood sheets (left) and FE results of these diagrams implemented in the complete lining model (right)

The highest implemented shear strength in the FE model is 60 kN resulting in a relatively high load bearing capacity of the lining as is seen in figure 10.9. Because of the uncoupled behaviour, as explained in the previous paragraph, the 60 kN strength in practice can result in an interaction force of  $\sqrt{60^2 + 60^2} = 85$  kN. An implemented shear strength of 36 kN results in a more accurate approximation of the deformations and load bearing capacity. This approximation of the second experiment is shown in figure 10.9 in more detail including the simulation of the first experiment and a simulation of the second experiment without implementing a shear strength. The deformations of the lining in the second experiment begin to deviate from the loading branch of the second experiment without a shear strength at an ovalisation load of 15 kN/Jack. This is an indication that one or more interface elements have reached their strength. At increasing the load the deformations start to deviate even more from the simulation without a shear strength until at 24 kN/Jack the deformations

reach a horizontal plateau indicating failure.

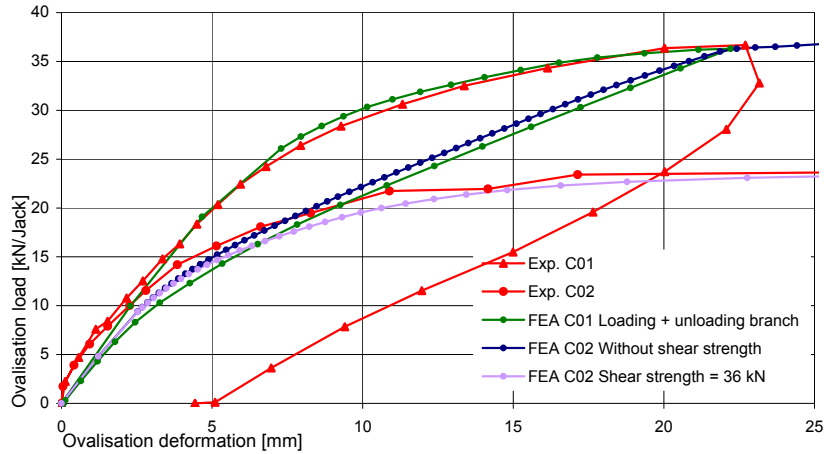


**Figure 10.9:** FEA of experiment C01 and C02

The experimentally ‘fitted’ deformations simulating experiment C01 including the unloading branch, are also shown in figure 10.9. Experimental deformations show a significant plastic deformation left after loading whereas the deformations in the numerical simulation return to zero. There may be a number of explanations for this plastic deformation. When looking at figure 5.9 it is concluded that the plastic deformation is mainly due to rotations in the joints not returning to zero and by some plastic deformation left in the segments. It is also very likely that deformations in the plywood did not return to zero in the experiment. These effects are not included in the FE model leading to no plastic deformations. It is noticed that the experimentally observed stiffness at the end of unloading is very much the same as found with the FE model.

In previous chapters the results of the first experiment and the FE analyses are compared extensively. Figure 10.9 seems to indicate that also the second experiment is simulated quite well although only the average total deformations are shown. In appendix F the joint and total deformations per ring are compared to numerical results and a very good agreement is found. The rotations in every single joint are also plotted and compared just like the compression strains on the complete lining. It is concluded that a very good agreement is found between the full-scale experiment and the numerical simulations. Therefore, the behaviour of the lining under loadings put onto the lining in the second experiment is further analysed using the FE model.

### 10.2.1 Redistribution of bending moments

Due to the fact that some segments are damaged at the start of the second experiment and due to the fact that the shear strength for the interface elements is implemented, it is interesting to study and compare the bending moment distribution at a certain ovalisation load in both models. In figure 10.10 the bending moment distribution simulating experiment C01

and C02 is compared with analytical values for the bending moments. The distribution is plotted at an ovalisation load of  $10 \text{ kN}/\text{Jack}$ . At this low load the redistribution of bending moments in circumferential direction is somewhat larger in the second experiment. This is easily explained by the fact that the critical cross-section is already heavily cracked leading to a even weaker cross-section and a redistribution of bending moments from the early start of loading. It is emphasized that only a minor redistribution is noticed. The redistribution of bending moments in circumferential direction is not increasing when increasing the load. A significant redistribution in circumferential direction during loading does not occur!

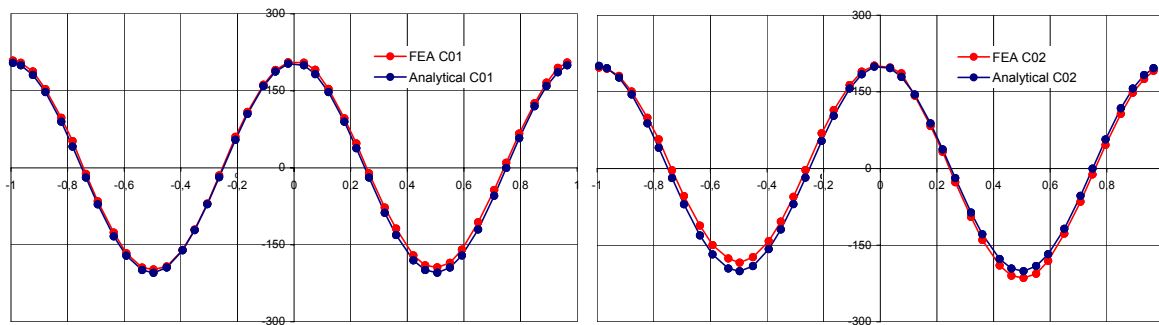


**Figure 10.10:** Comparison of bending moments in circumferential direction at an ovalisation load of  $10 \text{ kN}/\text{Jack}$  between analytical and FE results, experiment C01 (left) and C02 (right)

In appendix H the bending moments are outlined per separate ring at different load steps in which a comparison is made between experiment C01 and C02. From the graphs in the appendix it is noticed that the bending moments in the second experiment compared to the first experiment lay closer to the analytical expected bending moments. At the critical cross-sections the peak bending moments in the segments are lower meaning that less redistribution of bending moments in axial direction is taking place. The lower axial force in the second experiment is not responsible since this behaviour is noticeable before the shear strength of the plywood is reached. A physical explanation for the less redistribution in axial direction is the fact that the difference between the bending stiffness of a cracked segment and a neighbouring joint is reduced. Therefore, the segments rotate more without attracting additional bending moments whereas the neighbouring joints rotate more and thereby absorb higher bending moments. This is exactly what is seen in the mentioned appendix.

At higher ovalisation loads the interface elements reach their strength but no significant influence on the distribution of bending moments is noticed. It is emphasized that the above discussed difference in redistribution of bending moments in axial as well as in circumferential between the first and the second experiment is only very small. Significant redistributions of bending moments are taking place at higher ovalisation loads, as discussed 10.1.1, and are not reached in experiment C02.

### 10.2.2 Ring interaction

In the second experiment a much weaker interaction between the mutual rings is present due to the relatively low axial force. In figure 10.11 the interaction forces between ring 1 and

ring 2 are shown after applying the uniform radial load in experiment C02. Just like in the first experiment, these forces are primarily in a tangential direction. The resulting forces are lower compared to the first experiment but still significant. In the same figure the mutual displacements at an ovalisation load of  $22 \text{ kN/Jack}$  at the locations of the interface elements are shown. Just as in the first experiment it is noticed that the largest mutual deformations are found at the location of the cross-sections possessing high bending moments. At this final stage of loading some of the interface element reached their strength as is seen in figure 10.12. The highest shear forces are  $51 \text{ kN}$  which is equivalent to  $\sqrt{36^2 + 36^2} = 51 \text{ kN}$  indicating that 13 out of the 28 interface elements reached their strength at an ovalisation load of  $22 \text{ kN/Jack}$ .

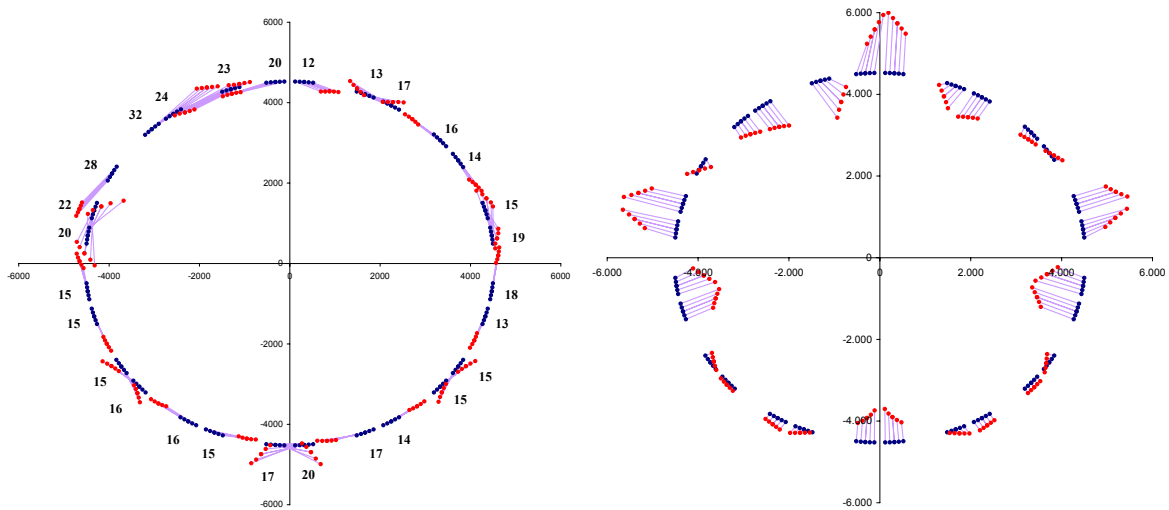


**Figure 10.11:** Interaction forces in  $kN$  between ring 1 and ring 2 after applying the uniform radial load (left) and the displacements between ring 1 and ring 2 at an ovalisation load of  $22 \text{ kN/Jack}$  (right)

Although the mutual deformations due to the uniform radial load and the ovalisation radial load are perpendicular, the shear strength of the interface elements is reached earlier compared to the case when no interaction forces due to the uniform radial load should have occurred. Therefore the interaction forces at an ovalisation load of  $22 \text{ kN/Jack}$  are shown from which the tangential forces after applying the uniform radial load are subtracted. These values represent the occurring forces in case the tangential forces did not occur.

Figure 10.12 is indicating that shear strengths varying between the  $50 \text{ kN}$  and the  $70 \text{ kN}$  are present in the lining at an ovalisation load of  $22 \text{ kN/Jack}$ . At that point the load bearing capacity of the lining is almost reached and total lining deformations of  $17 \text{ mm}$  are present. When increasing the ovalisation load the deformations begin to grow rapidly and all interface elements reach their shear strength. From this FE model it might be concluded that forces in the plywood sheets at failure lay somewhere in the ranch of  $50 \text{ kN}$  to  $70 \text{ kN}$  which corresponds to a friction coefficient of about 1. In this FE model the interface elements located at the critical cross-sections were reaching their shear strength at  $15 \text{ kN/Jack}$ . At increasing the load, more and more interface elements reached their strengths until at  $23,5 \text{ kN/Jack}$  all interface elements reached their capacity and a horizontal branch in the load-deformation diagram is reached.

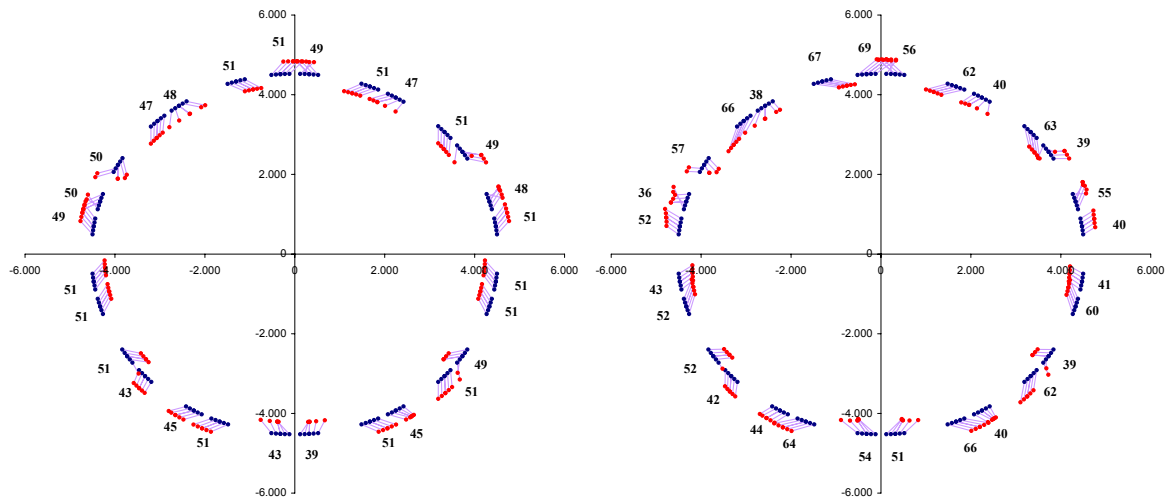


**Figure 10.12:** Interaction forces in  $kN$  between ring 1 and ring 2 at an ovalisation load of  $22 kN/Jack$ , resulting values (left) and forces from which the forces after applying the uniform radial load are subtracted (right)

In the horizontal branch of the load-deformation diagram the deformation increases without an increase in the applied load. The deformations grow and are primarily caused by an ongoing rotation of the segment joints. The curvatures in the segments show a light increase in these last load steps.

At the start of applying the ovalisation load in the second experiment some of the segments were damaged. At that stage the cracks are closed due the uniform radial load and gradually start to reopen. Only a very few additional cracks are noticed at maximum load.

# Chapter 11

## Conclusions and recommendations

### 11.1 Conclusions

For studying the failure behaviour of segmented tunnel linings, the results of two different tests have been analysed. In the first test a rather high axial force was applied, whereas in the second test a low axial force was applied. From the test results as well as from the analyses with the developed beam model it appeared that the axial force is governing the interaction between the ring joints, and therefore the lining behaviour. The numerical model developed consisted of a simple beam model, in many ways corresponding to regular engineering models.

Referring to the main objective of this thesis it has been shown that failure of the lining under ovalisation load can be predicted rather accurately with the adopted beam model, regardless of the failure mechanism (joint failure or segment failure). The beam model as used in engineering practice has therefore been proven to be applicable for describing ovalisation of segmented tunnel linings in the Ultimate Limit State. Also from a more scientific point of view the beam model offers great advantages due to the fact that only a very short computing time is needed offering the ability to perform influence analyses as well as probabilistic safety analyses.

From the results of the analyses and the tests, moreover, the following conclusions are drawn:

- It has been shown that the total deformation can be calculated from the joint rotations, the segment curvatures and segment cracking. Depending on the axial force, either the joint rotations or the segment rotations due to cracking are governing the deformations in the Ultimate Limit State.
- The calculated deformations due to the ovalisation load as well as the calculated strains almost perfectly match the experimental observations for both levels of the axial force tested.
- The ring interaction dominates the failure mode. For a high axial force, failure is induced by failure of the segments (concrete cracking and yielding of the reinforcement steel). For a low axial force, failure is dominated by the segment joints (joint failure).

- The numerical simulations have shown that the tested high capacity may be explained from the following phenomenon:
  - The ultimate bending moment of the segments is affected strongly by the softening behaviour of the concrete in tension because of the rather low reinforcement ratio, and has a large effect on the load bearing capacity of the lining.
  - By the redistribution of bending moments in circumferential direction an increase in the ultimate load capacity is obtained.
  - Due to a redistribution of the normal hoop force in axial direction a limited increase in the bending capacity of the critical concrete segments is obtained.

It has been shown that a conservative approach is followed when in the design ring interaction is neglected.

- The stiffness of the ring joints based on the literature is between the  $10^5$  to  $10^6$   $N/mm$ . Provided that only one plastic hinge develops along the circumference the effect is rather large. However, because in the Ultimate Limit State analyses three plastic hinges develop almost simultaneously, the effect is limited.
- Comparison of the results obtained with the beam model to a more detailed membrane model shows that the segment cracks are less localized in the beam model. The effect on global (ovalisation) behaviour, however, is limited.
- The tests and the numerical analyses have shown that a rather low axial force suffices for an adequate interaction between the neighbouring rings, resulting in segment failure as the dominant failure mechanism. As a result it may be stated that shallow bored tunnels (i.e. low axial force) in soft soil conditions may be feasible, provided that the axial force remains present during the service life of the tunnel.
- By simulating the rotational behaviour of the segment joints and by determining the role of the joint deformations related to the total ovalisation, it was found that the Janssen concept results in a realistic joint behaviour.

## 11.2 Recommendations

From the research performed the following recommendations to engineering practice are given:

- Because of the large uncertainties with respect to the softening behaviour (fracture energy, characteristic length, etc.) and its effect on the total bending capacity, it is recommended not to take into account the softening behaviour when designing a tunnel lining.
- For predicting the load bearing capacity of a segmented tunnel lining under ovalisation the Janssen concept may be used. It is recommended to adjust the initial stiffness according to earlier performed (joint) experiments.
- Disadvantage of the numerical model as used in the current research is the limited interaction in axial direction. As a result the model is not fit to deal with unequal soil settlements. Because bending in axial direction is governed by local rotations in the

ring joints it is advised to include this axial component by assigning axial properties to the ring interface elements.

From the results the following recommendations for further research are given:

- The interaction between neighbouring rings is strongly affected by the configuration and location of the ring joints. It is recommended to study the effect of applying interfaces between the neighbouring rings rather than point to point springs, as generally used in engineering beam models.
- Engineering beam models generally result into a realistic design approach, provided that concrete cracking is taken into account and that the axial force remains present during the service life of the tunnel. It is recommended to study the long term behaviour of the plywood sheets and the effect on a possible loss of the axial force.
- The additional lining capacity is governed among others by the interaction between neighbouring rings. Because the adopted models (beam and membrane) do not take into account any geometrical effects in axial direction, it is recommended to verify this phenomenon using a more advanced model (shell or solid).
- In the analyses the effect of the surrounding soil is not taken into account. Before using the model in practice it is finally recommended to study the effect of the interaction between lining and soil.



# Bibliography

A.M. Alvaredo, R.J. Torrent: *The effect of the shape of the strain-softening diagram on the bearing capacity of concrete beams*, RILEM Materials and Structures, 20(120), pp 448-454

K.J. Bakker: *Soil Retaining Structures, Development of Models for Structural Analysis*, Ph.D. Thesis TU Delft, 2000

T. Baumann: *Tunnelauskleidungen mit Stahlbetontubbingen*, Bautechnik 69, Heft 1, 1992

C.B.M. Blom: *Liggerwerking van boortunnels, Krachtswerking in de tunnelmantel door ongelijkmatige zettingen*, Master Thesis TU Delft, November 1995

C.B.M. Blom: *Lining Behaviour - Analytical solutions of coupled segmented rings in soil*, Background document Ph.D. Thesis TU Delft, 2002

C.B.M. Blom: *Design philosophy of concrete linings for tunnels in soft soils*, Ph.D. Thesis TU Delft, 2002

J.O. Bickel, T.R. Kuesel, E.H. King: *Tunnel engineering handbook*, Chapman New York, 1996

R. Burgers: *Non-Linear FEM modelling of steel fibre reinforced concrete for the analysis of tunnel segments in the thrust jack phase*, Master Thesis TU Delft, September 2006

H. Duddeck, J. Erdmann: *Structural design models for tunnels*, Tunnelling 1982, Proc. 3. Intern. Symp., Institution of mining and metallurgy, London 1982 83-91

J. Erdmann, H. Duddeck: *Statik der tunnel im lockergestein - Vergleich der berechnungsmodelle*, Bauingenieur 58, 407-414, 1983

W.H.N.C. van Empel: *Liggerwerking gesegmenteerde boortunnels, Krachtswerking gesegmenteerde boortunnel, belast als ligger*, Master Thesis TU Delft, March 1998

C.M. Frissen, B.F.J. van Dijk, G.A. Visser: *Grondbelasting en stijfheden*, CUR/COB L500, October 1997

- F.B.J. Gijsbers, D.A. Hordijk: *Experimenteel onderzoek naar het afschuifgedrag van ringvoegen*, CUR/COB K11-W-001, November 1997
- G. Gioda, G.S. Woboda: *Developments and applications of the numerical analysis of tunnels in continuous media*, Int. J. Numer. Anal. Meth. Geomech., 23, 1391-1405, 1999
- G.M.L. Gladwell: *Contact problems in the classical theory of elasticity*, ISBN 90 286 0440 5, Alphen aan den Rijn, 1980
- F. Gruebl: *Modern design aspects of segmental lining*, Lecture and extended abstract: International seminar on tunnels and underground works, Lisbon 2006
- A. Hillerborg, A. Modeer, P.E. Person: *Analysis of crack formation and crack growth in concrete by means of fracture mechanics and finite elements*, Cement and Concrete Res., 6, pp. 773-782
- D.A. Hordijk: *Local approach to fatigue of concrete*, Ph.D. Thesis TU Delft, October 1991
- D.A. Hordijk, F.B.J. Gijsbers: *Laboratoriumproeven tunnelsegmenten*, CUR/COB, Projectbureau boortunnels, June 1996
- D.A. Hordijk, H.A.W. Cornelissen, H.W. Reinhardt: *Experimental determination of crack softening characteristics of normalweight and lightweight concrete*, Heron 31, 1986
- E.J. van der Horst: *Invloed van voegmaterialen op de krachtswerking in gesegmenteerde betonnen boortunnels*, Master Thesis TU Delft, May 1998
- P. Janssen: *Tragverhalten von tunnelausbauten mit gelenktubbings*, Ph.D. Thesis Technischen Universitat Carolo-Wilhelmina, Braunschweig, December 1983
- N.D. Joustra, F. Vahle: *Gesegmenteerde lining, Voeggedrag*, CUR/COB L530 Cluster 31, October 1997
- A.J. Koek: *Axiale voorspanning in de lining van een geboorde tunnel, Onderzoek naar axiale normaalkracht in tunnelling tijdens bouwfase en gebruiksfase*, Master Thesis TU Delft, November 2004
- A.G. Kooiman, C. van der Veen, C.B.M. Blom: *Geboorde tunnels met betonnen segmenten*, April 2004
- K.M. Lee, X.Y. Hou, X.W. Ge, Y. Tang: *An analytical solution for a jointed shield-driven tunnel lining*, Int. J. Numer. Anal. Meth. Geomech., 25, 365-390, 2001
- R.D. Mindlin: *Stress distribution around a tunnel*, Trans. ASCE, 1117-1153, 1950

- R. Peters, B. Zafari: *Modellering van het tunnelboor- en consolidatieproces*, Bouwdienst Rijkswaterstaat, March 2000
- D. Postma, R.G.A. de Waal, C. van der Veen: *Analytische rekenmodellen voor geboorde tunnels*, Cement 1997 nr. 10, Oktober 1997
- H. Schulze, H. Duddeck: *Spannungen in schildvorgetriebenen tunnels*, Beton- und Stahlbetonbau, Heft 8, Jahrgang 59, August 1964
- E.O. Strack: *A complex variable solution for the ovalization of a circular tunnel in an elastic half-plane*, GeoEng2000, 19-24, November 2000, Melbourne
- A. Verruijt: *A complex variable solution for a deforming circular tunnel in an elastic half-plane*, Int. J. Numer. Meth. Geomech. 21, 77-89, 1997
- A.H.J.M. Vervuurt, F.B.J. Gijsbers: *Eerste orde evaluatie tunnelconstructie: Predictiemodellen, postdictieberekeningen en vergelijking met meetresultaten*, K100 Praktijkonderzoek boortunnels, November 1999
- A.H.J.M. Vervuurt, J.A. den Uijl, F.B.J. Gijsbers, C. van der Veen: *Aanvullende proeven in de tunnelproefopstelling: Constructiegedrag onder gebruiksbelastingen en het effect van plaatsingson nauwkeurigheden. Deel 1: Opzet en resultaten van Serie A*, Delft Cluster, February 2003
- A.H.J.M. Vervuurt, J.A. den Uijl, F.B.J. Gijsbers, C. van der Veen: *Aanvullende roeven in de tunnelproefopstelling: Constructiegedrag onder gebruiksbelastingen en het effect van plaatsingson nauwkeurigheden. Deel 2: Resultaten van serie B*, Delft Cluster, Februar 2003
- A.H.J.M. Vervuurt, J.A. den Uijl: *Bezwijkveiligheid boortunnels, Meetrapport en evaluatie proevenserie C*, TNO-report 2005-CI-R0232, April 2006
- A.H.J.M. Vervuurt, W.J.P. van Gogh: *Handleiding bij het programma 'DRNS' voor het maken van doorsnede berekeningen voor gewapende en voorgespannen betonconstructies*, TNO-report, December 2000
- A. Verweij: *4D- Groutdrukmodel Plaxis*, COB-F220, July 1995
- M.A.T. Visschedijk, W.H.N.C. van Empel, A.H.J.M. Vervuurt, N.M. Naaktgeboren: *Elementaire liggerwerking*, CUR/COB L530 31.3, August 1998
- C. van der Vliet: *Langsvoeggedrag op basis van de elasticiteitstheorie, Een aanscherping van de Janssen-relatie*, Bouwdienst Rijkswaterstaat, July 2006
- N.M. Vollema: *Ringwerking in geboorde tunnels, Vergelijking van numerieke modellen*, TNO Bouw/TU Delft, January 1996

J.K. Vrijling: *Bored and immersed Tunnels*, March 2006

J.C. Walraven, J.C. Galjaard: *Voorgespannen beton*, January 1997

R. Windels: *Kreisring im elastischen Kontinuum*, Bauingenieur 42, 429-439, 1967

F.C. de Witte, G. Schreppers: *DIANA User's Manual*, TNO DIANA BV, Delft, August 2006

**Part IV**  
**Appendices**



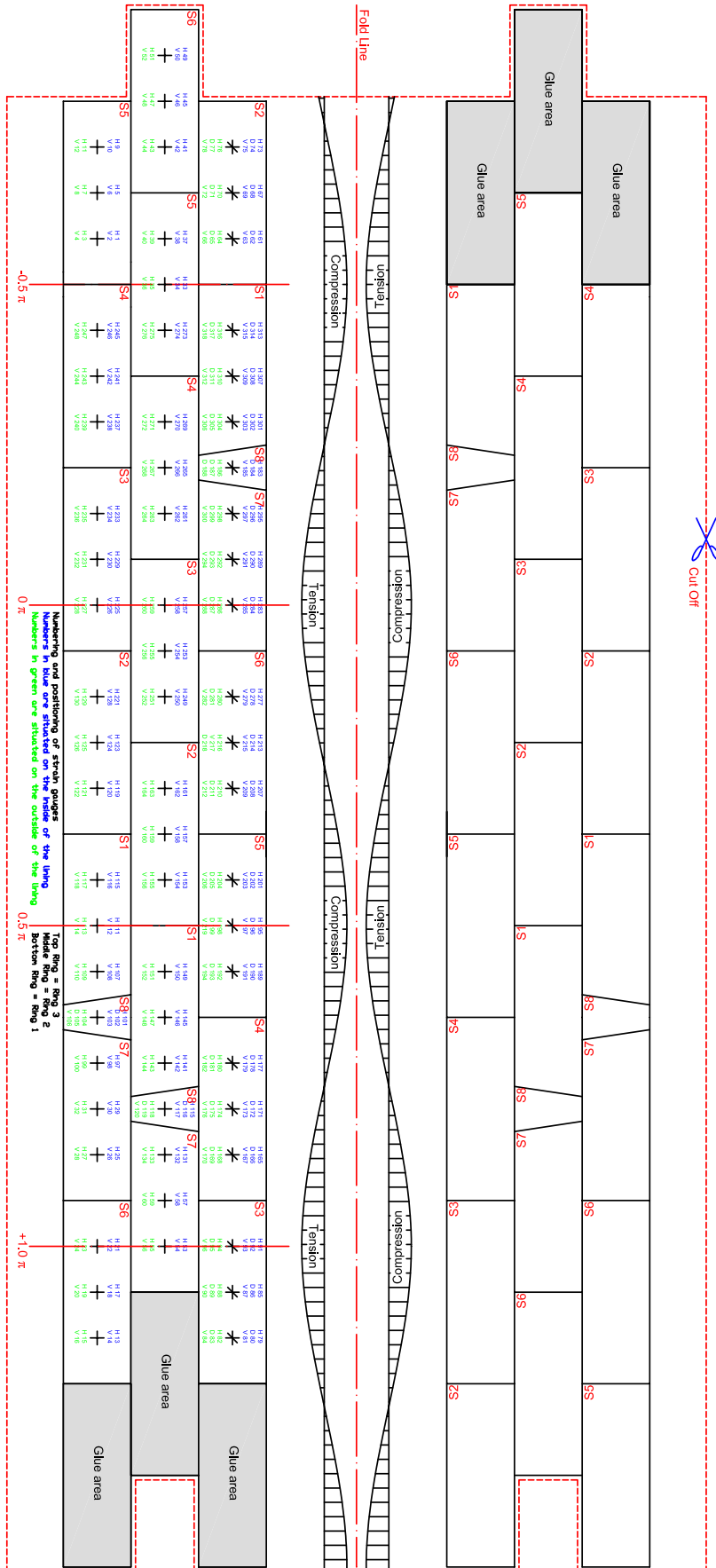
## Appendix A

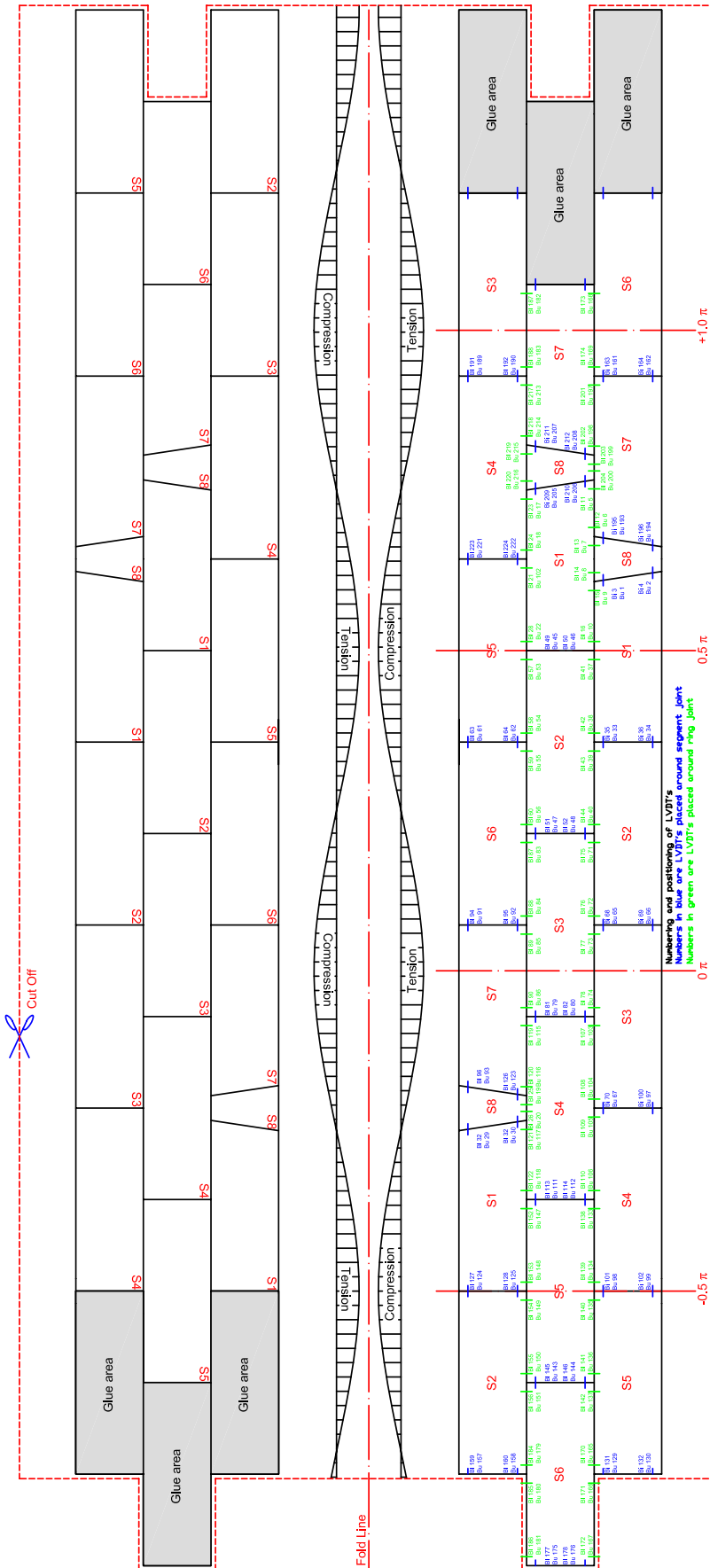
# Numbering and positioning of measurement devices

In this appendix an overview of the different measurement equipment is given. In the first figure the location and numbering of the strain gauges on the segments is presented and in the second figure the location and numbering of the LVDT's place on segment and ring joints are presented.

Because it is very difficult to get a clear picture in mind of the complete lining and its configuration from a plane figure, it is better to make a 3D model of the lining. Therefore, the figures are included with cutting and fold lines. First the paper has to be cut along the dashed line after which the paper has to be folded over the dash-dotted fold line. Subsequently glue has to be attached on the two hatched areas and by making a circle, these areas can be pressed together. After a few minutes the glue is dry and a scale model of the experimental lining is obtained. It is recommended to construct this scale model since it can be very helpful understanding this report.

# Ultimate Limit State Analysis of a Segmented Tunnel Lining







## Appendix B

# Calculation deformations of lining

On the next page a spreadsheet is shown from which the deformed shape of the lining is calculated. The coordinates of the lining are determined in the joints and on three points of every segment, resulting in a total of 37 coordinates per ring. The spreadsheet starts with different input options. The coordinates are calculated for a specific entered step number. From this step number a reference step is subtracted so deformations only caused by, for example, the ovalisational load can be determined. It is possible to give different enlargement factors for joint rotations and segment curvatures to be able to investigate deformations only caused by joint rotations. Every segment joint is equipped with a total of four LVDT's, one on top and one on the bottom, on the inside and outside of a joint. From these four LVDT's it is possible to determine a rotation on top or on the bottom or an average of those two.

**Information** In the first columns information on the non-deformed and non-loaded lining is reproduced. The coordinates of every joint and of three points of every segment is given. The numbers of the measurement devices is also given, for the joints the numbers of the LVDT's and for the segments the numbers of the strain gauges is given.

**Coordinates without loading** In the second section of columns additional information is extracted which is valuable for determining coordinates of the deformed lining.

**Collecting measured data** In the third section of columns the measured data is collected. This data is collected from another spreadsheet, CO1\_str-eng.xls for the first experiment or C02\_str-eng.xls for the second experiment. Using this data the rotations in the joints and the curvatures in three points of every segment is determined. The curvatures in the segments are multiplied by a part of the segment length to determine a rotation. Finally the calculated rotations are multiplied by an enlargement factor to finally make deformations visible.

**Correcting, closing and repositioning lining** In the fourth section of columns the collected rotations are corrected as explained in chapter 5.1. After this correction another correction is performed resulting in a closed lining. In the last section of columns the deformed shape is repositioned. The centre of the lining is calculated and repositioned to  $x=0$  and  $y=0$  and is rotated as shown in figure 5.5. In the final two columns the coordinates of 37 points of the lining are given. For ring 2 and ring 3 the same calculations are performed and when

performed for all load steps a good representation of deformations during the experiments is obtained.





## Appendix C

# Deformations of lining in experiment C01

The deformed shape of the lining in experiment C01 is drawn for several loading steps. The deformed shape is based on joint rotations and segment curvatures. The deformations are multiplied by a factor 50.

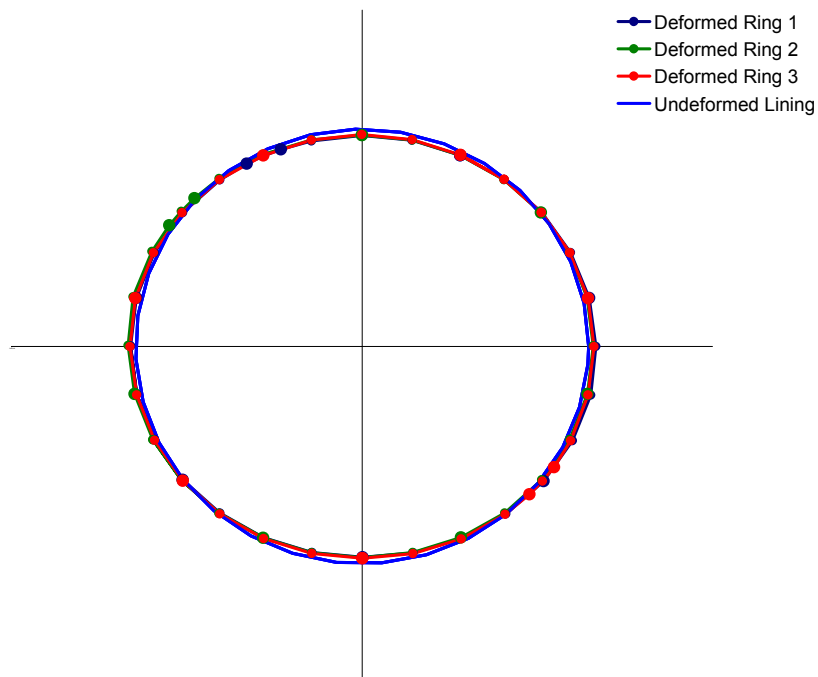


**Figure C.1:** Deformation of the lining, experiment C01, step 15, enlargement factor 50

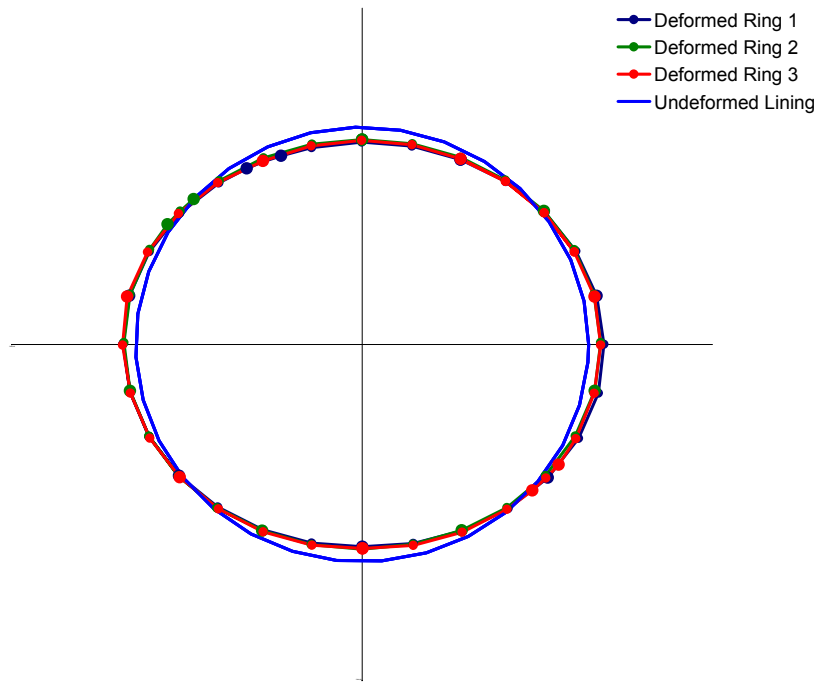


**Figure C.2:** Deformation of the lining, experiment C01, step 20, enlargement factor 50

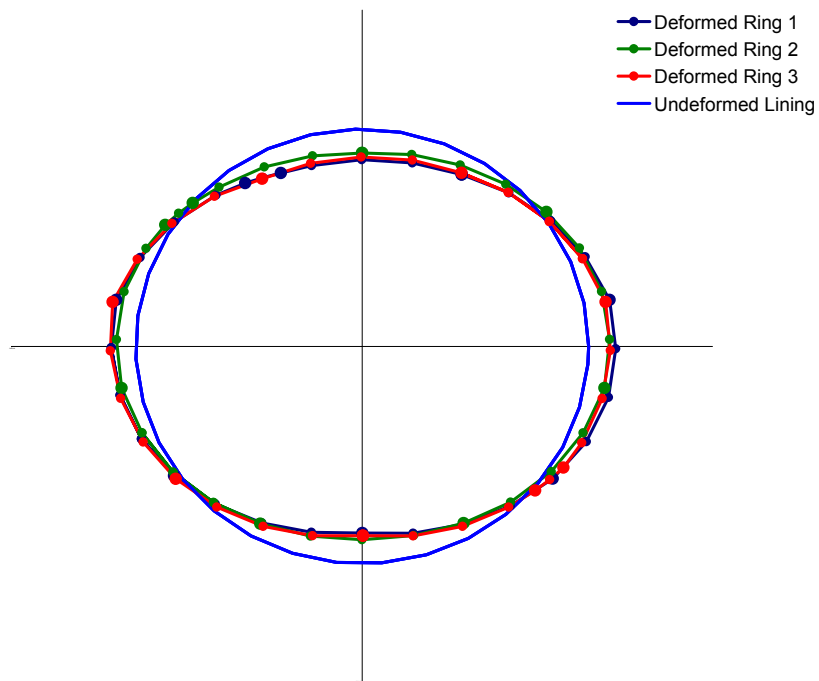


**Figure C.3:** Deformation of the lining, experiment C01, step 25, enlargement factor 50

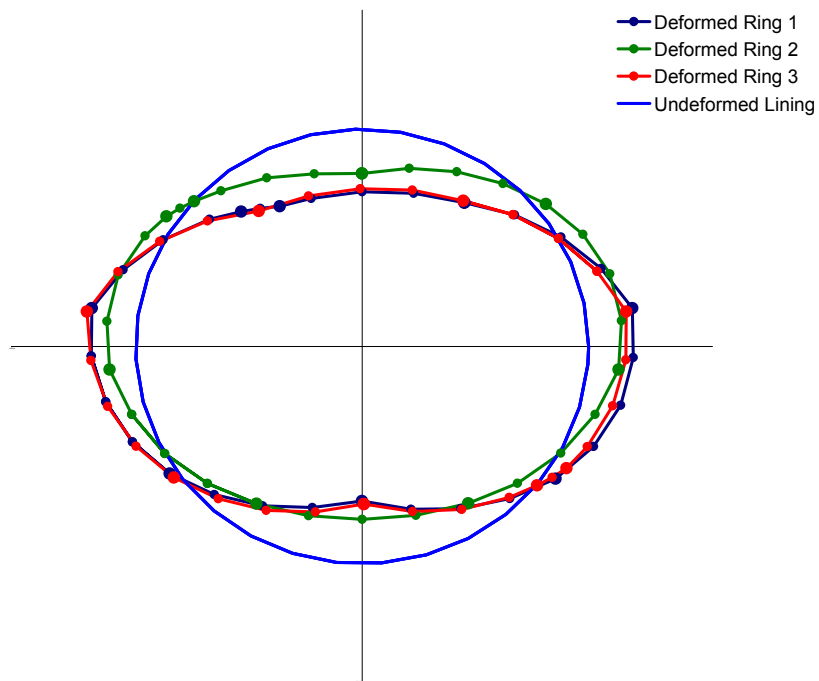


**Figure C.4:** Deformation of the lining, experiment C01, step 30, enlargement factor 50



## Appendix D

# Deformations of lining in experiment C02

The deformed shape of the lining in experiment C02 is drawn for several loading steps. The deformed shape is based on joint rotations and segment curvatures. The deformations are multiplied by a factor 50.

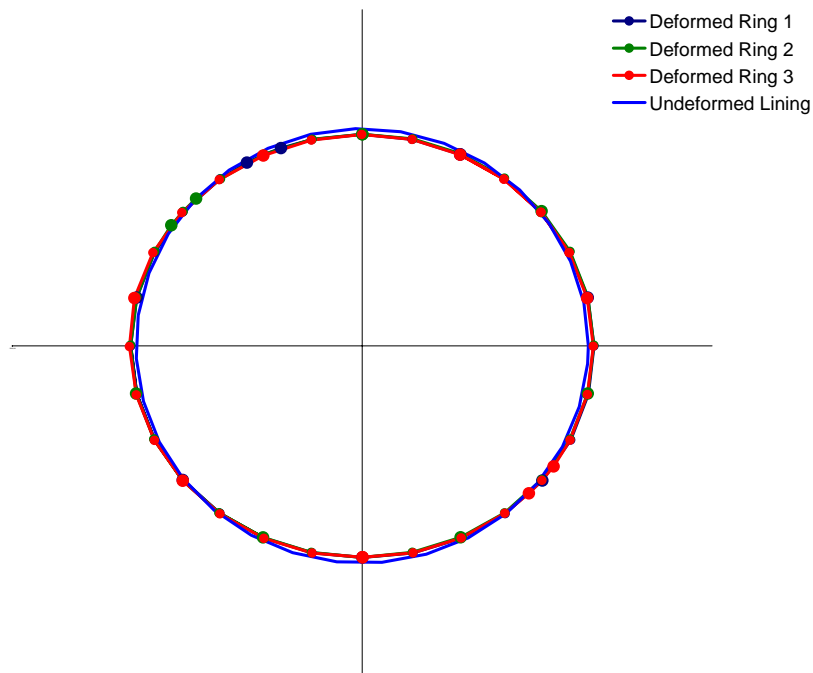


**Figure D.1:** Deformation of the lining, experiment C02, step 17, enlargement factor 50

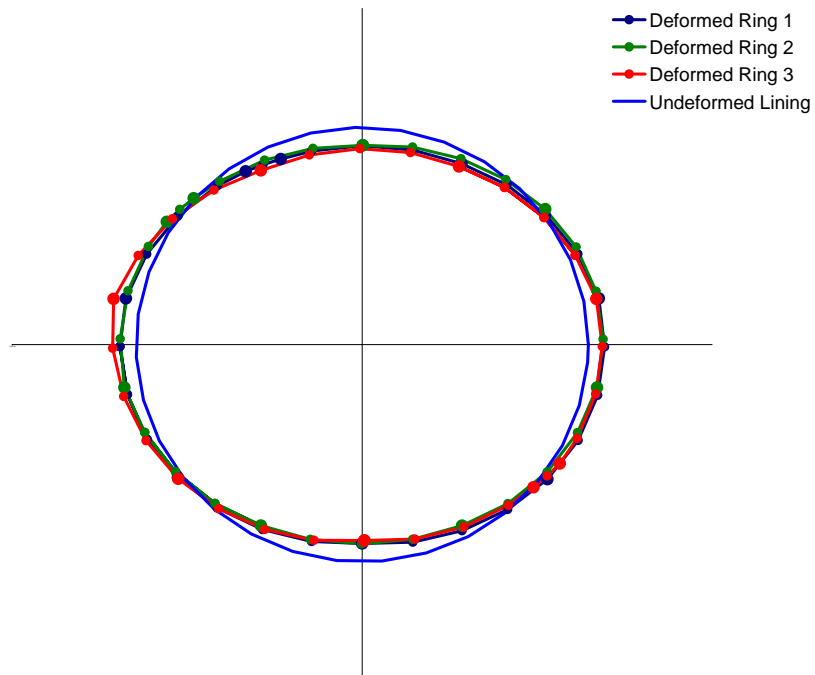


**Figure D.2:** Deformation of the lining, experiment C02, step 22, enlargement factor 50

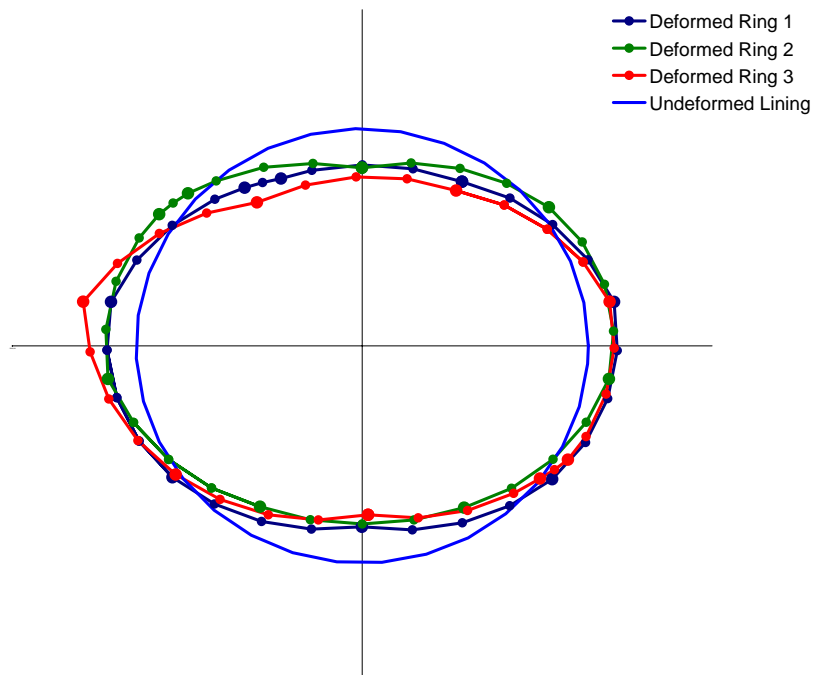


**Figure D.3:** Deformation of the lining, experiment C02, step 25, enlargement factor 50

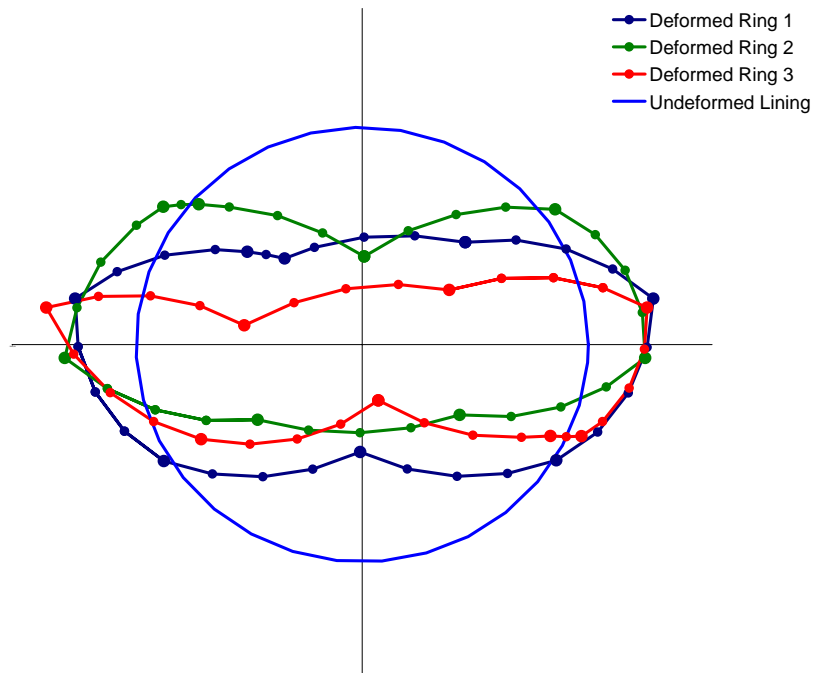


**Figure D.4:** Deformation of the lining, experiment C02, step 28, enlargement factor 50



## Appendix E

# Ovalisational deformation of lining

The ovalisational deformation of the lining is calculated as the average radial deformation of four points on the lining. These points are located on the same circumferential location as the radial measurements equipment (TU1-TU12) and possess therefore maximum radial deformations. These total deformations are drawn for each separate ring resulting in 3 graphs per experiment. The deformations caused by joint rotations and deformations caused by joint rotations and segment curvatures are also plotted in these graphs. Important is the difference in deformations caused by joint rotations in ring 1 and 3 compared to the deformations of ring 2.

The deformations are presented graphically in figures E.1-E.6. The exact numerical values are given in figures E.7 and E.8. In these two tables the deformations caused by the joints, caused by the segments and the total deformations are given. The deformations caused by the joints and by the segments are calculated using the method as described in chapter 5.1, while the total deformations are extracted from measurement equipment TU1-TU12 as described in figure 4.3. This explains why adding up the first two columns not results in the values given in the third column.

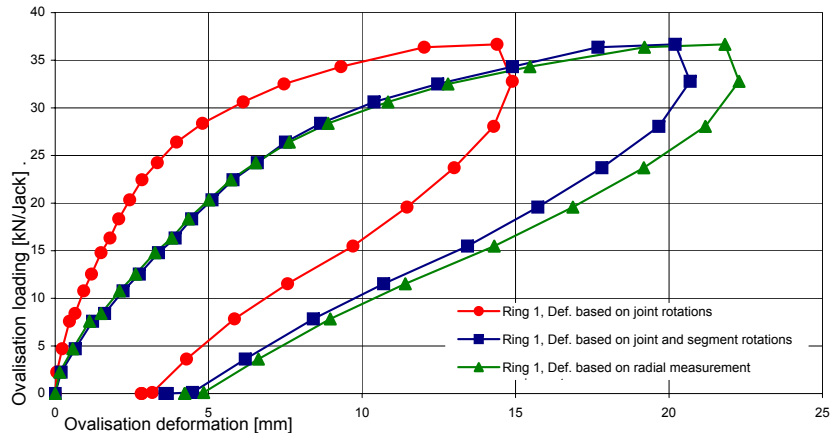


Figure E.1: Ovalisational deformation of lining, Ring 1, Experiment C01

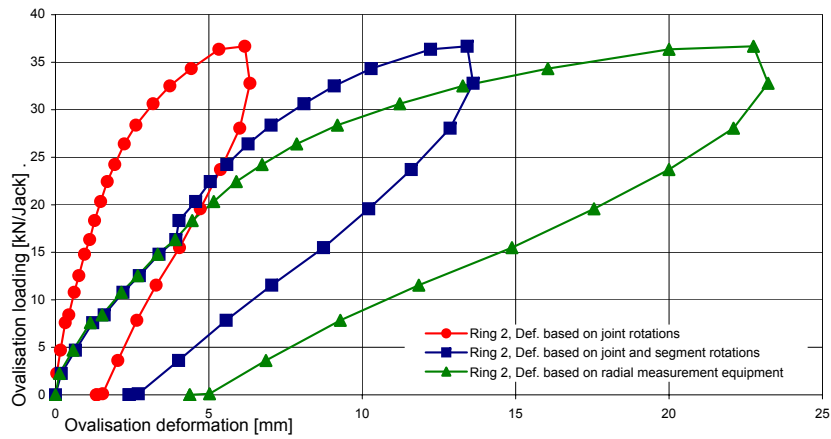


Figure E.2: Ovalisational deformation of lining, Ring 2, Experiment C01

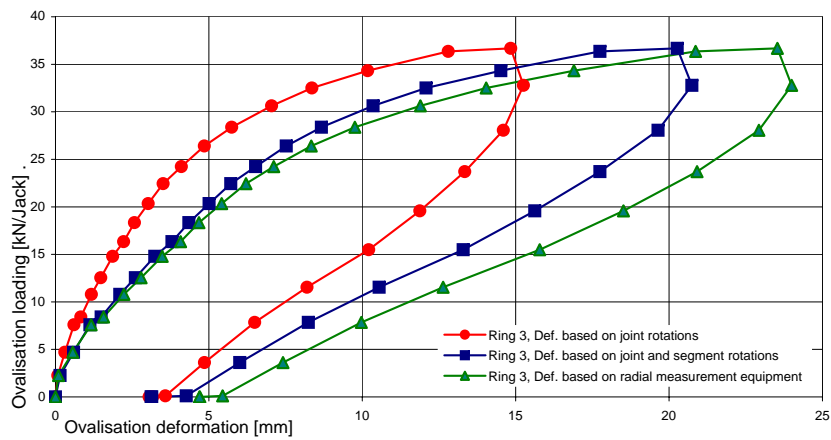


Figure E.3: Ovalisational deformation of lining, Ring 3, Experiment C01

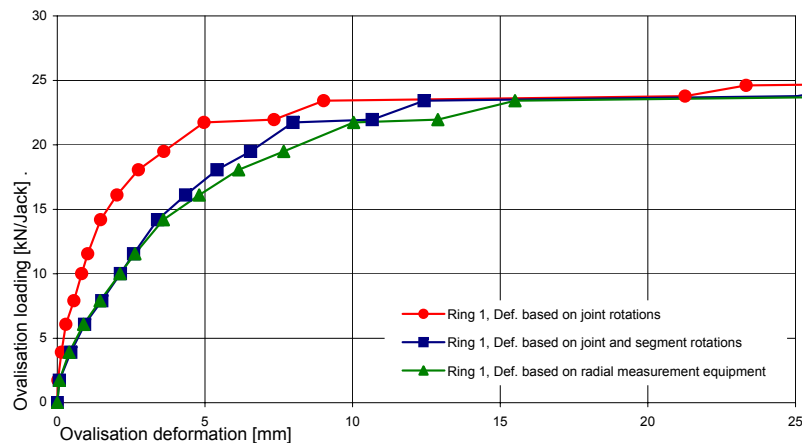


Figure E.4: Ovalisational deformation of lining, Ring 1, Experiment C02

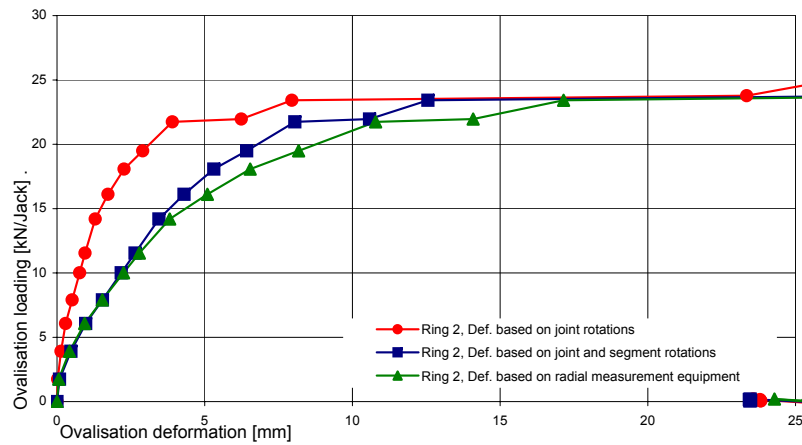


Figure E.5: Ovalisational deformation of lining, Ring 2, Experiment C02

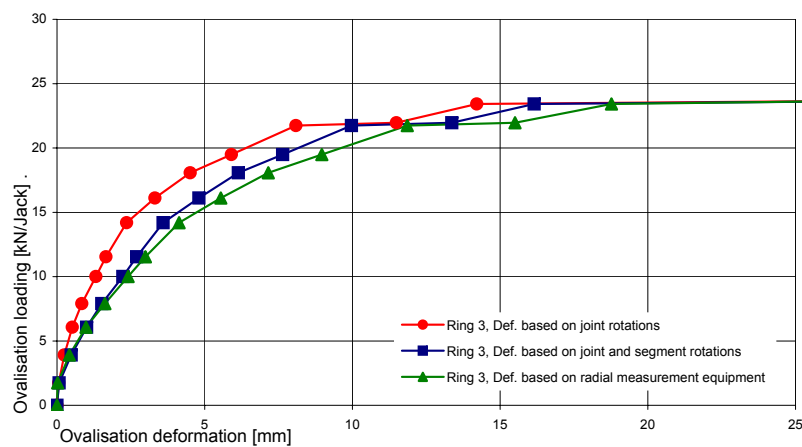


Figure E.6: Ovalisational deformation of lining, Ring 3, Experiment C02

Ultimate Limit State Analysis of a Segmented Tunnel Lining

C01	Ring 1			Ring 2			Ring 3		
	Joint def. [mm]	Segment def [mm]	Total def. [mm]	Joint def. [mm]	Segment def [mm]	Total def. [mm]	Joint def. [mm]	Segment def [mm]	Total def. [mm]
0,000	0,000	0,000	0,000	0,000	0,000	0,000	0,000	0,000	0,000
2,247	0,051	0,144	0,145	0,041	0,147	0,130	0,078	0,075	0,099
4,699	0,227	0,427	0,572	0,162	0,487	0,574	0,306	0,284	0,562
7,591	0,464	0,756	1,120	0,319	0,895	1,137	0,603	0,519	1,162
8,409	0,646	0,964	1,496	0,433	1,156	1,520	0,825	0,664	1,569
10,783	0,930	1,285	2,097	0,612	1,588	2,147	1,173	0,925	2,233
12,540	1,183	1,560	2,622	0,763	1,972	2,684	1,478	1,128	2,792
14,788	1,496	1,873	3,250	0,948	2,427	3,333	1,864	1,375	3,481
16,333	1,786	2,124	3,797	1,114	2,810	3,901	2,223	1,576	4,080
18,343	2,070	2,378	4,339	1,275	2,752	4,459	2,577	1,774	4,676
20,342	2,428	2,682	5,012	1,474	3,094	5,159	3,023	1,985	5,417
22,443	2,829	2,966	5,727	1,687	3,359	5,894	3,508	2,206	6,209
24,237	3,326	3,260	6,535	1,934	3,653	6,734	4,104	2,419	7,113
26,408	3,958	3,547	7,627	2,242	4,038	7,862	4,855	2,668	8,338
28,376	4,800	3,848	8,893	2,622	4,408	9,189	5,746	2,925	9,759
30,626	6,124	4,264	10,844	3,183	4,919	11,225	7,045	3,306	11,897
32,512	7,456	5,005	12,799	3,729	5,357	13,275	8,361	3,720	14,041
34,332	9,313	5,587	15,468	4,425	5,862	16,052	10,176	4,340	16,900
36,359	12,026	5,661	19,203	5,329	6,897	19,999	12,805	4,944	20,866
36,671	14,398	5,802	21,823	6,172	7,249	22,754	14,839	5,427	23,533
32,790	14,895	5,795	22,285	6,341	7,271	23,229	15,256	5,487	23,998
28,050	14,289	5,380	21,185	6,008	6,856	22,103	14,598	5,043	22,930
23,711	13,000	4,817	19,180	5,378	6,218	19,995	13,343	4,406	20,912
19,574	11,464	4,264	16,867	4,721	5,492	17,552	11,878	3,746	18,514
15,488	9,702	3,734	14,308	4,045	4,693	14,881	10,209	3,081	15,785
11,535	7,571	3,133	11,409	3,283	3,766	11,842	8,199	2,351	12,635
7,839	5,844	2,570	8,963	2,653	2,911	9,283	6,496	1,747	9,970
3,620	4,281	1,914	6,621	2,033	1,979	6,860	4,859	1,149	7,414
0,107	3,165	1,308	4,840	1,537	1,162	5,021	3,584	0,677	5,446
0,000	2,826	0,750	4,216	1,356	1,046	4,374	3,169	-0,031	4,708
0,000	2,804	0,853	4,227	1,333	1,070	4,382	3,055	0,063	4,695

Figure E.7: Numerical values belonging to figures E.1-E.3

C02	Ring 1			Ring 2			Ring 3		
	Joint def. [mm]	Segment def [mm]	Total def. [mm]	Joint def. [mm]	Segment def [mm]	Total def. [mm]	Joint def. [mm]	Segment def [mm]	Total def. [mm]
0,000	0,000	0,000	0,000	0,000	0,000	0,000	0,000	0,000	0,000
1,736	0,024	0,048	0,071	0,021	0,064	0,060	0,057	0,014	0,023
3,911	0,140	0,319	0,405	0,138	0,335	0,422	0,247	0,232	0,418
6,074	0,291	0,638	0,891	0,291	0,680	0,936	0,518	0,485	0,980
7,906	0,562	0,947	1,451	0,512	1,029	1,533	0,839	0,678	1,622
10,014	0,826	1,316	2,126	0,766	1,411	2,254	1,316	0,913	2,408
11,548	1,032	1,555	2,631	0,949	1,694	2,787	1,658	1,038	2,994
14,194	1,468	1,928	3,595	1,293	2,157	3,816	2,355	1,235	4,132
16,112	2,021	2,327	4,808	1,728	2,574	5,093	3,316	1,487	5,546
18,069	2,748	2,664	6,141	2,269	3,038	6,538	4,510	1,629	7,153
19,485	3,608	2,940	7,667	2,903	3,519	8,178	5,902	1,736	8,963
21,743	4,968	3,012	10,033	3,906	4,144	10,784	8,090	1,879	11,856
21,957	7,342	3,325	12,890	6,239	4,341	14,085	11,490	1,873	15,502
23,423	9,022	3,404	15,501	7,951	4,605	17,148	14,212	1,940	18,768
23,776	21,262	3,788	28,946	23,346	5,279	31,516	33,006	2,063	31,208
24,614	23,330	3,955	29,838	25,357	5,611	31,713	35,811	2,145	31,012
24,782	29,945	4,341	30,551	32,132	6,130	31,728	44,055	2,268	30,662
24,099	30,819	4,367	30,566	32,980	6,148	31,734	45,012	2,284	30,558
20,930	30,917	4,364	30,550	33,119	6,132	31,741	45,116	2,265	30,546
17,262	30,514	4,094	30,550	32,894	5,801	31,745	44,514	2,121	30,376
11,819	28,742	3,305	30,307	31,913	4,649	31,746	41,870	1,794	30,591
8,832	26,660	2,579	29,975	30,658	3,347	31,355	38,609	1,557	30,990
3,315	22,919	1,527	28,431	28,006	1,851	29,673	33,111	1,237	29,993
-0,176	20,606	0,815	26,030	25,906	0,754	27,084	29,387	0,967	28,156
0,194	18,266	-0,023	24,014	23,571	-0,107	24,286	26,486	0,385	26,327
0,054	18,988	-0,659	24,218	23,824	-0,370	25,128	27,604	-0,043	27,147
0,064	19,017	-0,581	24,429	23,817	-0,335	25,226	27,738	-0,074	27,267
0,156	19,027	-0,575	24,422	23,800	-0,363	25,237	27,740	-0,079	27,281

Figure E.8: Numerical values belonging to figures E.4-E.6



## Appendix F

# FE results compared to experimentally obtained data

In this appendix the results from FE analysis are compared to experimentally obtained data. The material properties of the concrete used in the simulation of experiment C01 correspond to Curve IV of figure 7.13, whereas the properties of the concrete in simulating experiment C02 are in accordance with paragraph 10.2. In table F.1 the performed comparisons are summarised.

Description	Experiment	Figure
Average joint + average total deformation per ring	C01	F.1-F.3
Joint rotations	C01	F.4-F.6
Compression strains per ring in circumferential direction	C01	F.7-F.12
Average joint + average total deformation per ring	C02	F.13-F.15
Joint rotations	C02	F.16-F.18
Compression strains per ring in circumferential direction	C02	F.19-F.24

**Table F.1:** Summary of figures showing comparison between FEA and experimentally obtained results

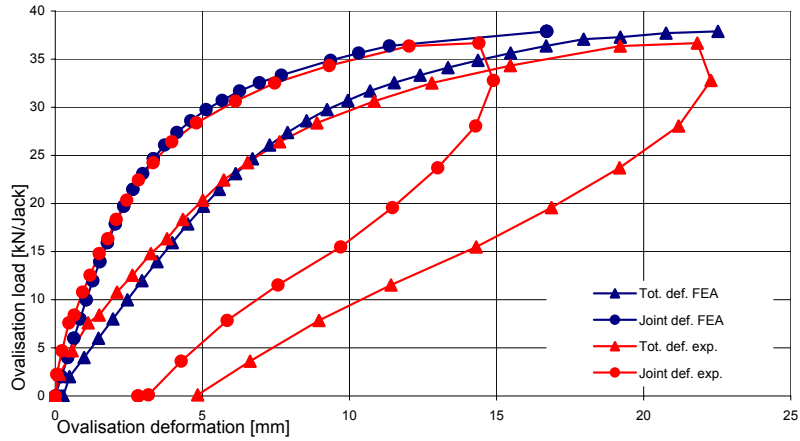


Figure F.1: Total and joint deformation of FE model compared to experimental data, ring 1 C01

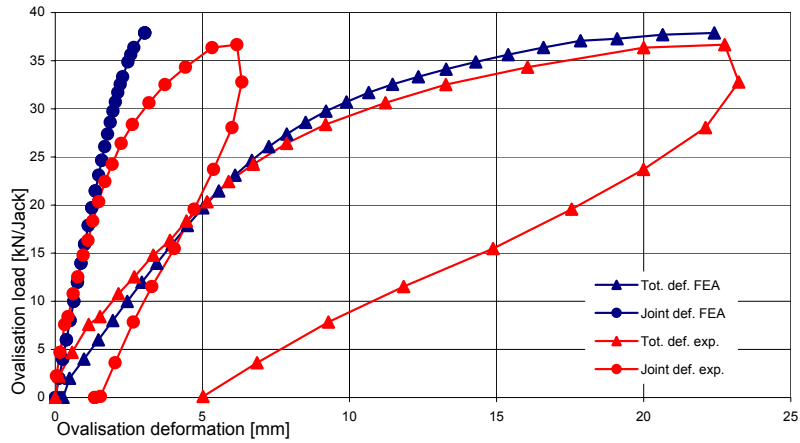


Figure F.2: Total and joint deformation of FE model compared to experimental data, ring 2 C01

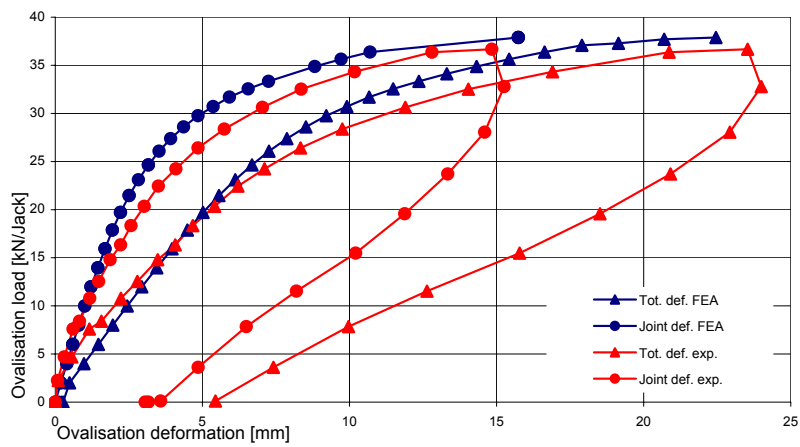


Figure F.3: Total and joint deformation of FE model compared to experimental data, ring 3 C01

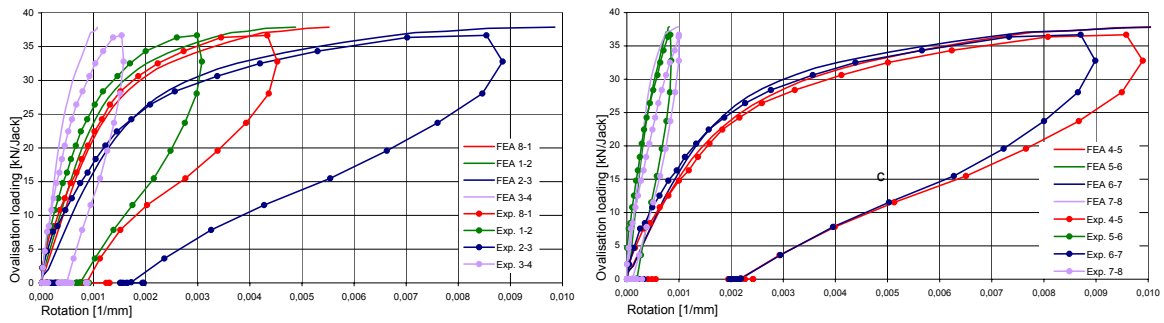


Figure F.4: Rotations in joints in ring 1, FE results compared to experimental data C01

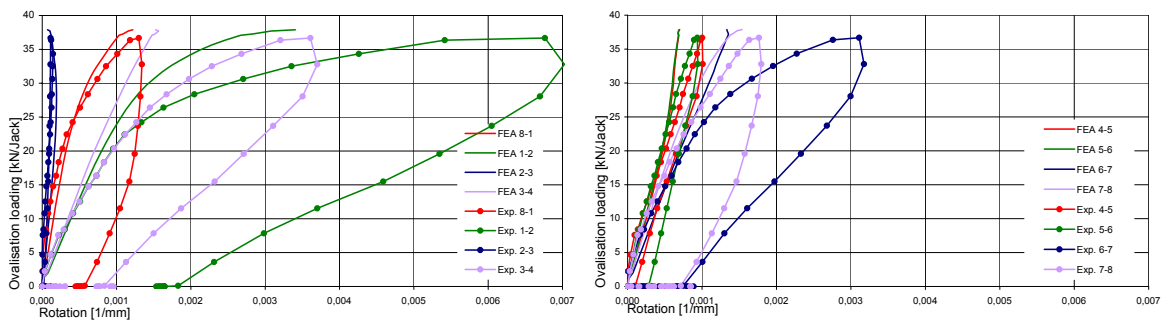


Figure F.5: Rotations in joints in ring 2, FE results compared to experimental data C01

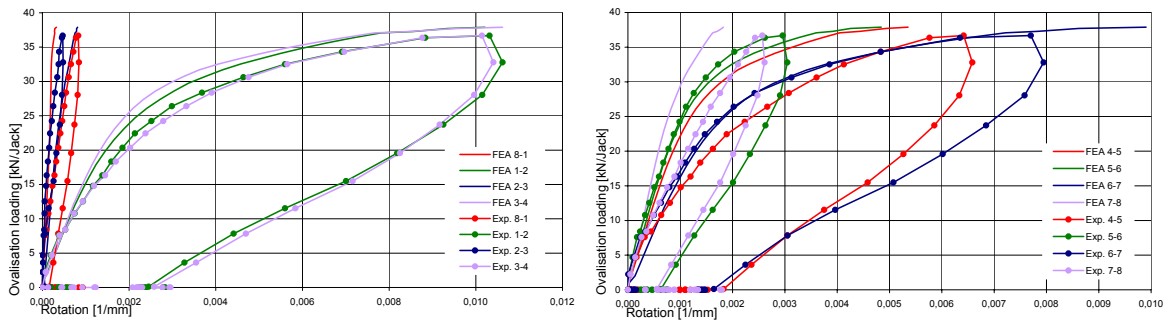
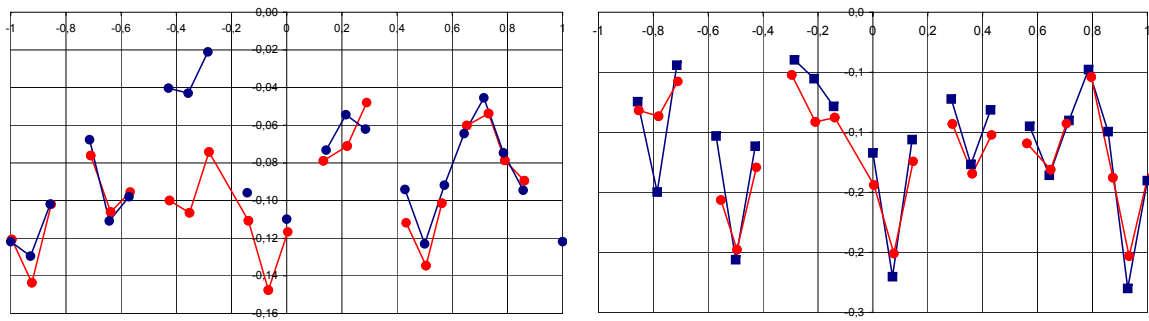
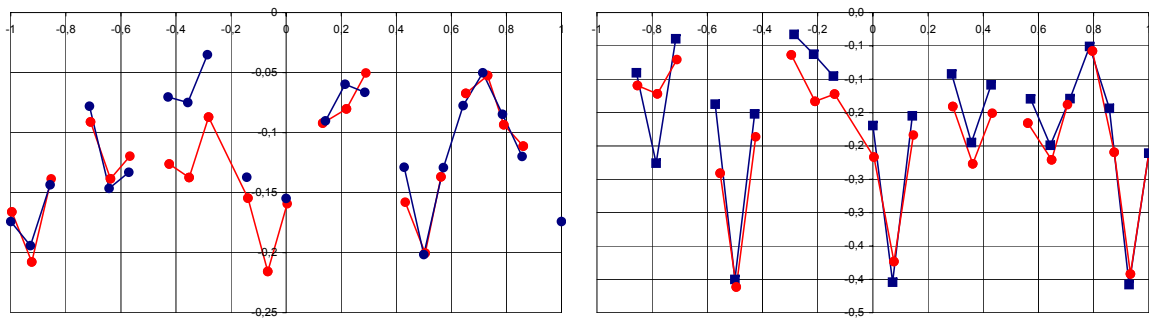


Figure F.6: Rotations in joints in ring 3, FE results compared to experimental data C01



**Figure F.7:** Comparison of compression strain from experiment and FEA in circumferential direction, ovalisation load  $16 \text{ kN/Jack}$ , ring 1(left) and ring 2 (right), C01, blue=exp. red=FEA



**Figure F.8:** Comparison of compression strain from experiment and FEA in circumferential direction, ovalisation load  $26 \text{ kN/Jack}$ , ring 1(left) and ring 2 (right), C01, blue=exp. red=FEA

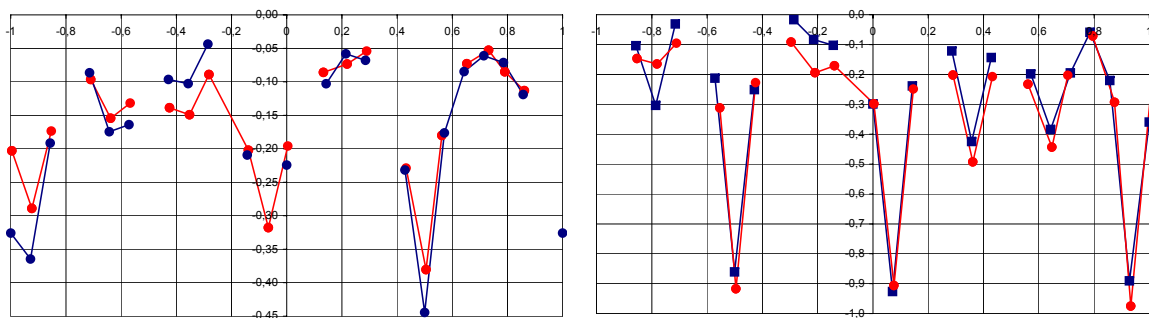


**Figure F.9:** Comparison of compression strain from experiment and FEA in circumferential direction, ovalisation load  $36 \text{ kN/Jack}$ , ring 1(left) and ring 2 (right), C01, blue=exp. red=FEA

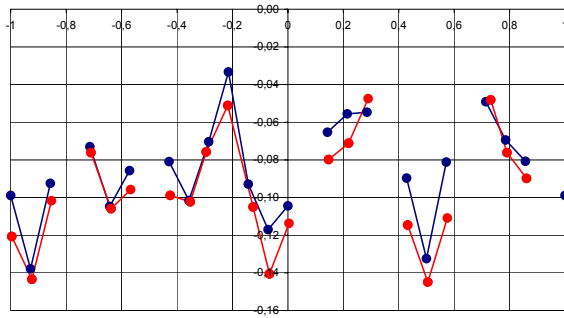


**Figure F.10:** Comparison of compression strain from experiment and FEA in circumferential direction, ovalisation load  $16 \text{ kN/Jack}$ , ring 3, C01, blue=exp. red=FEA

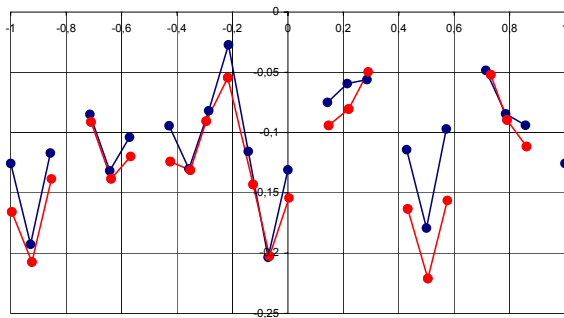


**Figure F.11:** Comparison of compression strain from experiment and FEA in circumferential direction, ovalisation load  $26 \text{ kN/Jack}$ , ring 3, C01, blue=exp. red=FEA

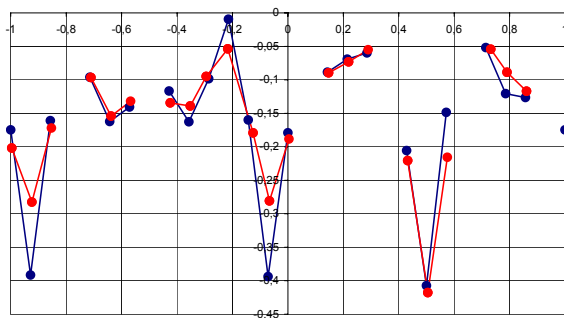


**Figure F.12:** Comparison of compression strain from experiment and FEA in circumferential direction, ovalisation load  $36 \text{ kN/Jack}$ , ring 3, C01, blue=exp. red=FEA

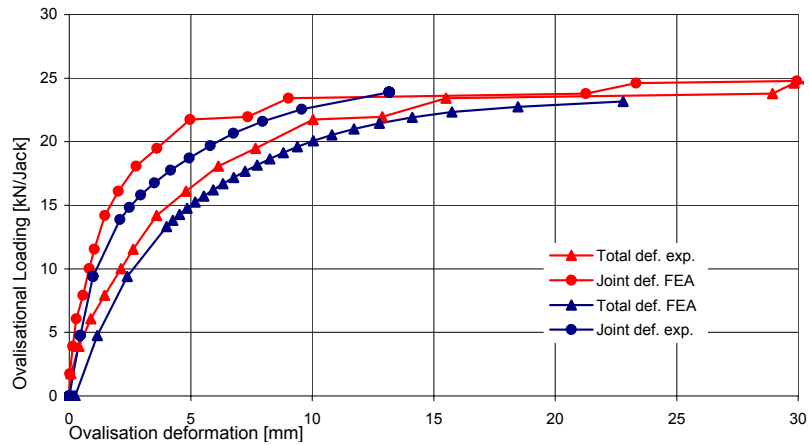


Figure F.13: Total and joint deformation of FE model compared to experimental data, ring 1 C02

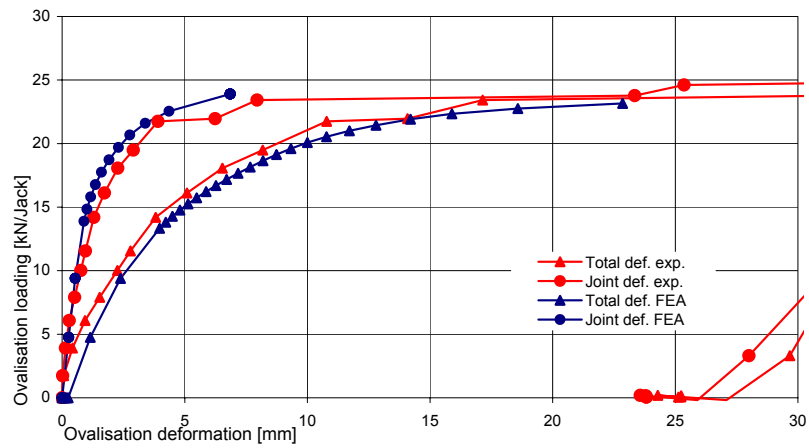


Figure F.14: Total and joint deformation of FE model compared to experimental data, ring 2 C02

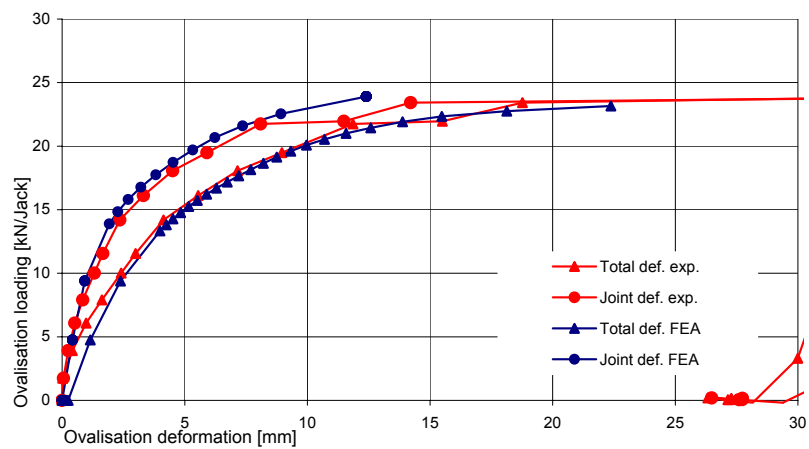


Figure F.15: Total and joint deformation of FE model compared to experimental data, ring 3 C02

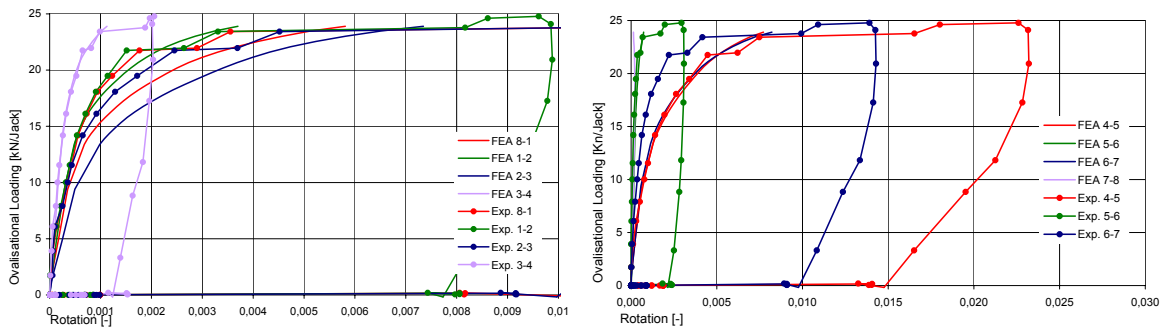


Figure F.16: Rotations in joints in ring 1, FE results compared to experimental data C02

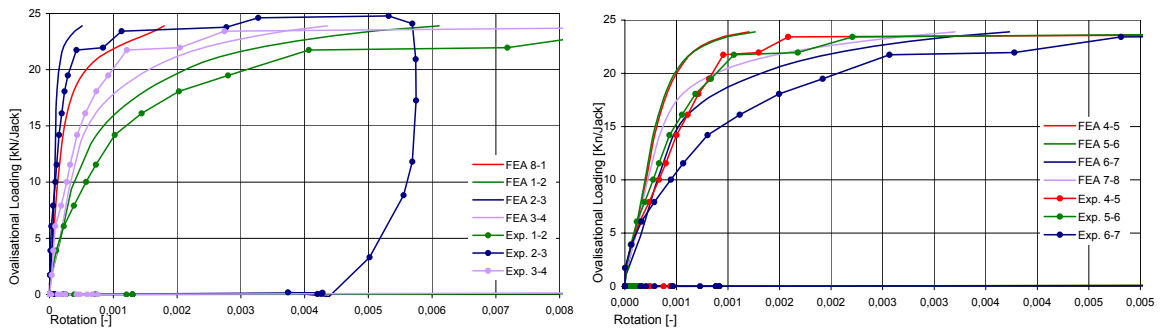


Figure F.17: Rotations in joints in ring 2, FE results compared to experimental data C02

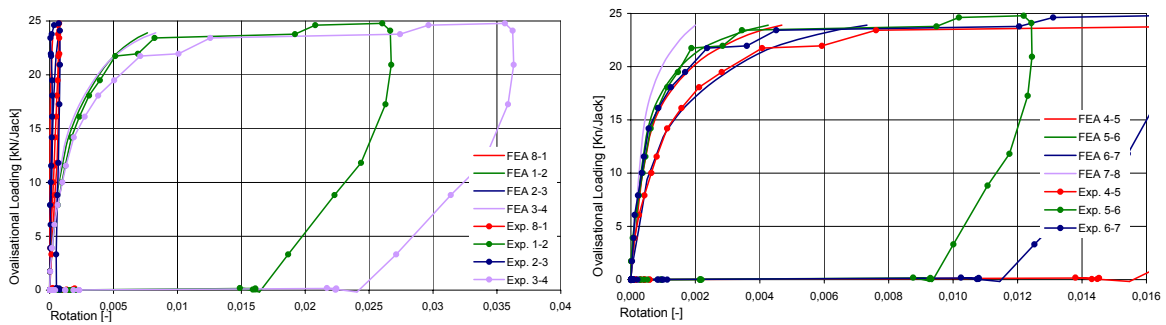
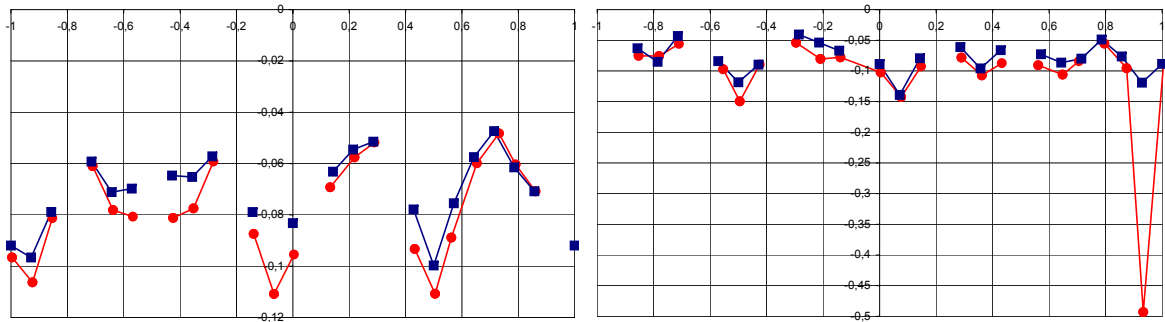
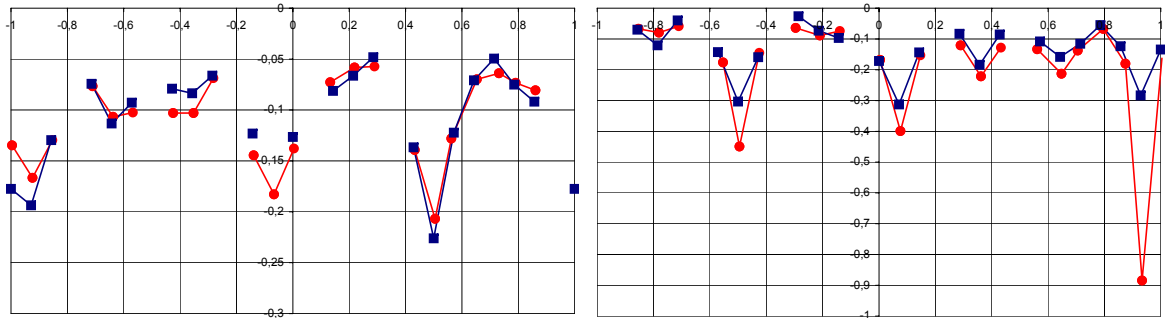


Figure F.18: Rotations in joints in ring 3, FE results compared to experimental data C02



**Figure F.19:** Comparison of compression strain from experiment and FEA in circumferential direction, ovalisation load  $10 \text{ kN/Jack}$ , ring 1(left) and ring 2 (right), C02, blue=exp. red=FEA



**Figure F.20:** Comparison of compression strain from experiment and FEA in circumferential direction, ovalisation load  $20 \text{ kN/Jack}$ , ring 1(left) and ring 2 (right), C02, blue=exp. red=FEA

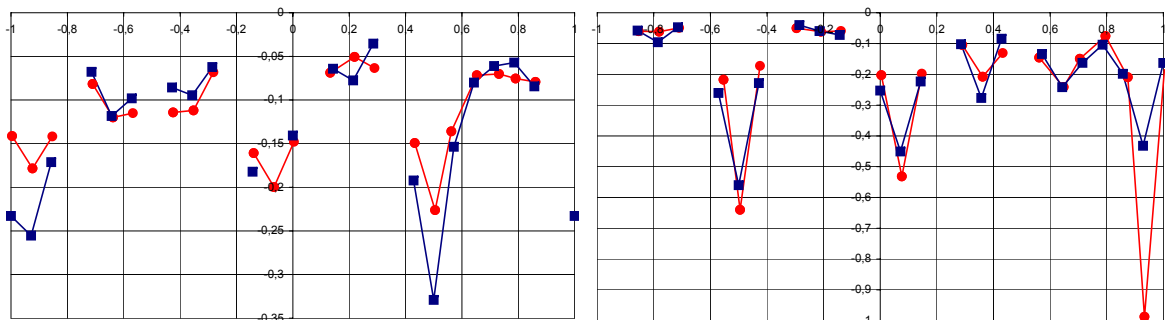


**Figure F.21:** Comparison of compression strain from experiment and FEA in circumferential direction, ovalisation load  $23 \text{ kN/Jack}$ , ring 1(left) and ring 2 (right), C02, blue=exp. red=FEA

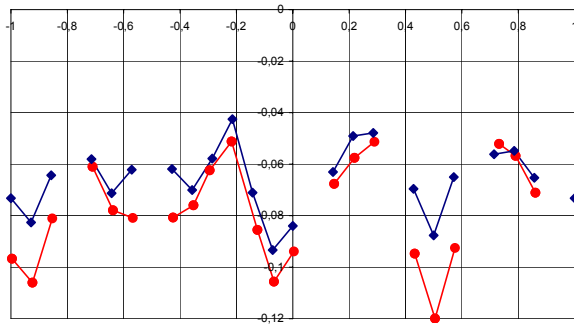


**Figure F.22:** Comparison of compression strain from experiment and FEA in circumferential direction, ovalisation load 10  $kN/Jack$ , ring 3, C02, blue=exp. red=FEA

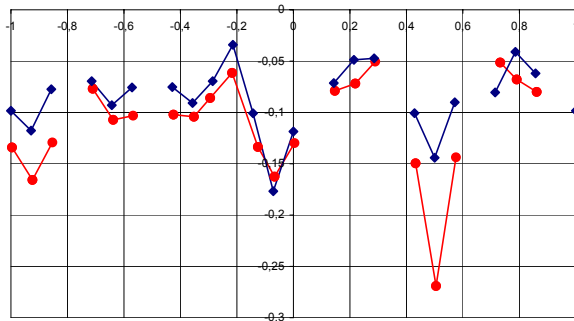


**Figure F.23:** Comparison of compression strain from experiment and FEA in circumferential direction, ovalisation load 20  $kN/Jack$ , ring 3, C02, blue=exp. red=FEA

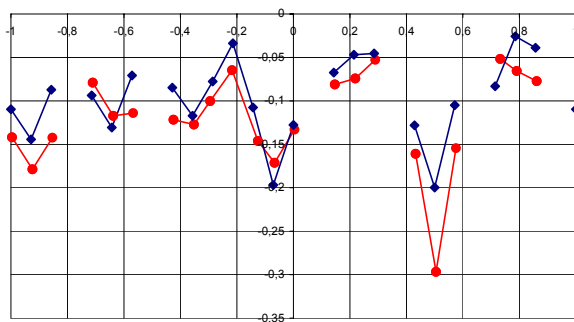


**Figure F.24:** Comparison of compression strain from experiment and FEA in circumferential direction, ovalisation load 23  $kN/Jack$ , ring 3, C02, blue=exp. red=FEA



## Appendix G

# Validating numerical analysis of a single tunnel segment

The moment-curvature relation of a single tunnel segment is thoroughly elucidated in chapter 7.2 and is based on 1D FE calculations using DIANA. These results are validated in this appendix.

The bending moment curvature relations are obtained by modelling a single tunnel segment, clamped at one end and loaded with a bending moment at the other end. This way a constant moment is present in the beam resulting in a constant curvature. The 4.000 *mm* in length beam is subdivided in 20 beam elements which are numerically integrated over their cross-sections, using 11 integration points. The FE calculations are performed using DIANA.

To validate the obtained bending moment-curvature relations the same calculations are performed with DIANA only now using 41 instead of 11 integration points along the height of an element. This should result in more accurate results but it does not validate the DIANA calculations. Therefore another program (DRNS) is used, developed by Vervuurt and Van Gogh (2000). The stress-strain relations of the concrete and the steel are given to the program which subsequently performs a cross-section calculation. The results of 'DRNS' and of the beam model using 11 and 41 integrations points are given in figures G.1 and G.2. Four comparisons are shown representing the bending moment-curvature relations belonging to the earlier mentioned four different concrete properties. From the graphs it is concluded that a very good agreement is found between the different calculations. From that it is concluded that correct calculation results are obtained by using beam elements in DIANA.

The clamped beam, subject to a constant normal force and an increasing bending moment, may also be simulated in DIANA by using 2D plane stress elements. In the figures G.3 and G.4 a comparison is shown between bending moment-curvature relations obtained with a 1D and a 2D FE model. Discrepancies between the curves are found for curves II, III and IV. At the start of cracking the curvatures in the 2D model start to increase more rapidly but eventually the same bending capacity is reached. In the last curve shown there is also a discrepancy between the 1D and the 2D model. Not only is the non-linear stiffness different, also the bending capacity of the 2D model is smaller.

## Ultimate Limit State Analysis of a Segmented Tunnel Lining

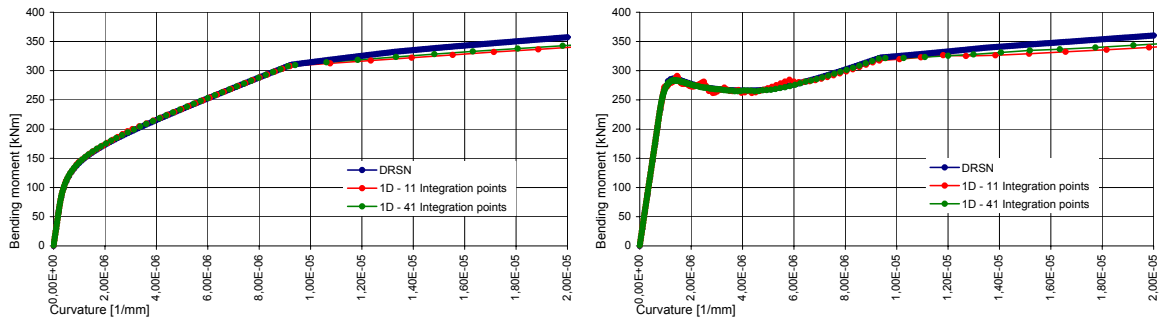


**Figure G.1:** Bending moment-curvature relations from DIANA compared to ‘DRNS’ for concrete properties belonging to Curve I (left) and Curve II (right)

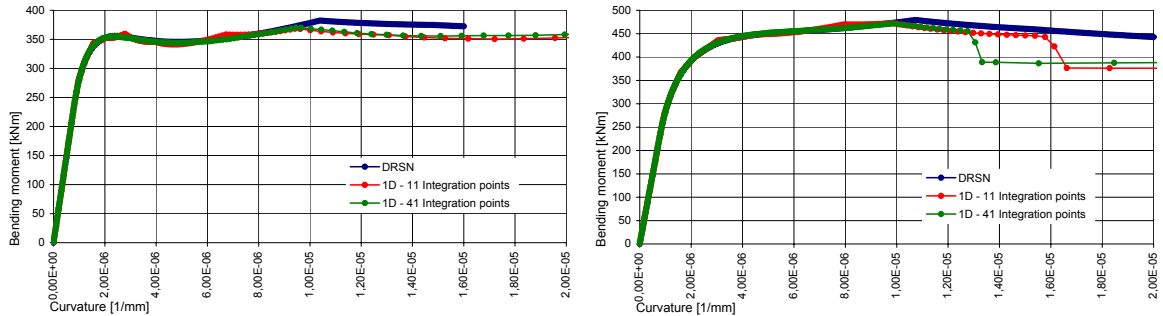


**Figure G.2:** Bending moment-curvature relations from DIANA compared to ‘DRNS’ for concrete properties belonging to Curve III (left) and Curve IV (right)

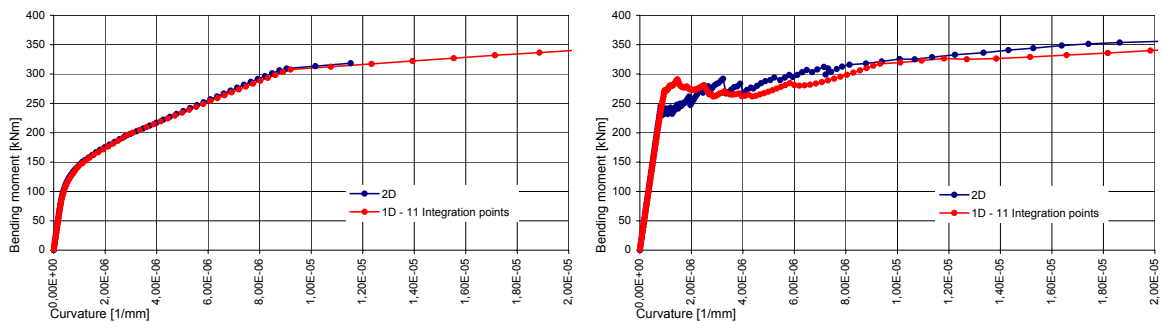


**Figure G.3:** Bending moment-curvature relations from 1D beam model compared to 2D plane stress model for Curve I (left) and Curve II (right)

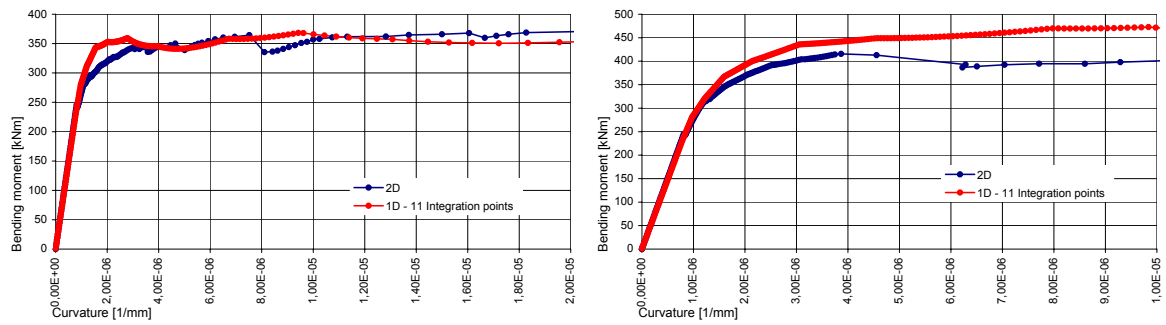


Figure G.4: Bending moment-curvature relations from 1D beam model compared to 2D plane stress model for Curve III (left) and Curve IV (right)



## Appendix H

# Comparison of bending moments between experiment C01 and C02

In this appendix the bending moments in the three separate rings are shown at an ovalisation load of  $10\text{ kN/Jack}$ ,  $15\text{ kN/Jack}$  and  $23\text{ kN/Jack}$  for both experiments.

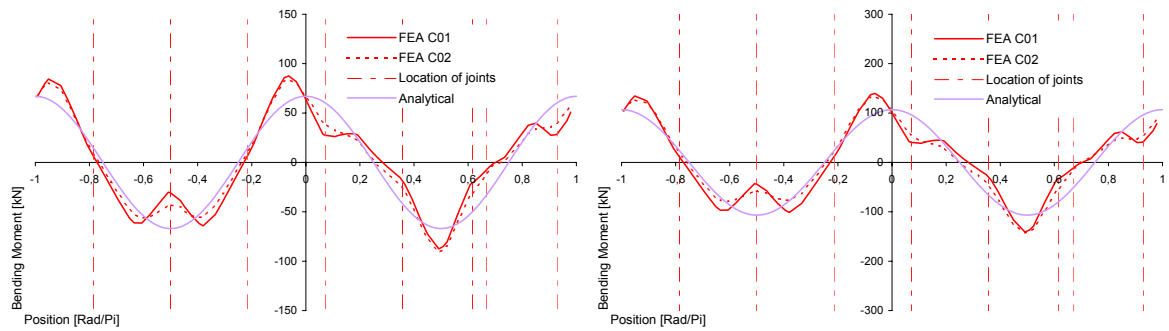


**Figure H.1:** Bending moments in ring 1 at an ovalisation load of 10 *kN/Jack* (left) and 15 *kN/Jack* (right)

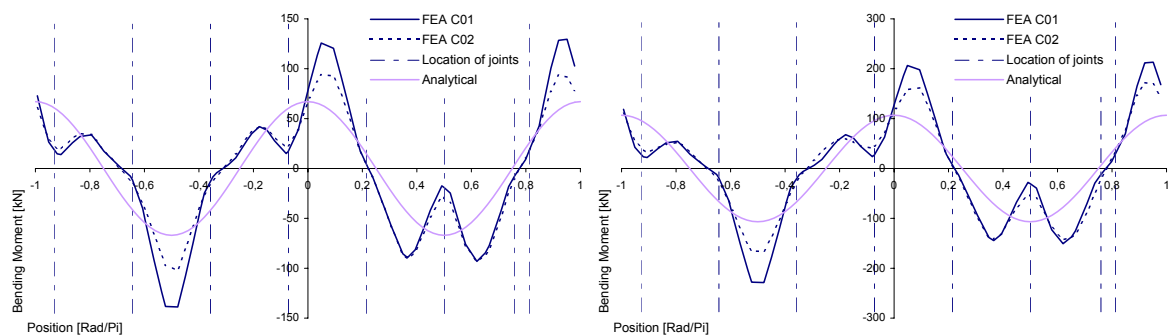


**Figure H.2:** Bending moments in ring 2 at an ovalisation load of 10 *kN/Jack* (left) and 15 *kN/Jack* (right)

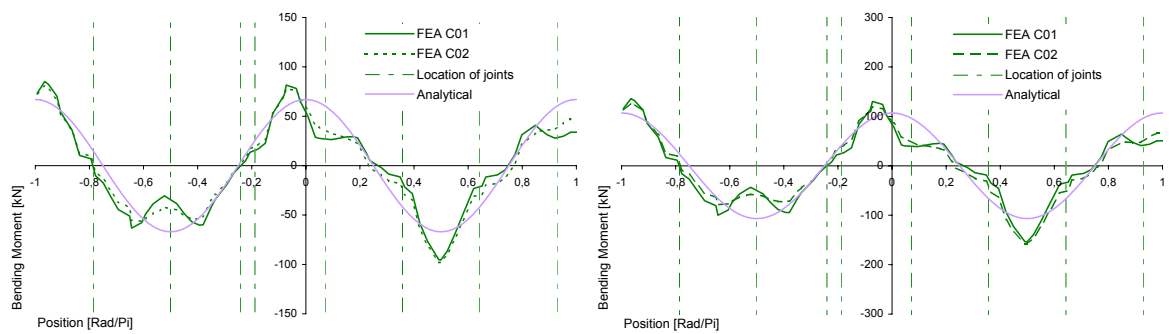


**Figure H.3:** Bending moments in ring 3 at an ovalisation load of 10 *kN/Jack* (left) and 15 *kN/Jack* (right)

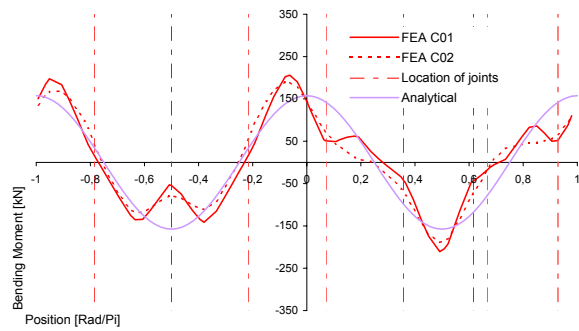


**Figure H.4:** Bending moments in ring 1 at an ovalisation load of  $23 \text{ kN/Jack}$

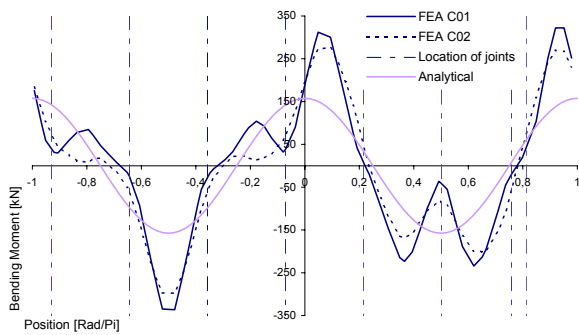


**Figure H.5:** Bending moments in ring 1 at an ovalisation load of  $23 \text{ kN/Jack}$

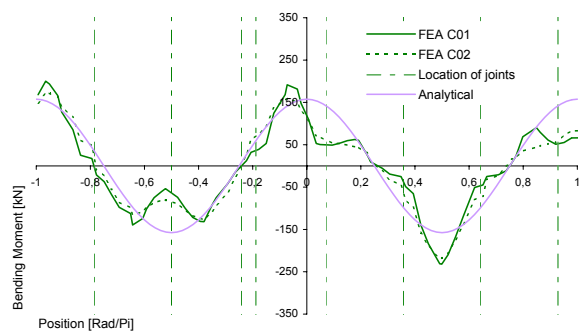


**Figure H.6:** Bending moments in ring 1 at an ovalisation load of  $23 \text{ kN/Jack}$



# Appendix I

## Data on CD

All data obtained during the experiment is found on the enclosed CD. Discontinuous measured data, like from strain gauges placed on segments and LVDT measurements placed on joints, but also continuous measured joints rotations are included. These files are used as input for two other excel files which calculated the deformed shape of the lining. The deformed shape of the lining is calculated based on joint rotations and/or based on segment curvatures as extensively described in chapter 5.1. By also selecting an enlargement factor and the reference and loading step the deformations of the lining can be analysed in great detail. The 1D beam model as well as the 2D plane stress model which are used for describing structural behaviour are also included. In the table I.1 the content of the CD is given.

Contents	File name	Kind of file
Data obtained during experiment C01	C01_str-eng.xls	Excel file
	C01_SegmentJoints.xls	Excel file
Data obtained during experiment C01	C02_str-eng(1).xls	Excel file
	C02_SegmentJoints.xls	Excel file
Deformation of lining experiment C01	Deformation_Lining_C01.xls	Excel file
Deformation of lining experiment C02	Deformation_Lining_C02.xls	Excel file
1D FE model simulating C01	Tunnel_1D_C01.dat	DIANA data file
	Nonlin_1D_C01.com	DIANA command file
	Tunnel_1D_C01.fdb	FX+ model file
2D FE model simulating C01	Tunnel_2D_C01.dat	DIANA data file
	Nonlin_2D_C01.com	DIANA command file
	Tunnel_2D_C01.fdb	FX+ model file
1D FE model simulating C01 and C02	Tunnel_1D_C0121.dat	DIANA data file
	Tunnel_1D_C0122.dat	DIANA data file
	Nonlin_1D_C012.com	DIANA command file
	Tunnel_1D_C012.fdb	FX+ model file

**Table I.1:** Content of enclosed CD





